EVALUATION OF $k-\omega$ TURBULENCE MODEL AND EULER FLUX SCHEMES FOR SHOCK WAVE TURBULENT BOUNDARY LAYER INTERACTION

By

SAUMIL B. PATEL

A thesis submitted to the

School of Graduate Studies

Rutgers, The State University of New Jersey

in partial fulfillment of the requirements

for the degree of

Master of Science

Graduate Program in Mechanical and Aerospace Engineering

written under the direction of

Dr. Doyle D. Knight

and approved by

_____

_____

_____

New Brunswick, New Jersey

May, 2018

ABSTRACT OF THE THESIS

EVALUATION OF $k-\omega$ TURBULENCE MODEL AND EULER FLUX SCHEMES FOR SHOCK WAVE TURBULENT BOUNDARY LAYER INTERACTION

By SAUMIL B. PATEL

Thesis Director:

Dr. Doyle D. Knight

Shock-wave boundary-layer interaction (SBLI) has long been an important phenomenon in aerodynamics, from transonic through to hypersonic speeds. High-speed flow has been at the center of research for many applications such as the hypersonic flight engine (i.e., scramjet), aircraft (i.e., SR-72), re-entry vehicle (i.e., Space Shuttle), missile (i.e., BrahMos-II) and high-speed transportation (i.e., Hyperloop, Uber Elevate). As hypersonics is still an area of research, we need more reliable CFD models to predict the flow structures of the flows over complex geometries. For that purpose, available models should be validated in order to develop an understanding of a reliable computational model development approach for hypersonic flow. In the current research work, the assessment of the $k-\omega$ Wilcox (2006) turbulence model to predict surface aerothermodynamic loading on a large hollow cylinder flare configuration for turbulent flows ranging from Mach 5 to 8 has been performed. Additionally, three Euler flux schemes, i.e., Roe, AUSM+ and HLLE+, have been evaluated along with a grid independence study. The experimental data from CUBRC has been used for validation of the numerical results. The surface pressure is consistently underpredicted

and surface heat transfer is consistently overpredicted by the $k-\omega$ Wilcox (2006) turbulence model. Also, an unphysical spike in turbulent kinetic energy is observed upstream of the reattachment location. The $k-\omega$ turbulence model overpredicts the size of the separation region for all cases which is an important factor to be taken into consideration while designing control surfaces for hypersonic vehicles.

Keywords: CFD, RANS, SBLI, Hypersonics, Turbulence

Acknowledgments

I would like to take this opportunity to express my gratitude to my family and friends who were there for me as a source of strength and encouragement. I would like to especially thank my parents, Bharat and Meena, and lovely sister, Gargi, for their unconditional support to this endeavor of mine. I do not have enough words to express my appreciation for their dedication, love, and continued confidence in me. I am very grateful to my advisor Dr. Doyle D. Knight for his support, guidance, and patience throughout my thesis project. I am still impressed by his comprehensive knowledge in numerical computation and his analytical approach to problems. This inspired me, enriched my growth as a student and nourished my intellectual maturity, which I will benefit from throughout my engineering career. Also, Mahsa Mortazavi and Nadia Kianvashrad, two Ph.D. candidates from my research group, have been my go-to persons for any doubts and they have been kind enough to answer my silliest questions with patience and smile. Dr. Reece Neel from Aerosoft Inc. has always been there for technical guidance. Dr. Alexei Kotelnikov, associate director of information technology at RUSOE, has always been very supportive in troubleshooting any problems I had with SOE cluster. Lastly, my friends, Shashank Thakker, Gaurav Mishra, Jay Patel, Dhruv Bhatt, Kalyan Inamdar and many others have been so supportive during my thesis work that I never felt alone during this journey.

Dedication

This thesis is dedicated to my country, India, and my parents, Bharat, and Meena.

Table of Contents

List of Tables

List of Figures

List of Abbreviations

A	Jacobian matrix; Roe matrix
a	Speed of sound
C_{ijk}	Turbulent transport tensor
c	Fastest characteristic speed
E	Total energy
e	Specific internal energy
e_n	Non-equilibrium vibrational energy
F	Flux vector
f	Entropy flux vector
H	Total enthalpy; Height
h	Specific enthalpy
$i,\ j,\ k$	Unit vectors in $x,\ y,\ z$ directions
$Kr+$	Surface roughness coefficient representing average surface element height
k	Kinetic energy of turbulent fluctuations per unit mass; thermal conductivity coefficient
L	Length
Δ_L	Characteristic length of the cell
M	Mach number
$\hat{n}$	Unit normal vector
Pr	Prandtl number
p	Static pressure
P	Mean static pressure
Q	Conserved quantities vector
q_j	Heat-flux vector
$q_{L_j},\ q_{T_j}$	Laminar, turbulent mean heat-flux vector
R	Perfect-gas constant
S	Source term vector
Sc	Schmidt number
s''_{ij}	Fluctuating strain-rate tensor
T	Temperature
t	Time
t_{ij}	Viscous Stress Tensor
u_i	Instantaneous velocity in tensor notation
u	Instantaneous velocity in vector notation
u'_i	Fluctuating velocity in tensor notation
u'	Fluctuating velocity in vector notation
$\tilde{u}_i$	Favre-averaged velocity in tensor notation
$\tilde{u}$	Favre-averaged velocity in vector notation; Roe-averaged velocity
u''_i	Favre fluctuating velocity in tensor notation
u''	Favre fluctuating velocity in vector notation
x_i	Position vector in tensor notation

x	Position vector in vector notation
y^+	Dimensionless, sublayer-scaled, distance, $u_\tau y/\nu$
γ	Specific heat ratio, c_p/c_v
δ	Boundary-layer or shear-layer thickness
δ_{ij}	Kronecker delta
ϵ	Dissipation per unit mass
ε	Internal energy per unit mass
ζ	Second viscosity coefficient; entropy
τ	Specific volume, $1/\rho$
τ_{ij}	Specific Reynolds stress tensor, $-\overline{u_i' u_j'}$
ω	Specific dissipation rate; vorticityvector magnitude
Ω_{ij}	Mean-rotation tensor; Vorticity
Π	Coles' wake-strength parameter
ρ	Mass density
λ	Courant (CFL) number
κ	Coefficient for spatial accuracy of MUSCL formulation
μ	Molecular viscosity; Mach angle
μ_T	Eddy viscosity
ν	Kinematic molecular viscosity, μ/ρ

Chapter 1

Introduction

For flight at hypersonic speeds, shock wave turbulent boundary layer interaction is an important phenomenon for determination of aerothermodynamic loads in many applications such as transonic compressors, supersonic inlet diffuser, ramjet etc. Also, we are entering an era of high speed transportation be it Hyperloop [1], Uber Elevate [2], Boom Technology [3] or intercontinental flights as proposed by Elon Musk at International Astronautical Congress in Adelaide, Australia in September 2017. All these technological breakthroughs will require accurate prediction of aerothermodynamic loading for the successful design of vehicles. The aerothermodynamic loading on hypersonic vehicles represents a significant engineering design challenge. Shock wave boundary layer interaction can result in an order of magnitude or more peak heat loads above stagnation point heating values.

Since inception of computational fluid dynamics, turbulent flow modeling has been a major breakthrough which opened many applications for CFD (Computational FLuid Dynamics). One of the next research breakthroughs needed is an accurate numerical prediction of important properties, specifically heat transfer rate, for turbulent hypersonic flow. Although we need to solve 3D CFD computational problems, the basic understanding of the 3D flow structures with minimum amount of computational resources can be achieved with 2D axisymmetric models. For 2D-axisymmetric cases, still there is a need for more validation studies of current numerical models and development of new models [4]. In the process of development of the new turbulence models, we need to understand existing turbulence models which will enable us to identify correct modeling approach.

American, European, Australian and Japanese programs have focused on varied aspects of SBLI (Shock Wave Boundary Layer Interaction) and have greatly contributed to fundamental and applied advances over the last decade [5]. A classic example of consequences of

shock interaction is flight number 2-53-97 of the X-15 in which a test model pylon mounted beneath the fuselage disintegrated due to the impingement of a supersonic jet generated by a shock-shock interaction [6]. The ability to accurately predict both the magnitude and location of peak aerothermodynamic loading is therefore essential to the development of effective hypersonic vehicles. Over the past five decades numerous studies have focused on assessment of the capability of Computational Fluid Dynamics (CFD) to accurately predict aerothermodynamic loads on simple geometries that generate shock wave boundary layer interactions similar to flight conditions [7]. The Hypersonic International Flight Research Experimentation Program (HIFiRE) vehicle research program has been one of the key establishments for SBLI research with extensive ground test results. Several Advisory Group for Aerospace Research and Development (AGARD), USA and NATO Research and Technology Office, USA task groups have been formed for investigation of 2D/3D shock wave laminar/turbulent boundary layer interactions. These AGARD and RTO groups concluded that CFD did not consistently achieve an accurate prediction of peak heat transfer in shock wave boundary layer interactions [7]. This observation suggests that there is an urgent need for an accurate prediction of aerothermodynamic loads at hypersonic speeds.

In 1970, after more than twenty years since the first systematic investigation of the interaction between a shock wave and boundary layer, J. E. Green [8] noted that there was not a single coherent theoretical framework which would embrace all facets of the problem, and the available experimental results, though numerous, were spread thinly over a wide field. The number of situations in which confident predictions could be made, either theoretically or by interpolating or extrapolating experimental results, was therefore comparatively small. In 2001, David S. Dolling [9] observed that even after more than fifty years of SBLI research, important quantities such as peak heat transfer cannot be accurately predicted and unsteady pressure loads cannot be predicted at all. This indicates the amount of research required and the need to model new or modify existing flux and turbulence models in order to accurately simulate hypersonic flows with SBLI. Dolling also suggested a future outlook on development and application of simulation tools and measurements.

Delery (1985) [10] examined various features of SBLIs such as upstream interaction

length, incipient shock induced separation and evolution of the boundary layer properties during the interaction process. Also, the means envisaged to control shock-wave boundary-layer interactions were presented, with emphasis on the physics of phenomena involved in this process, i.e., those acting on the boundary layer properties before it enters the shock region (e.g., wall cooling, wall mass transfer, upstream blowing) and those having a local action in the shock foot region itself (e.g., suction or injection, boundary layer removal, passive control).

The SBLI occurs in those regions of a high speed vehicle in which two surfaces intersect. Simple configurations have been studied which resemble these regions. Panaras [11] reviewed gradual progress in the understanding of the nature of such flow fields. Numerical simulations of experimentally-studied swept-shock/boundary layer interactions have appeared in the literature since the early seventies. Algebraic turbulence models of Escudier [12] and Baldwin and Lomax [13] were considered by Hung and MacCormack [14] for fin/plate (M = 5.9, fin angle, $\alpha = 6^\circ$ and 12°). Though the grid was rather coarse for the calculation of turbulent interactions (21 x 36 x 32 points), good agreement was found between the computed results and the experimental data, for both the surface pressures and the heat transfer in the case of the weak interaction ($\alpha = 6^\circ$). For the case of $\alpha = 12^\circ$, the computed results do not demonstrate the experimentally observed existence of peak pressure near the corner; however, the range of interaction and the value and location of peak heat transfer were well predicted.

Gaitonde [5] reviewed SBLI research in unsteadiness, heat transfer prediction capability, complex interaction, and flow control techniques. It was noted that SBLI can result in loss of control authority, peaks in thermo-mechanical loading, and adverse effects on structures due to unsteadiness on the exterior of the aircraft. The fundamental physics of SBLI are best examined in canonical situations. In the mid-1990s, more experimental efforts actively considered data generation and processing for numerical validation. An extensive compilation of data and analysis for transitional and turbulent flows at different interaction strengths is presented in a series of publications by Holden et al. [15]-[16]. These data have been extensively used by computationalists to predict surface quantities by examining turbulence

modeling aspects. Knight and Degrez [17] compiled RANS results from simulations for several 2-D and 3-D interactions. The turbulence models range from algebraic to full Reynolds stress equation formulations for the single fin, double fin and the hollow cylinder flare. The basic conclusions were that heat transfer and skin friction predictions were generally poor, with up to 100% discrepancy for the stronger interactions displaying significant separated regions. Heat transfer rates for laminar conditions have been predicted accurately with adequate meshing support while accurate prediction of turbulent heat transfer rates still remain an area of research. It has been observed by Knight et al. [17] that heat transfer rates and unsteadiness for SBLIs are not captured by RANS methods.

1.1 Outline

In the chapter 2, the experimental and computational studies are summarized which defines scope of this thesis. Equations solved in the numerical simulations, i.e., Navier-Stokes equation, equation of state, energy equation, and turbulence equations are described in the chapter 3. Three Euler flux algorithms, grid generation techniques, and solver parameters are presented in chapter 4. Finally, results and conclusion are discussed in the following chapters. Many of the figures in this thesis are taken from the work of the respective authors and their collaborators mainly because of their ready availability - their selection is not meant to construe that they are necessarily first or most illustrative in their class.

Chapter 2

Problem Statement

2.1 Experimental Study

Experimental studies have been conducted at CUBRC [18], a research, development, testing and systems integration organization. Detailed heat transfer and pressure measurements were obtained in regions of shock-wave turbulent-boundary layer interaction over a hollow cylinder/flare configuration in high Reynolds number hypervelocity flows for comparison with computations with CFD codes employing a range of turbulence models. These studies were conducted at a series of Mach numbers between 5 and 8, in cold flows and in flows with duplicated flight velocities in fully turbulent flows.

Data sets were obtained with high-frequency PCB piezoelectric surface pressure and platinum thin film heat transfer instrumentation installed in the large hollow cylinder/flare model shown installed in the LENS II tunnel [19] in Figure 2.1. The accuracy of the pressure measurements are estimated to be +/- 5% and the heat transfer measurements +/-3%.

Figure 2.1: LENS II Wind Tunnel [18]

The large scale of the models used in these experiments enabled to obtain measurements in fully turbulent flows with the length of turbulent flow up to 1,000 boundary layer thicknesses

downstream of the beginning of untripped transition. The surface measurements obtained in these studies together with Schlieren and interferometry measurements of the regions of shock-wave boundary-layer interaction were originally assembled to provide data sets for blind code validation studies. To predict these flows with RANS techniques, the non-equilibrium nature of the turbulent processes in the separation and reattachment regions requires models that are significantly more sophisticated than those required to describe attached flows in mild pressure gradients.

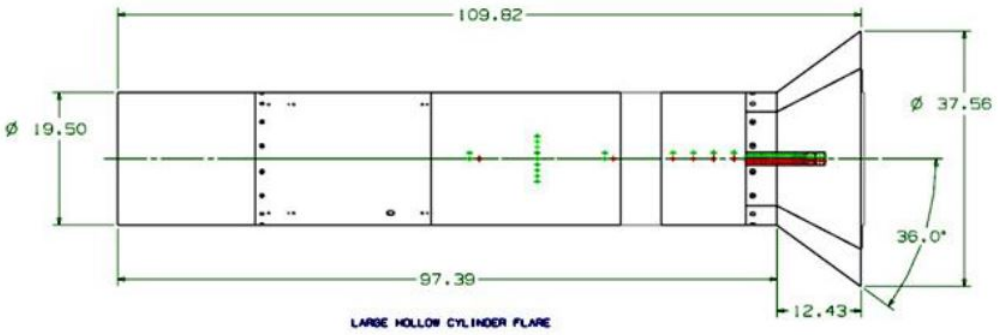

Figure 2.2: Dimensions of the Model [18]

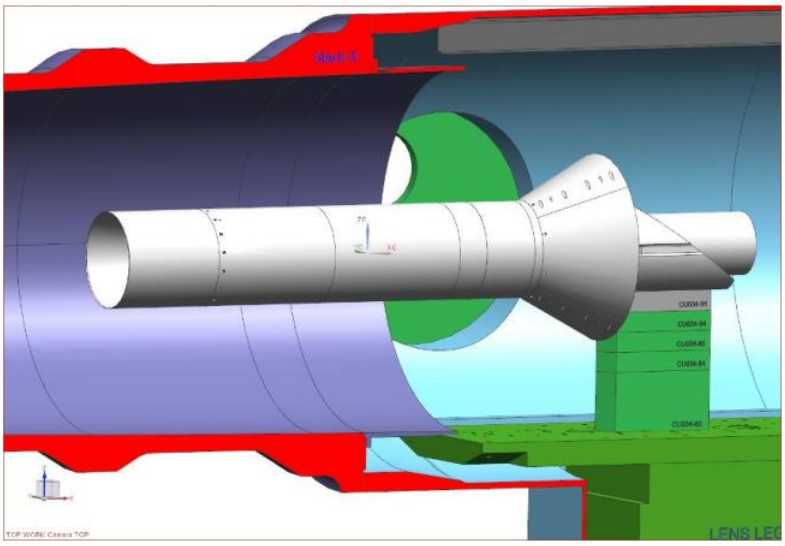

Figure 2.3: Schematic Figure of the Model [18]

The facility test conditions is established and validated by a combination of measurements in the reservoir region and test section of the tunnel. The stagnation pressure and enthalpy are obtained directly from pressure measurements behind the reflected shock and measurements of the incident shock Mach number. Figure 2.2 shows dimensions of the hollow cylinder/flare configuration and Figure 2.3 shows 3D modeling sketch of the hollow cylinder/flare.

Conditions in the freestream are obtained from survey rakes containing pitot pressure probes, stagnation heat transfer gauges on hemispherical cylinders, total temperature measurements with vented thermocouple probes (where applicable). A series of six experiments were conducted (Table 2.1). The physical test model is shown in the Figure 2.4.

Figure 2.4: Physical Model of LHCF [18]

Case	Mach Number	Velocity (ft/s)	Temperature (R)	Density $(slug/ft^3)$	Reynolds Number Based on Hollow Cylinder	T_w/T_0
1	4.95	4774	385	0.000212	32.3 $\times 10^6$	0.25
2	4.97	4766	381	0.000414	63.3 $\times 10^6$	0.25
3	5.95	5578	364	0.000102	17.3 $\times 10^6$	0.20
4	6.01	5496	347	0.000306	53.3 $\times 10^6$	0.20
5	6.96	6869	404	0.000089	17 $\times 10^6$	0.14
6	7.96	7115	332	0.0000449	10.5 $\times 10^6$	0.14

Table 2.1: Test Conditions [18]

2.2 Computational Study

A systematic detailed computational study has been conducted to recreate the physics of the experimental test conditions. A very intensive grid independence study has been conducted where grids of up to 8 million cells have been created in Plot3D format using the C++ programming language. Numerical results presented here are obtained by solving the RANS equations using the GASPex commercial CFD software by Aerosoft Inc [20]. GASPex is a structured/unstructured, multi-block CFD flow solver which solves the Reynolds Averaged Navier-Stokes (RANS) equations as well as the heat conduction equation for solid bodies.

In this study, the experiments of CUBRC [18] were simulated using a perfect gas model. The flow is assumed to be uniform at the inflow with the given inlet Mach number. The fluid is assumed to be viscous, perfect gas with no chemical reactions. The governing equations are the compressible Reynolds Averaged Navier-Stokes equations with the turbulence incorporated using the $k-\omega$ Wilcox (2006) model [21] without compressibility correction and with surface roughness, Kr+ = 5 to solve for the computational domain. Kr+ represents the average height of sand-grain roughness elements. The computations were performed on 80 cores with 2000 MB of memory per core using Rutgers university's SOE (School of Engineering) cluster's Linux HPC platform. The Gauss-Seidel time integration scheme has been used to achieve a steady state solution. In this computation, three Euler flux algorithms, AUSM+ (Advection Upstream Splitting Method) [22], HLLE+(Harten-Lax-van Leer-Einfeldt Improved) [23] and Roe [24] have been evaluated. The reconstruction is performed by third order primitive MUSCL [25], [26] with the Courant-Friedrichs-Lewy (CFL) number ranging from 0.1 to 50.

Post processing has been carried out in Matlab and Tecplot. Matlab has been utilized for qualitative visualization which is for comparing surface pressure and heat transfer with experimental results. Also, Matlab has been helpful in investigating grid independence. Tecplot has been used for a more qualitative visualization like streamlines, and contours.

Chapter 3

Theory: Equations Solved

3.1 Navier-Stokes Equations

The Navier-Stokes equations, developed by Claude-Louis Navier and George Gabriel Stokes in 1822, are equations which can be used to determine the velocity vector field that applies to a fluid, given some initial conditions (obtained through zone initialization - pressure, temperature and boundary conditions). They arise from the application of Newton's second law in combination with a fluid stress (due to viscosity) and a pressure term. For almost all real situations, they result in a system of nonlinear partial differential equations. Usually, however, they remain nonlinear, which makes them difficult or impossible to solve analytically; this is what causes the turbulence and unpredictability in their results.

The Navier-Stokes equations can be derived from the basic conservation and continuity equations applied to properties of fluids. These equations can be derived either for a fluid particle that is moving with the flow (Lagrangian) or for a fluid element that passes through specific locations in the space as time passes (Eulerian). For CFD purposes we need them in Eulerian form. The relation between these both forms exists in the material derivative of a fluid property. In order to derive the equations of fluid motion, we must first derive the continuity equation (which dictates conditions under which things are conserved), apply the equation to conservation of mass, momentum and energy. The Navier-Stokes equations are a special case of the (general) continuity equation.

For motion in a compressible medium, we must solve the equations governing conservation of mass, momentum and energy. The unsteady compressible equations are as follows in Cartesian coordinates [21] using the Einstein summation notation:

$$\frac{\partial \rho}{\partial t} + \frac{\partial}{\partial x_i}(\rho u_i) = 0 \tag{3.1}$$

$$\frac{\partial}{\partial t}(\rho u_i) + \frac{\partial}{\partial x_j}(\rho u_j u_i) = -\frac{\partial p}{\partial x_i} + \frac{\partial t_{ji}}{\partial x_j}, \quad \text{for } i = 1, 2, 3 \tag{3.2}$$

$$\frac{\partial}{\partial t}\left[\rho\Big(e + \frac{1}{2}u_i u_j\Big)\right] + \frac{\partial}{\partial x_j}\left[\rho u_j\Big(h + \frac{1}{2}u_i u_j\Big)\right] = \frac{\partial}{\partial x_j}(u_i t_{ij}) - \frac{\partial q_j}{\partial x_j}, \quad \text{for } i = 1, 2, 3 \tag{3.3}$$

where e is the specific internal energy and $h = e + p/\rho$ is the specific enthalpy. For compressible flow, the viscous stress tensor, t_{ij}, involves the second viscosity, ζ, as well as the conventional molecular viscosity, μ. For gases, we use the perfect gas law so that pressure, density and temperature are related by

$$p = \rho R T \tag{3.4}$$

where R is the perfect-gas constant.

3.2 Reynolds-Averaged Navier-Stokes (RANS) Equations

As Reynolds averaging of incompressible fluid gives rise to the Reynolds-stress tensor, we expect that similar averaging of compressible fluid will lead to a turbulent heat-flux vector. We also expect that new compressibility-related correlations will appear throughout the equations of motion. In addition to velocity and pressure fluctuations, we must also account for density and temperature fluctuations when the medium is a compressible fluid. If we use the standard time-averaging procedure, the mean conservation equations contain additional terms that have no analogs in the laminar equations. [21] The problem of establishing the appropriate form of the time-averaged equations can be simplified dramatically by using the density-weighted averaging procedure suggested by Favre [27]. That is, we introduce the mass-averaged velocity, $\tilde{u}_i$, defined by

$$\bar{\rho}\tilde{u}_i(\vec{x}, t) = \lim_{n\to\infty} \frac{1}{n} \sum_{\nu=1}^{n} \rho^{(\nu)}(\vec{x}, t) u_i^{(\nu)}(\vec{x}, t) \tag{3.5}$$

where $u_i^{(\nu)}(\vec{x},t)$ is a realization of the flow velocity u_i at $(\vec{x},t)$ and similarly for $\rho^{(\nu)}$ and $\bar{\rho}$ is the conventional ensemble averaged density.

$$\bar{\rho} = \lim_{n\to 0} \sum_{\nu=1}^{n} \rho^{(\nu)} \tag{3.6}$$

where an overbar denotes conventional Reynolds average. Note that $\overline{\rho u_i''} = 0$ from the definition of the Favre average.

In order to mass average the conservation equations, we now decompose the various flow properties as follows:

$$\begin{aligned} u_i &= \tilde{u}_i + u_i'', \quad \rho = \bar{\rho} + \rho', \quad p = P + p' \\ h &= \tilde{h} + h'', \quad e = \tilde{e} + e'', \quad T = \tilde{T} + T'' \\ q_j &= q_{L_j} + q_j' \end{aligned} \tag{3.7}$$

Note that we decompose p, ρ and q_j in terms of conventional mean and fluctuating parts. Substituting equations (3.7) into equations (3.1) - (3.4) and performing the mass-averaging operations, we arrive at what are generally referred to as the *Favre (mass) averaged mean conservation equations* [21].

$$\frac{\partial \bar{\rho}}{\partial t} + \frac{\partial}{\partial x_i}(\bar{\rho}\tilde{u}_i) = 0 \tag{3.8}$$

$$\frac{\partial}{\partial t}(\bar{\rho}\tilde{u}_i) + \frac{\partial}{\partial x_j}(\bar{\rho}\tilde{u}_j\tilde{u}_i) = -\frac{\partial P}{\partial x_i} + \frac{\partial}{\partial x_j}\big[\bar{t}_{ji} - \overline{\rho u_j'' u_i''}\big], \quad \text{for } i = 1,2,3 \tag{3.9}$$

$$\begin{aligned} \frac{\partial}{\partial t}\Big[\bar{\rho}\Big(\tilde{e} + \frac{\tilde{u}_i\tilde{u}_j}{2}\Big) + \frac{\overline{\rho u_i'' u_j''}}{2}\Big] + \frac{\partial}{\partial x_j}\Big[\bar{\rho}\tilde{u}_j\Big(\tilde{h} + \frac{\tilde{u}_i\tilde{u}_j}{2}\Big) + \tilde{u}_j\frac{\overline{\rho u_i'' u_j''}}{2}\Big] \\ = \frac{\partial}{\partial x_j}\big[-q_{L_j} - \overline{\rho u_j'' h''} + \overline{t_{ji}u_i''} - \overline{\rho u_j''\frac{1}{2}u_i'' u_i''}\big] \\ + \frac{\partial}{\partial x_j}\big[\tilde{u}_i\big(\bar{t}_{ij} - \overline{\rho u_i'' u_j''}\big)\big] \end{aligned} \tag{3.10}$$

$$P = \bar{\rho}R\tilde{T} \tag{3.11}$$

3.3 Turbulence Modeling

The Favre-averaged Reynolds-stress tensor is

$$\bar{\rho}\tau_{ij} = -\overline{\rho u_i'' u_j''} \tag{3.12}$$

As in the incompressible case, the Favre-averaged τ_{ij} is a symmetric tensor.

Equation (3.10), the Favre-averaged mean-energy equation for total energy (i.e., the sum of internal energy, mean flow kinetic energy and turbulence kinetic energy) has numerous additional terms, each of which represents an identifiable physical process or property. Consider first the double correlation between u_i'' and itself that appears in each of the two terms on the left hand side. This is the kinetic energy per unit volume of the turbulent fluctuations, so that it makes sense to define

$$\bar{\rho}k = \frac{1}{2}\overline{\rho u_i'' u_i''} \tag{3.13}$$

Next, the correlation between u_j'' and h'' is the turbulent transport of heat. In analogy to the notation selected for the molecular transport of heat, we define

$$q_{T_j} = \overline{\rho u_j'' h''} \tag{3.14}$$

The two terms $\overline{t_{ji} u_i''}$ and $\overline{\rho u_j'' \frac{1}{2} u_i'' u_i''}$ on the right-hand side of the equation (3.10) correspond to molecular diffusion and turbulent transport of turbulence kinetic energy (k), respectively. These terms arise because the mass-averaged total enthalpy appearing in the convective term of Equation (3.10) is the sum of mass averaged enthalpy, mean kinetic energy and turbulence kinetic energy. They represent transfers between mean energy and turbulence kinetic energy that naturally arise when we derive the Favre-averaged turbulence kinetic energy equation. The simplest way to derive the equation for k is to multiply the primitive variable form of the instantaneous momentum equation by u_i'' and time average

$$\overline{\rho u_i'' \frac{\partial u_i}{\partial t}} + \overline{\rho u_i'' u_j \frac{\partial u_i}{\partial x_j}} = -\overline{u_i'' \frac{\partial P}{\partial x_i}} + \overline{u_i'' \frac{\partial t_{ji}}{\partial x_j}} \tag{3.15}$$

The most illuminating way to carry out the indicated time averaging operations is to proceed term by term, and to use tensor notation for all derivatives. Proceeding from left to right, we first consider the unsteady term.

$$\begin{aligned}\overline{\rho u_i'' u_{i,t}} &= \overline{\rho u_i''(\tilde{u}_i + u_i'')_{,t}} \\ &= \overline{\rho u_i''}\tilde{u}_{i,t} + \overline{\rho u_i'' u_{i,t}''} \\ &= \overline{\rho(\frac{1}{2}u_i'' u_i'')_{,t}} \\ &= \frac{\partial}{\partial t}(\bar{\rho}k) - \overline{\frac{1}{2}u_i'' u_i''\frac{\partial \rho}{\partial t}}\end{aligned} \tag{3.16}$$

where $u_{i,t} = \dfrac{\partial u_i}{\partial t}$

Turning now to the convective term, we have the following.

$$\begin{aligned}\overline{\rho u_i'' u_j u_{i,j}} &= \overline{\rho u_i''[(\tilde{u}_j + u_j'')\tilde{u}_{i,j} + u_j u_{i,j}'']} \\ &= \overline{\rho u_i''}\tilde{u}_j\tilde{u}_{i,j} + \overline{\rho u_i'' u_j''}\tilde{u}_{i,j} + \overline{\rho u_j u_i'' u_{i,j}''} \\ &= -\bar{\rho}\tau_{ij}\tilde{u}_{i,j} + \overline{\rho u_j(\tfrac{1}{2}u_i'' u_i'')_{,j}} \\ &= -\bar{\rho}\tau_{ij}\tilde{u}_{i,j} + \overline{(\rho u_j \tfrac{1}{2}u_i'' u_i'')_{,j}} - \overline{\tfrac{1}{2}u_i'' u_i''(\rho u_j)_{,j}} \\ &= -\bar{\rho}\tau_{ij}\tilde{u}_{i,j} + \big(\overline{\rho\tilde{u}_j\tfrac{1}{2}u_i'' u_i''} + \overline{\rho u_j''\tfrac{1}{2}u_i'' u_i''}\big)_{,j} - \overline{\tfrac{1}{2}u_i'' u_i''(\rho u_j)_{,j}} \\ &= -\bar{\rho}\tau_{ij}\frac{\partial \tilde{u}_i}{\partial x_j} + \frac{\partial}{\partial x_j}\big(\tilde{\rho}\tilde{u}_j k + \overline{\rho u_j''\tfrac{1}{2}u_i'' u_i''}\big) - \overline{\tfrac{1}{2}u_i'' u_i''\frac{\partial}{\partial x_j}(\rho u_j)}\end{aligned} \tag{3.17}$$

where $u_{i,j} = \dfrac{\partial u_i}{\partial x_j}$. The pressure-gradient term simplifies immediately as follows.

$$\overline{u_i'' p_{,i}} = \overline{u_i''}P_{,i} + \overline{u_i'' p'_{,i}} = \overline{u_i''}\frac{\partial P}{\partial x_i} + \frac{\partial}{\partial x_i}\big(\overline{p' u_i''}\big) - \overline{p'\frac{\partial u_i''}{\partial x_i}} \tag{3.18}$$

Finally, the viscous term is simply rewritten as

$$\overline{u_i'' t_{ji,j}} = \frac{\partial}{\partial x_j}\big(\overline{t_{ji}u_i''}\big) - \overline{t_{ji}\frac{\partial u_i''}{\partial x_j}} \tag{3.19}$$

Thus, substituting equations (3.16) to (3.19) into equation (3.15), we arrive at the Favre-averaged turbulence kinetic energy equation. In arriving at the final result, we make use of the fact that the sum of the last terms on the right-hand sides of equations (3.16) and (3.17) vanish since their sum is proportional to the two terms appearing in the instantaneous

continuity equation. Inspection of the turbulence kinetic energy equation also indicates that the Favre-averaged dissipation rate is given by

$$\bar{\rho}\epsilon = \overline{t_{ji}\frac{\partial u_i''}{\partial x_j}} = \frac{1}{2}\overline{t_{ji}\left(\frac{\partial u_i''}{\partial x_j} + \frac{\partial u_j''}{\partial x_i}\right)} = \overline{t_{ji}s_{ij}''} \tag{3.20}$$

where s_{ij}'' is the fluctuating strain-rate tensor. This is entirely consistent with the definition of dissipation for incompressible flows [21]. Using the similar derivation, the *Favre-averaged Reynolds-stress equation* assumes the following term:

$$\begin{aligned}\frac{\partial}{\partial t}(\bar{\rho}\tau_{ij}) + \frac{\partial}{\partial x_k}(\bar{\rho}\tilde{u}_k\tau_{ij}) = &-\bar{\rho}\tau_{ik}\frac{\partial \tilde{u}_j}{\partial x_k} - \bar{\rho}\tau_{ik}\frac{\partial \tilde{u}_i}{\partial x_k} + \bar{\rho}\epsilon_{ij} - \bar{\rho}\Pi_{ij} \\ &+ \frac{\partial}{\partial x_k}\Big[-\overline{(t_{kj}u_i'' + t_{ki}u_j'') + \bar{\rho}C_{ijk}}\Big] \\ &+ \overline{u_i''}\frac{\partial P}{\partial x_j} + \overline{u_j''}\frac{\partial P}{\partial x_i}\end{aligned} \tag{3.21}$$

where

$$\bar{\rho}\Pi_{ij} = \overline{p'\left(\frac{\partial u_i''}{\partial x_j} + \frac{\partial u_j''}{\partial x_i}\right)} \tag{3.22}$$

$$\bar{\rho}\epsilon_{ij} = \overline{t_{kj}\frac{\partial u_i''}{\partial x_k} + t_{ki}\frac{\partial u_j''}{\partial x_k}} \tag{3.23}$$

$$\bar{\rho}C_{ijk} = \overline{\rho u_i'' u_j'' u_k''} + \overline{p'u_i''}\delta_{jk} + \overline{p'u_j''}\delta_{ik} \tag{3.24}$$

Taking advantage of the definitions given in Equations (3.12), (3.13), (3.14) and (3.20), we can summarize the Favre-averaged mean equations and turbulence kinetic energy equation in conservation form.

$$\frac{\partial \bar{\rho}}{\partial t} + \frac{\partial}{\partial x_i}(\bar{\rho}\tilde{u}_i) = 0 \tag{3.25}$$

$$\frac{\partial}{\partial t}(\bar{\rho}\tilde{u}_i) + \frac{\partial}{\partial x_j}(\bar{\rho}\tilde{u}_j\tilde{u}_i) = -\frac{\partial P}{\partial x_i} + \frac{\partial}{\partial x_j}[\bar{t}_{ji} + \bar{\rho}\tau_{ji}], \quad \text{for } i = 1, 2, 3 \tag{3.26}$$

$$\begin{aligned}\frac{\partial}{\partial t}(\bar{\rho}E) + \frac{\partial}{\partial x_j}(\bar{\rho}\tilde{u}_j H) = &\frac{\partial}{\partial x_j}\Big[-q_{L_j} - q_{T_j} + \overline{t_{ji}u_i''} - \overline{\rho u_j''\tfrac{1}{2}u_i''u_i''}\Big] \\ &+ \frac{\partial}{\partial x_j}[\tilde{u}_i(\bar{t}_{ij} + \bar{\rho}\tau_{ij})]\end{aligned} \tag{3.27}$$

$$\frac{\partial}{\partial t}(\bar{\rho}k) + \frac{\partial}{\partial x_j}(\bar{\rho}\tilde{u}_j k) = \bar{\rho}\tau_{ij}\frac{\partial \tilde{u}_i}{\partial x_j} - \bar{\rho}\epsilon + \frac{\partial}{\partial x_j}\left[\overline{t_{ji}u_i''} - \overline{\rho u_j'' \tfrac{1}{2}u_i'' u_i''} - \overline{p' u_j''}\right] - \overline{u_i''}\frac{\partial P}{\partial x_i} + \overline{p'\frac{\partial u_i''}{\partial x_i}} \tag{3.28}$$

$$P = \bar{\rho}R\tilde{T} \tag{3.29}$$

The quantities E and H are the *total energy* and *total enthalpy*, and include the kinetic energy of the fluctuating turbulent field, viz.,

$$E = \tilde{e} + \tfrac{1}{2}\tilde{u}_i\tilde{u}_i + k \quad and \quad H = \tilde{h} + \tfrac{1}{2}\tilde{u}_i\tilde{u}_i + k \tag{3.30}$$

For current computations, $k-\omega$ Wilcox (2006) turbulence model [21] has been used. Design features for two-equation turbulence models include [28]

- Distinct resolution of the laminar sub-layer, overlap region and defect layer. [required]
- Skin friction predicted well for simple flows (flat plates, channels, pipes, etc.) [required]
- Asymptotic behavior consistent with turbulence theory and experiment.
- Sharp near-wall peak in Turbulent Kinetic Energy (TKE) well defined and positioned.
- Computationally simple and efficient.
- Acceptable performance for both favorable and adverse pressure gradients.
- Transition predicted accurately for a flat plate.

David Wilcox proposes that integrating through the laminar sublayer be accomplished without damping functions to control the singularity of ϵ at a no-slip surface. He states that not only is the $k-\epsilon$ formulation ill-posed in the laminar sublayer, but that the equations are inaccurate for flows with moderate to severe adverse pressure gradients [29], [30]. Additionally, the damping functions proposed in all low-Reynolds number models cause unnecessary stiffness. The $k-\omega$ equations are well-posed in the laminar sublayer and accurate

for adverse pressure gradients. However, they exchange a singularity at the wall with one in the freestream. GASPex implements several Wilcox $k-\omega$ models. The first is his 1988 $k-\omega$ version based on reference [31]. For free shear flows, Wilcox made improvements to the 1988 model which resulted in the 1998 model [32]. For wall-bounded flows, the '88 and '98 models should perform about the same, while for free shear flows the improvements to the '98 model allow for improved spreading rate predictions.

The improvements resulting in the 1998 model are mainly in the dissipation terms for TKE and ω. The dissipation constants are defined by

$$C_{D_K}^W = \begin{cases} 1 & X_k \leq 0 \\ \dfrac{1+680X_k^2}{1+400X_k^2} & X_k > 0 \end{cases}$$

and

$$C_{D_\omega}^W = \frac{1+70X_\omega}{1+80X_\omega}$$

where X_k is defined as

$$X_k = \frac{1}{\omega^3}\frac{\partial k}{\partial x_j}\frac{\partial \omega}{\partial x_j}$$

where X_ω is defined as

$$X_\omega = \left|\frac{\Omega_{ij}\Omega_{jk}S_{ki}}{(0.09\omega)^3}\right|$$

where Ω is vorticity.

Wilcox has a low Reynolds number version of the 1998 $k-\omega$ model which applies for transitioning flows. In Wilcox's low-Re model, a viscous damping function is multiplied to the eddy viscosity such that $\mu_t = f^W \rho k/\omega$. The damping function is defined as

$$f^W = \frac{\alpha_0^* + R_{t_l}/R_k}{1+R_{t_l}/R_k}, \quad \alpha_0^* = 3/125, R_k = 6,$$

the dissipation coefficient of turbulence kinetic energy is

$$C_{D_k}^{WLR} = \frac{4/15+(R_{t_l}/R_\beta)^4}{1+(R_{t_l}/R_\beta)^4} C_{D_k}^W, \quad R_\beta = 8,$$

and the coefficient of production of specific dissipation rate is

$$C_{p_\omega}^{WLR} = \frac{13/25}{f^W}\Big(\frac{\alpha_0 + R_{t_l}/R_\omega}{1 + R_{t_l}/R_\omega}\Big), \quad \alpha_0 = 1/9,\ R_\omega = 2.95.$$

In 2006, Wilcox released another version of his $k-\omega$ model. The model is implemented in GASPex as described in reference [21]. The major difference between the 2006 and earlier versions of the model are the addition of a cross-diffusion term and a built-in stress-limiter. Wilcox claims that the new model is "as accurate as the Wilcox (1988a) model for attached boundary layers, mildly separated flows and backward-facing steps [21]." The 2006 model is also supposed to be an improvement for shear flow spreading rates and shock-separated flows. The Favre-averaged equations defining the $k-\omega$ model are as follows.

Eddy Viscosity:

$$\mu_T = \frac{\bar{\rho}k}{\tilde{\omega}}, \quad \tilde{\omega} = max\Big\{\omega,\ C_{lim}\sqrt{\frac{2\bar{S}_{ij}\bar{S}_{ij}}{\beta^*}}\Big\}, \quad C_{lim} = \frac{7}{8} \tag{3.31}$$

Turbulence Kinetic Energy:

$$\frac{\partial}{\partial t}(\bar{\rho}k) + \frac{\partial}{\partial x_j}(\bar{\rho}\tilde{u}_j k) = \bar{\rho}\tau_{ij}\frac{\partial \tilde{u}_i}{\partial x_j} - \beta^*\bar{\rho}k\omega + \frac{\partial}{\partial x_j}\Big[\Big(\mu + \sigma^*\frac{\bar{\rho}k}{\omega}\Big)\frac{\partial k}{\partial x_j}\Big] \tag{3.32}$$

Specific Dissipation Rate:

$$\begin{aligned}\frac{\partial}{\partial t}(\bar{\rho}\omega) + \frac{\partial}{\partial x_j}(\bar{\rho}\tilde{u}_j\omega) = \alpha\frac{\omega}{k}\bar{\rho}\tau_{ij}\frac{\partial \tilde{u}_i}{\partial x_j} - \beta\bar{\rho}\omega^2 + \sigma_d\frac{\bar{\rho}}{\omega}\frac{\partial k}{\partial x_j}\frac{\partial \omega}{\partial x_j} \\ + \frac{\partial}{\partial x_j}\Big[\Big(\mu + \sigma\frac{\bar{\rho}k}{\omega}\Big)\frac{\partial \omega}{\partial x_j}\Big]\end{aligned} \tag{3.33}$$

Closure Coefficients and Auxiliary Relations:

$$\alpha = \frac{13}{25}, \quad \beta = \beta_0 f_\beta, \quad \beta^* = \frac{9}{100}, \quad \sigma = \frac{1}{2}, \quad \sigma^* = \frac{3}{5}, \quad \sigma_{do} = \frac{1}{8} \tag{3.34}$$

$$\beta_0 = 0.0708, \quad Pr_T = \frac{8}{9}, \quad \sigma_d = \begin{cases} 0, & \dfrac{\partial k}{\partial x_j}\dfrac{\partial \omega}{\partial x_j} \le 0 \\ \sigma_{do}, & \dfrac{\partial k}{\partial x_j}\dfrac{\partial \omega}{\partial x_j} > 0 \end{cases} \tag{3.35}$$

$$f_\beta = \frac{1 + 85\chi_\omega}{1 + 100\chi_\omega}, \quad \chi_\omega = \Big|\frac{\Omega_{ij}\Omega_{jk}\hat{S}_{ki}}{(\beta^*\omega)^3}\Big|, \quad \hat{S}_{ki} = S_{ki} - \frac{1}{2}\frac{\partial \tilde{u}_m}{\partial x_m}\delta_{ki} \tag{3.36}$$

$$\epsilon = \beta^* \omega k \quad and \quad l = k^{1/2}/\omega \tag{3.37}$$

The turbulence equations are closed by making choices for the empirical constants. Equations (3.31) - (3.37) are referred to as the Wilcox (2006) $k - \omega$ turbulence model [21].

Chapter 4

Methodology

The RANS equations for compressible fluid can be presented in vector form as following

$$\frac{\partial Q}{\partial t} + \frac{\partial F_i}{\partial x_i} = 0, \quad i, j = 1,\ 2,\ 3 \tag{4.1}$$

where

$$Q = \begin{Bmatrix} \bar{\rho} \\ \bar{\rho}\tilde{u}_i \\ \bar{\rho}E \\ \bar{\rho}k \\ \bar{\rho}\omega \end{Bmatrix}, \quad F_i = \begin{Bmatrix} \bar{\rho}\tilde{u}_i \\ \bar{\rho}\tilde{u}_i\tilde{u}_j + P - [\bar{t}_{ij} + \bar{\rho}\tau_{ij}] \\ \bar{\rho}\tilde{u}_i H - [-q_{L_i} - q_{T_i} + \overline{t_{ij}u_j''} - \overline{\rho u_i'' \frac{1}{2} u_j'' u_j''}] - [\tilde{u}_j(\bar{t}_{ji} + \bar{\rho}\tau_{ji})] \\ \bar{\rho}\tilde{u}_i k - \bar{\rho}\tau_{ji}\tilde{u}_j - \Big[\Big(\mu + \sigma^* \frac{\bar{\rho}k}{\omega}\Big)\frac{\partial k}{\partial x_j}\Big] \\ \bar{\rho}\tilde{u}_i \omega - \alpha\frac{\omega}{k}\bar{\rho}\tau_{ji}\tilde{u}_j - \alpha_d\frac{\bar{\rho}}{\omega}k\omega - \Big[\Big(\mu + \sigma\frac{\bar{\rho}k}{\omega}\Big)\frac{\partial \omega}{\partial x_j}\Big] \end{Bmatrix} \tag{4.2}$$

4.1 Finite Volume Formulations

Three inviscid flux schemes, HLLE+, Roe, and AUSM+, have been utilized for the computation. Now, we will see the formulation of these flux schemes.

The flow of a frictionless fluid is governed by the non-linear, hyperbolic partial differential equations known as the Euler equations. A frictionless fluid may also exhibit chemical and/or thermodynamic imperfections. These effects enter the governing equations through the chemical source term for species, $\mathbf{S}$, in the calculation of the species and mixture internal energy, $\widetilde{e}$ and also in turbulence model equation for k and ω. The partial differential equations for a three-dimensional flow of a frictionless fluid with non-equilibrium chemistry and non-equilibrium internal energy may be written in integral form [28],

$$\frac{\partial}{\partial t}\iiint \mathbf{Q}\ dV + \oint_A (\mathrm{F}(\mathbf{Q})\cdot\hat{\mathbf{n}})\ dA = \iiint \mathbf{S}\ dV \tag{4.3}$$

The conserved quantities are denoted by $\mathbf{Q}$, the flux vector by $\mathbf{F}$ and the source term vector by $\mathbf{S}$. The vector $\hat{\mathbf{n}}$ represents the unit normal vector at a cell face, denoted positive when pointing outward from the cell. Every cell in the domain is used as a control volume for application of Equation (4.3). If we denote the cell volume as Vol and the area of each cell face as ΔA, then we can rewrite Eqn. (4.3) exactly as

$$Vol\frac{\partial \bar{\mathbf{Q}}}{\partial t} + \oint_A (\mathrm{F}(\mathbf{Q})\cdot\hat{\mathbf{n}})\ dA = \iiint \mathbf{S}\ dV \tag{4.4}$$

where the cell average of the conserved-variable field is defined as

$$\bar{\mathbf{Q}} = \frac{1}{Vol}\iiint \mathbf{Q}\ dV \tag{4.5}$$

For CFD software like GASPex, the formulation depicted in Equation (4.4) can be approximated on an arbitrarily shaped finite volume as

$$\overbrace{Vol\left(\frac{\partial \bar{\mathbf{Q}}}{\partial q}\right)\frac{\partial q}{\partial t}}^{\text{Time Derivative}} + \overbrace{\sum_A (\mathbf{F}\cdot\hat{\mathbf{n}})\ \Delta A}^{\text{Inviscid and Viscous Fluxes}} = \overbrace{Vol\bar{\mathbf{S}}}^{\text{Source Term}} \tag{4.6}$$

where the the chain rule has been applied to the conservative variables to obtain the time derivative of the primitive variables (i.e., density (ρ), velocity components ($u,\ v,\ w$,) pressure (p), non-equilibrium vibrational energy (e_n), turbulent kinetic energy (k), turbulent dissipation (ω)). GASPex uses the primitive variables (rather than conservative) as a state-vector basis throughout the code for ease and efficiency. In particular, the calculation of the translational temperature and the flux Jacobians are significantly simplified.

4.2 Inviscid Flux Solution

In this section, we will derive three Euler flux schemes , i.e., Roe, AUSM+, and HLLE+, which have been used in the present computations. The derivation has been carried out for 1-D Euler equations for simplicity. An extension to three dimensions is described in GASPex technical reference manual [28].

An integration of the one-dimensional Euler equations in control volume form [33]:

$$\frac{d}{dt}\int_V Q dx dy + \int_{dV} F dy = 0 \tag{4.7}$$

where Q is the vector of dependent variables,

$$Q = \begin{Bmatrix} \rho \\ \rho u \\ \rho e \end{Bmatrix}, \quad \text{and F is the vector of fluxes } F = \begin{Bmatrix} \rho u \\ \rho u u + p \\ \rho e u + p u \end{Bmatrix}$$

The conservation equations (4.7) are applied to a discrete set of control volumes V_i. The solution requires specification of a set of control volumes and algorithms for the temporal and spatial quadratures. Assume a uniform discretization of the x-axis into M cells of length Δx with centroids x_i, $i = 1, ..., M$ as illustrated in Fig. 4.1. The cell faces, located midway between the adjacent centroids, are denoted by $x_{i+1/2}$ for $i = 0, ..., M$.

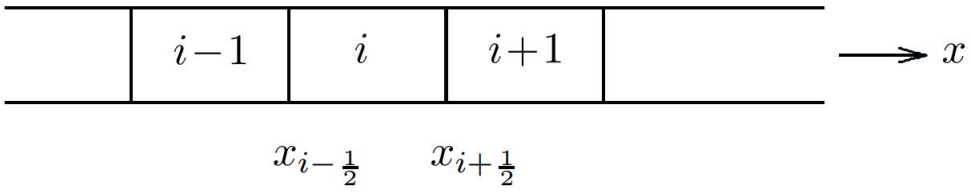

Figure 4.1: Grid of Control Volumes $V_{i-1},\ V_i,\ V_{i+1}$ [33]

Assume a discretization of time into discrete levels t^n, $n = 1, ...$, where

$$t^{n+1} = t^n + \Delta t^n \tag{4.8}$$

For volume i, denote the volume-averaged vector of dependent variables by

$$Q_i(t) = \frac{1}{V_i}\int_{V_i} Q dx dy \tag{4.9}$$

where $V_i = \Delta x\ \Delta y$ and Δy is the (constant) height of each cell. The spatial (flux) quadrature involves faces $i + 1/2$ and $i1/2$. Denote

$$F_{i+1/2} = \frac{1}{A_{i+1/2}} \int_{x_{i+1/2}} F dy \tag{4.10}$$

where $A_{i+1/2} = \Delta y$ is the surface area of the face at $x_i + 1/2$. The flux vector F depends on Q. In the discretization, the dependence on Q can be replaced by an assumed dependence on $Qi + 1/2$, which is some function f of a set of the volume-averaged variables Q_i in the neighborhood of $xi + 1/2$, namely

$$Q_{i+1/2} = f(Q_{i-m}, Q_{i-m+1}, ..., Q_i, ..., Q_{i+n-1}, Q_{i+n}) \tag{4.11}$$

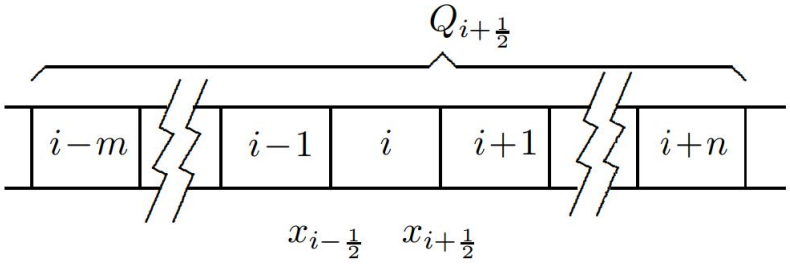

Figure 4.2: Domain of Dependence for $Q_{i+1/2}$ [33]

as illustrated in Fig. 4.2.

Then the Euler equations (4.7) become

$$\frac{dQ_i V_i}{dt} + (F_{i+1/2}\Delta y - F_{i-1/2}\Delta y) = 0 \tag{4.12}$$

Since V_i is assumed to be independent of time,

$$\frac{dQ_i}{dt} + \frac{F_{i+1/2} - F_{i-1/2}}{\Delta x} = 0 \tag{4.13}$$

This is the *semi-discrete* method by which the Euler partial differential equations (4.14) are transformed into a system of ordinary differential equations. This approach is also known as the Method of Lines [34]-[35].

4.2.1 Roe's Scheme

Roe [24], [36] developed an algorithm based on an exact solution to an approximation of the generalized Riemann problem [33]. The solution of the General Riemann Problem requires an iteration to find the contact pressure except in the case of expansion-expansion while Roe's scheme does not require an iterative procedure to find the flux.

Consider the one-dimensional Euler equations in nonconservative differential form,

$$\frac{\partial Q}{\partial t} + A\,\frac{\partial Q}{\partial x} = 0 \tag{4.14}$$

where A is the Jacobian matrix,

$$A(Q) = \frac{\partial F}{\partial Q} = \begin{Bmatrix} 0 & 1 & 0 \\ (\gamma-3)u^2/2 & (3-\gamma)u & \gamma-1 \\ -Hu+(\gamma-1)u^3/2 & H-(\gamma-1)u^2 & \gamma u \end{Bmatrix}$$

where,

$$Q = \begin{Bmatrix} Q_1 \\ Q_2 \\ Q_3 \end{Bmatrix} = \begin{Bmatrix} \rho \\ \rho u \\ \rho E \end{Bmatrix}, \quad F = \begin{Bmatrix} F_1 \\ F_2 \\ F_3 \end{Bmatrix} = \begin{Bmatrix} \rho u \\ \rho u u + p \\ \rho E u + p u \end{Bmatrix} = \begin{Bmatrix} Q_2 \\ \dfrac{Q_2^2}{Q_1} + (\gamma-1)\Big(Q_3 - \dfrac{1}{2}\dfrac{Q_2^2}{Q_1}\Big) \\ \dfrac{Q_2 Q_3}{Q_1} + (\gamma-1)\dfrac{Q_2}{Q_1}\Big(Q_3 - \dfrac{1}{2}\dfrac{Q_2^2}{Q_1}\Big) \end{Bmatrix}$$

The static pressure p is obtained from

$$p = (\gamma-1)(\rho u - \frac{1}{2}\rho u^2)$$

and $H = E + p/\rho$ is the total enthalpy. Here, E is total energy.

Roe sought a solution of the general Riemann problem using an approximate form of the Euler equations

$$\frac{\partial Q}{\partial t} + \tilde{A}(Q_l, Q_r)\frac{\partial Q}{\partial x} = 0 \tag{4.15}$$

where $\tilde{A}(Q_l, Q_r)$ depends on the left and right states Q_l and Q_r of the general Riemann problem (Figure 4.3) and is assumed constant.

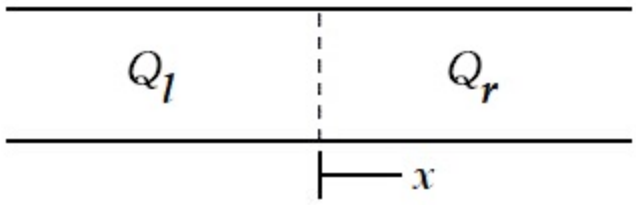

Figure 4.3: Initial condition for General Riemann Problem [33]

$$\frac{dQ_i}{dt} + \frac{F_{i+1/2} - F_{i-1/2}}{\Delta x} = 0 \tag{4.16}$$

The matrix $\tilde{A}$ is an approximation to the exact matrix A and satisfies the following four properties [24].

1. $\tilde{A}$ provides a linear mapping from the vector space of Q to the vector space of F.
2. $\tilde{A}(Q_l, Q_r) \to A(Q)$ as $Q_l \to Q_r \to Q$.
3. For any Q_l and Q_r, $\tilde{A}(Q_l, Q_r)$ x $(Q_l - Q_r) \equiv F_l - F_r$.
4. The eigenvectors of $\tilde{A}(Q_l, Q_r)$ are linearly independent.

These properties are derived and satisfied for $\tilde{A}$ in [33]. Also, $\tilde{A}$ can be written as

$$\tilde{A} = \begin{Bmatrix} 0 & 1 & 0 \\ (\gamma-3)\tilde{u}^2 & (3-\gamma)\tilde{u} & (\gamma-1) \\ -\tilde{H}\tilde{u} + (\gamma-1)\tilde{u}^3/2 & \tilde{H} - (\gamma-1)\tilde{u}^2 & \gamma\tilde{u} \end{Bmatrix} \tag{4.17}$$

where

$$\begin{aligned} \tilde{u} &\equiv \frac{\bar{v_2}}{\bar{v_1}} = \frac{\sqrt{\rho_l}u_l + \sqrt{\rho_r}u_r}{\sqrt{\rho_l} + \sqrt{\rho_r}} \\ \tilde{H} &\equiv \frac{\bar{v_3}}{\bar{v_1}} = \frac{\sqrt{\rho_l}H_l + \sqrt{\rho_r}H_r}{\sqrt{\rho_l} + \sqrt{\rho_r}} \end{aligned} \tag{4.18}$$

The quantities $\tilde{u}$ and $\tilde{H}$ are the *Roe-averaged velocity* and *Roe-averaged total enthalpy*, respectively. The matrix $\tilde{A}(Q_l, Q_r)$ is the *Roe matrix*. Also, $\nu_1 = \sqrt{\rho}$, $\nu_2 = \sqrt{\rho}u$, $\nu_3 = \sqrt{\rho}H$.

The eigenvalues $\tilde{\lambda_i}$ and the right eigenvectors $\tilde{e_i}$ of $\tilde{A}$ may be found directly,

$$\tilde{\lambda}_1 = \tilde{u}, \quad \tilde{\lambda}_2 = \tilde{u} + \tilde{a}, \quad \tilde{\lambda}_3 = \tilde{u} - \tilde{a} \tag{4.19}$$

$$\tilde{e}_1 = \begin{Bmatrix} 1 \\ \tilde{u} \\ \frac{1}{2}\tilde{u}^2 \end{Bmatrix}, \ \tilde{e}_2 = \begin{Bmatrix} 1 \\ \tilde{u}+\tilde{a} \\ \tilde{H}+\tilde{u}\tilde{a} \end{Bmatrix}, \ \tilde{e}_3 = \begin{Bmatrix} 1 \\ \tilde{u}-\tilde{a} \\ \tilde{H}-\tilde{u}\tilde{a} \end{Bmatrix}, \tag{4.20}$$

where $\tilde{a}$ is the speed of sound based on the Roe-averaged total enthalpy and velocity and is given by

$$\tilde{a} = \sqrt{(\gamma-1)(\tilde{H}-\frac{1}{2}\tilde{u}^2)} \tag{4.21}$$

It may be directly verified that the eigenvectors are linearly independent.

The *exact* solution of the *approximate* General Riemann Problem, equation (4.15), is now sought, where $\tilde{A}(Q_l, Q_r)$ is treated as a constant. The Roe matrix may be diagonalized as

$$\tilde{A}(Q_l, Q_r) = \tilde{S}\tilde{\Lambda}\tilde{S}^{-1} \tag{4.22}$$

where $\tilde{S}$ is matrix of right eigenvectors of $\tilde{A}(Q_l, Q_r)$,

$$\tilde{S} = \begin{Bmatrix} 1 & 1 & 1 \\ \tilde{u} & \tilde{u}+\tilde{a} & \tilde{u}-\tilde{a} \\ \frac{1}{2}\tilde{u}^2 & \tilde{H}+\tilde{u}\tilde{a} & \tilde{H}-\tilde{u}\tilde{a} \end{Bmatrix} \tag{4.23}$$

and $\tilde{S}^{-1}$ is

$$\tilde{S}^{-1} = \begin{Bmatrix} 1-(\gamma-1)\tilde{u}^2/2\tilde{a}^2 & (\gamma-1)\tilde{u}/\tilde{a}^2 & -(\gamma-1)/\tilde{a}^2 \\ (\gamma-1)\tilde{u}^2/4\tilde{a}^2-\tilde{u}^2/2\tilde{a} & -(\gamma-1)\tilde{u}^2/2\tilde{a}^2+1/2\tilde{a} & (\gamma-1)/2\tilde{a}^2 \\ (\gamma-1)\tilde{u}^2/4\tilde{a}^2+\tilde{u}^2/2\tilde{a} & -(\gamma-1)\tilde{u}^2/2\tilde{a}^2-1/2\tilde{a} & (\gamma-1)/2\tilde{a}^2 \end{Bmatrix} \tag{4.24}$$

Since $\tilde{A}(Q_l, Q_r)$ is treated as a constant, it is possible to multiply equation (4.15) by $\tilde{S}^{-1}$ to obtain

$$\frac{\partial R}{\partial t} + \tilde{\Lambda}\frac{\partial R}{\partial x} = 0 \tag{4.25}$$

where

$$R = \tilde{S}^{-1}Q = \begin{Bmatrix} R_1 \\ R_2 \\ R_3 \end{Bmatrix} \tag{4.26}$$

and $\tilde{\Lambda}$ is

$$\tilde{\Lambda} = \begin{Bmatrix} \tilde{\lambda}_1 & 0 & 0 \\ 0 & \tilde{\lambda}_2 & 0 \\ 0 & 0 & \tilde{\lambda}_3 \end{Bmatrix} \tag{4.27}$$

The solution of (4.25) is

R_1 = constant on curve C_1 defined by $\dfrac{dx}{dt} = \tilde{\lambda}_1 = \tilde{u}$

R_2 = constant on curve C_2 defined by $\dfrac{dx}{dt} = \tilde{\lambda}_2 = \tilde{u} + \tilde{v}$

R_3 = constant on curve C_3 defined by $\dfrac{dx}{dt} = \tilde{\lambda}_1 = \tilde{u} - \tilde{v}$

C_1, C_2, and C_3 are the characteristic curves of (4.25). The solutions for R_1, R_2, and R_3 are shown together in Fig 4.4.

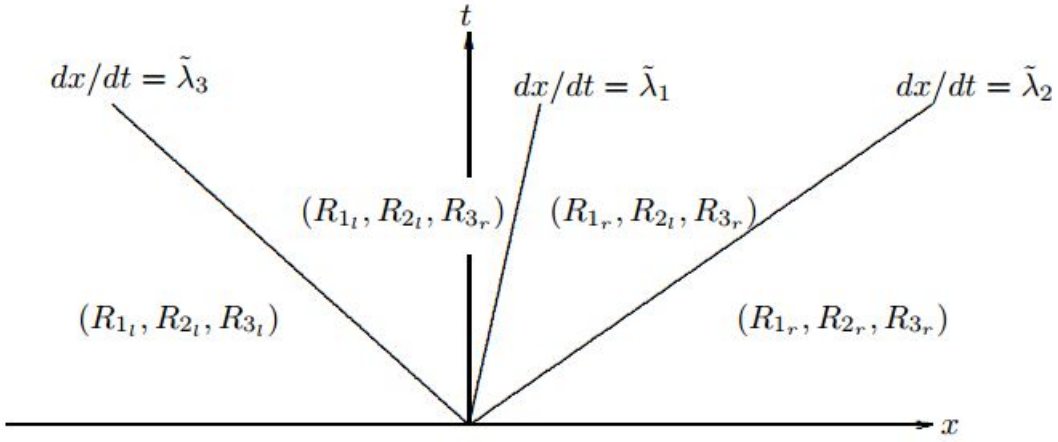

Figure 4.4: Roe's solution to the General Riemann Problem [33]

Consider now the semi-discrete form of Euler equations

$$\frac{dQ_i}{dt} + \frac{F_{i+1/2} - F_{i-1/2}}{\Delta x} = 0 \tag{4.28}$$

The flux $F_{i+1/2}$ is given by,

$$F_{i+1/2} = \frac{1}{2}\left[F_l + F_r + \tilde{S}|\tilde{\Lambda}|\tilde{S}^{-1}(Q^l_{i+1/2} - Q^r_{i+1/2})\right] \tag{4.29}$$

where $F_l = F(Q^l_{i+1/2})$ and $F_r = F(Q^r_{i+1/2})$. This is *Roe's method* for the flux F.

4.2.2 AUSM+ Flux Scheme

The advection upstream splitting method (AUSM) was developed by Liou and Steffen in 1993 [37]. Since that time a number of variations have resulted from the original AUSM algorithm. One variation seems to have gained a lot of attention and is called AUSM+ [22]. The AUSM flux scheme was proposed as a solution to shortcomings of Roe's robust flux scheme with matching (or even surpassing in some cases) robustness and accuracy with less computation cost. Roe's flux scheme has been known to give anomalous results for cases like a supersonic blunt body problem. We will see development of AUSM scheme followed by incarnation of AUSM+ which improves its performance even further.

4.2.2.1 AUSM Flux Scheme

Let us consider the two-dimensional system of Euler equations for perfect gas,

$$\frac{\partial Q}{\partial t} + \frac{\partial F}{\partial x} = 0 \tag{4.30}$$

where,

$$Q^T = (\rho, \rho u, \rho E)$$

$$\text{The inviscid fluxes, } F^T = (\rho u, \rho u^2 + p, \rho u H)$$

$$\text{The total energy, } E = e + \frac{1}{2}u^2 = H - p/\rho$$

The first step is to recognize that the inviscid flux vector F consists of two physically distinct parts, namely *convective* and *pressure* terms:

$$F = \begin{pmatrix} \rho \\ \rho u \\ \rho H \end{pmatrix} u + \begin{pmatrix} 0 \\ p \\ 0 \end{pmatrix} = F^{(c)} + \begin{pmatrix} 0 \\ p \\ 0 \end{pmatrix}$$

The convective terms can now be considered as passive scalar quantities convected by a *suitably* defined velocity u at the cell interface. On the other hand, the pressure flux terms are governed by the acoustic wave speeds. Thus Liou and Steffen [37] proposed to discretize

the two components separately. At an interface $L < \frac{1}{2} < R$, the convective terms can be effectively written as,

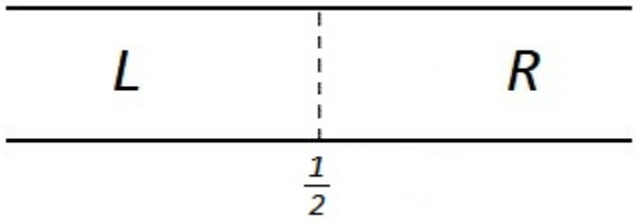

Figure 4.5: Interface between Left and Right States of the Flow

$$F_{1/2}^{(c)} = u_{1/2} \begin{pmatrix} \rho \\ \rho u \\ \rho H \end{pmatrix}_{L/R} = M_{1/2} \begin{pmatrix} \rho a \\ \rho a u \\ \rho a H \end{pmatrix}_{L/R} = M_{1/2} \phi_{L/R}, \tag{4.31}$$

where,

$$(\phi)_{L/R} = \begin{cases} (\phi)_L, & \text{if } M_{1/2} \geq 0, \\ (\phi)_R, & \text{otherwise.} \end{cases} \tag{4.32}$$

Note that $(\phi)_L$, $(\phi)_R$ and $(\phi)_{L/R}$ can also be written as ϕ_j, ϕ_{j+1} and $\phi_{j+1/2}$ respectively, where j is coordinate system index.

This formulation opens up a whole new family of schemes based upon the formulation chosen for the advective velocity $M_{1/2}$. Liou and Steffen [37] chose to represent this velocity as a combination of the wave speeds $(M \pm 1)$ traveling towards the interface $(\frac{1}{2})$ from the adjacent L and R cells. This is formally written, by combining the contributions from both the "left" and "right" states, as

$$M_{\pm} = M_L^{+} + M_R^{-}$$

Various ways of defining $M^{\pm}$ exist. In derivation of AUSM [37], Van Leer splitting [38] was chosen.

$$M^{\pm} = \begin{cases} \pm\frac{1}{4}(M \pm 1)^2, & \text{if } |M| \leq 1; \\ \frac{1}{2}(M \pm |M|), & \text{otherwise.} \end{cases}$$

Now turning to pressure term by writing,

$$p_{1/2} = p_L^+ + p_R^-.$$

Again the pressure splitting is weighted using the polynomial expansion of the characteristic speeds $(M \pm 1)$. According to Liou et al. [39] , the pressure splitting can be expressed in terms of second order polynomials $(M \pm 1)^2$ as

$$p_3 : p^{\pm} = \begin{cases} \frac{p}{4}(M \pm 1)^2(2 \mp M), & \text{if } |M| \leq 1; \\ \frac{p}{2}(M \pm |M|)/M, & \text{otherwise.} \end{cases}$$

First order form of the above expansion ca be written as,

$$p_1 : p = \begin{cases} \frac{p}{2}(1 \pm M), & \text{if } |M| \leq 1; \\ \frac{p}{2}(M \pm |M|)/M, & \text{otherwise.} \end{cases}$$

The above formulas can be rewritten as,

$$\begin{pmatrix} \rho u \\ \rho uu + p \\ \rho uH \end{pmatrix}_{1/2} = M_{1/2}\, \frac{1}{2} \left[\begin{pmatrix} \rho a \\ \rho au \\ \rho aH \end{pmatrix}_L + \begin{pmatrix} \rho a \\ \rho au \\ \rho aH \end{pmatrix}_R \right] - \frac{1}{2}\, |M_{1/2}|\, \Delta_{1/2} \begin{pmatrix} \rho a \\ \rho au \\ \rho aH \end{pmatrix} + \begin{pmatrix} 0 \\ p_L^+ + p_R^- \\ 0 \end{pmatrix}$$

where $\Delta_{1/2}(\bullet) = \{\bullet\}_R - \{\bullet\}_L$. Here, the first term on the right side is the Mach-number-weighted average instead of a simple average of "L" and "R" states. The second term is the numerical dissipation, rendering the flux formula upwinding, and it has merely a scalar coefficient $|M_{1/2}|$, requiring on $O(n)$ operations, in contrast to $O(n^2)$ operations by the Roe matrix. A significant savings by a factor of three for 2D explicit calculation has been claimed by the author [37].

The above splitting of both the advective term and pressure term completely define the inviscid flux vector. For viscous terms, the usual central-average representation is used at

the interface. Liou et al [37] have compared results from the AUSM splitting technique with Roe and Van Leer schemes for problems like 2D viscous conical flow, 2D inviscid flow around NACA four-digit series airfoil (under regimes similar to GAMM workshop [40]), laminar SBLI and supersonic flow over a circular cylinder which showed that AUSM's performance rivals or surpasses that of other two.

4.2.2.2 AUSM+ Flux Scheme

Flux-vector splitting (FVS) schemes (like Van Leer) are efficient to solve, while the flux difference splitting (FDS) schemes (like Roe) have the advantage of increased accuracy. AUSM tries to be numerically efficient, while attaining a high level of accuracy. AUSM+ has been introduced in 1996 by Liou [22] with the purpose of improving its predecessor, AUSM. AUSM+ features the following properties:

1. Exact resolution of 1D contact and shock discontinuities
2. Positivity preserving of scalar quantity such as density
3. Free of "carbuncle phenomenon"
4. Free of oscillations at the slowly moving shock
5. Algorithmic simplicity
6. Easy extension to treat other hyperbolic systems
7. Improvement in accuracy over its predecessor AUSM and other popular schemes

The differences among all numerical schemes lie essentially in the definition of the numerical flux $f_{j+1/2}$ evaluated at the cell interface. AUSM+ has been derived containing AUSM as its special case. A set of more general Mach number and pressure splitting functions are used in the AUSM, resulting in improvement in accuracy, such as removing post shock overshoot and a glitch in the slowly moving shock problem.

The AUSM scheme simply consists of two steps: (1) the definition of $M^{\pm}$ and $p^{\pm}$, followed by (2), a simple upwind selection advection of $\phi_{j+1/2}$ (Equation (4.32)) . In AUSM+, Liou [22] proposes to deal with the genuinely nonlinear field associated with the eigenvalues

$(u \pm a)$ in the first step and the linearly degenerate field associated with the eigenvalue (u) in the second step. In other words, the interface (numerical) velocity and pressure will be determined by considering the nonlinear field when we define their explicit functional forms. The key for unifying the Mach number and velocity formulations [37] is the notion of the common speed of sound defined at the cell interface. This notion turns out to be very useful as it allows the exact capturing of a shock wave in AUSM+.

Let the common speed of sound be denoted by $a_{1/2}$. We can rewrite the numerical convective flux in equation (4.31) as,

$$F_{1/2}^{(c)} = M_{1/2} a_{1/2} \Phi_{L/R}, \quad \Phi = (\rho,\, \rho u,\, \rho H)^T \tag{4.33}$$

Consider now the semi-discrete form of Euler equations (4.28). The convective flux $F_{i+1/2}$ is given by,

$$F_{i+1/2} = M_{i+1/2}\; a_{i+1/2}\; \frac{1}{2}\left[\Phi_{i+1/2}^{L} + \Phi_{i+1/2}^{R}\right] - \frac{1}{2}\;|M_{i+1/2}|\; a_{i+1/2}\; \Delta_{i+1/2}\Phi + p_{i+1/2} \tag{4.34}$$

We note that the quantity Φ in equation (4.34) differs by a factor a from that used in the AUSM, as shown in equation (4.31). Both $\phi_{L/R}$ and $\Phi_{L/R}$ are given by simple upwinding as shown in equation (4.32). It remains to define $(M_{i+1/2},\, p_{i+1/2})$ and $a_{i+1/2}$ for which a detailed framework has been developed in [22].

Comparison reveals clearly that a striking difference in form between the FVS and FDS lies in whether the dissipation matrix (or scalar) is differenced. In this regard, the present scheme may appear formally close to a FDS, but it differs in the averaged term. On the other hand, the current method retains the efficiency of the Van Leer scheme in defining the dissipation term. Consequently, the present scheme is neither FDS nor FVS, but rather a hybrid one.

4.2.3 HLLE+ Flux Scheme

An improved HLLE+ scheme has been suggested by Park and Kwon [23] based on Einfeldt's HLLEM scheme [41], a typical HLL solver. A HLL (Harten-Lax-van Leer) solver

is a mathematical theory of the upstream difference scheme and the Godunov-type solvers proposed by Harten et al. [42] in 1983. The recent interest in Godunov-type methods was engendered by van Leer, who realized the importance of Godunov's method and invented a second-order extension. In 1991, HLLEM scheme was modified by Einfeldt to enhance the resolution of HLLE (1988) scheme [43] comparable to that of Roe's scheme. In the following, we will go through a brief development of the HLLE+ scheme beginning with the HLL solver. For the current solution procedure, the HLLE+ dissipation constant, Delta, has been set to 2.5. Increasing the value of Delta results in the more dissipative HLLE scheme being applied to a larger portion of the domain.

4.2.3.1 HLL (Harten-Lax-van Leer) Solver

In 1983, Harten et al [42] considered numerical solutions of the initial-value problem for hyperbolic systems of conservation laws,

$$\frac{\partial Q}{\partial t} + \frac{\partial F(Q)}{\partial x} = 0,\ Q(x,0) = Q_0(x), \quad -\infty < x < +\infty \tag{4.35a}$$

Here $Q(x,t)$ is a column vector of m unknowns and $F(Q)$, the flux, is a vector-valued function of m components.We can write above equation in matrix form

$$\frac{\partial Q}{\partial t} + A\frac{\partial Q}{\partial x} = O,\ A(Q) = \frac{\partial F}{\partial Q} \tag{4.35b}$$

Equation (4.35) is called hyperbolic if all eigenvalues of the Jacobian matrix A are real. We assume that the eigenvalues $a_1(Q), ..., a_m(Q)$ are distinct and arranged in an increasing order.

Now, consider systems of conservation laws (4.35) that possess an entropy function $U(Q)$, defined as follows:

(i) U is a convex function of Q, i.e., $\dfrac{\partial^2 U}{\partial Q^2} > 0$.

(ii) U satisfies

$$\frac{\partial U}{\partial Q}\frac{\partial F}{\partial Q} = \frac{\partial f}{\partial Q} \tag{4.36}$$

where f is some other function called *entropy flux* (see [44]).

Numerical approximations to weak solutions of (4.35) that are obtained by 3-point explicit schemes in conservation form:

$$P_j^{n+1} = P_j^n - \lambda F_{j+1/2}^n + \lambda F_{j-1/2}^n, \quad \lambda = \tau/\Delta, \tag{4.37a}$$

where

$$F_{j+1/2}^n = F(P_j^n, P_{j+1}^n). \tag{4.37b}$$

Here $P_j^n = P(j\Delta, n\tau)$, and $F(Q, P)$ is a *numerical flux*. We require the numerical flux to be consistent with the physical flux in the following sense:

$$F(Q, Q) = F(Q) \tag{4.37c}$$

Harten et al [42] reviewed some of the recent developments in upstream difference schemes through a unified representation, in order to enable comparison between the various schemes. Special attention was given to the Godunov-type schemes that result from using an approximate solution of the Riemann problem. For schemes based on flux splitting, the approximate Riemann solution can be interpreted as a solution of the collisionless Boltzmann equation. Upstream-differencing schemes attempt to discretized hyperbolic partial differential equations by using differences biased in the direction determined by the sign of the characteristic speed.

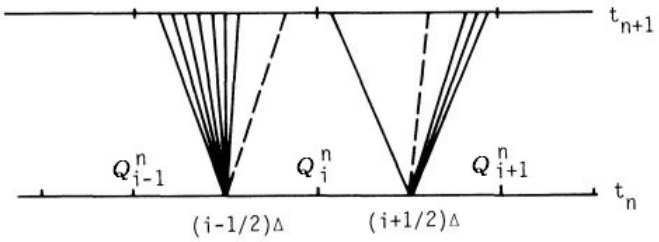

Figure 4.6: Godunov's Method in Physical Space [43]

Harten et al presented a review of basic concepts and derivation of design principles (including review of some properties of the equations essential to their proper numerical

approximation), a straightforward extension of linear upstream differencing to nonlinear systems, physical picture due to Godunov which is useful to interpret certain schemes and to construct new schemes and flux splitting. It has been noted that linear upstream difference schemes contain a large amount of artificial viscosity, except for those components where a_k, a stability criterion of upstream differencing scheme, is small, in particular where $a_k = 0$. The same appears to be true for all upstream difference schemes for nonlinear conservation laws: when all characteristic speeds are not zero, each component is treated like a scheme with a hefty amount of artificial viscosity, smearing discontinuities. There is, however, quite a distinction among the schemes when one of the characteristic speeds is zero; this shows up in the way each scheme resolves a stationary shock, centered transonic rarefaction wave, and stationary contact discontinuity.

A difference scheme in conservation form (4.37) is said to be an upstream scheme if:

(i) For Q and P nearby states, a linear approximation to the numerical flux F(Q, P) is,

$$F(Q,P) = A^{+}Q + A^{-}P \tag{4.38}$$

(ii) When all signal speeds associated with the numerical flux $F(Q,P)$ are > 0,

$$F(Q,P) = F(Q), \tag{4.39}$$

When all signal speeds are < 0,

$$F(Q,P) = F(P) \tag{4.40}$$

The relevant signal speeds generally differ from the characteristic speeds of the states Q and P.

The most critical difference in performance occurs in resolving a stationary shock:

$$Q_0(x) = \begin{cases} Q, & x < 0, \\ P, & x > 0, \end{cases} \qquad F(Q) = F(P), \qquad f(P) < f(Q) \tag{4.41a}$$

The lack of numerical dissipation allows the design of schemes that perfectly resolve stationary shocks, i.e., Equation (4.41a) is a steady solution of the numerical scheme.

$$\text{The condition for that is,} \quad d(Q,P)=0 \quad \text{if } F(Q)=F(P), \qquad f(P)<f(Q) \tag{4.41b}$$

On the other hand

$$Q_0(x)=\begin{cases} Q, & x<0, \\ P, & x>0, \end{cases} \qquad f(P)<f(Q) \tag{4.41c}$$

is not an admissible discontinuity and should not be a steady solution of the finite difference scheme, i.e., we require that

$$d(Q,P)\neq 0 \quad \text{if } F(Q)=F(P), \qquad f(P)>f(Q) \tag{4.41d}$$

The danger that a given upstream scheme selects a nonphysical solution will occur only for stationary or near-stationary discontinuities; otherwise there is enough numerical viscosity to enforce the selection of a physically relevant solution. Hence there are two options in designing an upstream-differencing scheme for solving problems with discontinuous solution:

1. To switch direction of differencing in a way that will effectively introduce nonlinear dissipation at the expense of slightly spreading the shock

2. To satisfy equation (4.41) and thus get perfect resolution of a stationary shock, but to add a mechanism for checking the admissibility of the discontinuity.

Godunov, in his construction of the "best" monotone scheme [45], used the exact solutions of local Riemann problems to obtain an upstream differencing scheme. The solution of the Riemann problem

$$\frac{\partial Q}{\partial t}+\frac{\partial F(Q)}{\partial x}, \quad Q(x,0)=\begin{cases} Q_L, & x<0, \\ Q_R, & x>0, \end{cases}$$

depends only on the states Q_L and Q_R and the ratio x/t; it will be denoted by $Q(x/t;Q_L,Q_R)$.

From solutions of Godunov's scheme for the local Riemann problem, it has been concluded [42] that due to averaging, the Godunov scheme does not make use of all the information contained in the exact solution of the Riemann problem. Therefore, replacement of the

exact solution to the Riemann problem $Q(x/t; Q_L, Q_R)$ by an approximation $w(x/t; Q_L, Q_R)$ in the local Riemann problem solutions for piecewise-constant approximation of Godunov Scheme has been considered. The latter can have a much simpler structure as long as it does not violate the essential properties of conservation and entropy inequality.

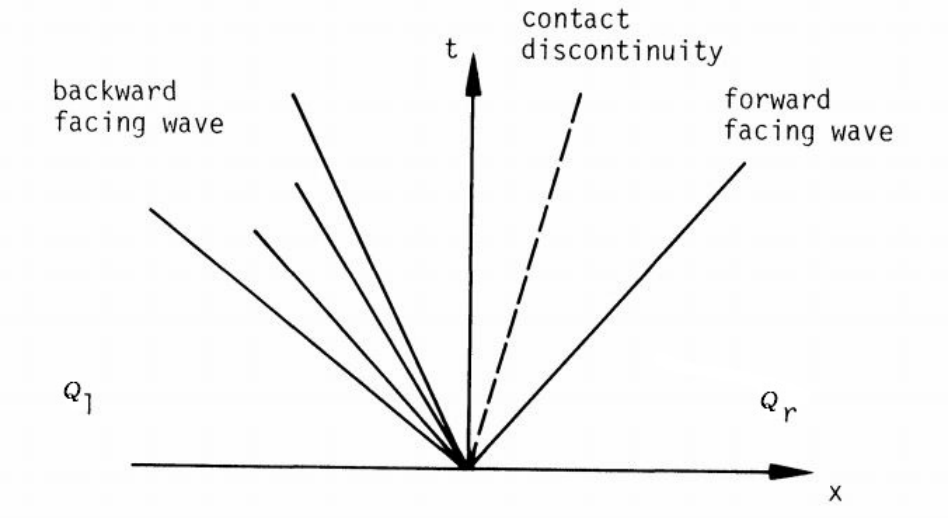

Figure 4.7: The Solution of the Riemann Problem in Physical Space [43]

The solution to the Riemann problem consists of four constant states separated by three elementary waves. The backward and forward facing wave is either a rarefaction or shock wave. The solution to the Riemann problem incorporates a large amount of information about the physical system that is modeled by equation (4.35). It includes, for example, the directions and strength of the disturbances that emerge from the nonlinear interaction of two constant states. For that reason, the solution of the Riemann problem is a natural "building block" for the construction of upstream differencing schemes.

Further, construction of Roe's Riemann solver has been discussed and an alternative scheme proposed which require less computational effort than either Godunov's or Roe's scheme. It has been indicated that more experimentation is needed to see whether its accuracy is comparable. Also, generalizations of the upstream differencing scheme to nonlinear systems of conservation laws that are based on the flux-splitting and stability analysis of

linear case (Boltzmann-type schemes) has been presented. It has been concluded that split-flux scheme of van Leer [46] for the Euler equations can represent a stationary shock with, at best, one intermediate state, just as the Osher [47] scheme. A contact discontinuity, however, will keep on spreading with the use of any split flux scheme. This follows immediately from the diffusive nature of the underlying Boltzmann model.

4.2.3.2 HLLE Flux Scheme

The disadvantage of Godunov's method and its higher-order extension was the difficulty of solving the nonlinear Riemann problem exactly, especially for materials with complex equations of state. The exact solution of the Riemann problem required an iterative procedure, which leads to relatively complex and time-consuming numerical codes. Since computational efficiency was a major requirement for applied numerical methods, this had restricted the extensive applications of Godunov-type methods. To overcome this drawback, several approximations to the Riemann problem had been developed. For ideal (polytropic) equations of state there were, by then, particular approximate "Riemann solvers" available. These linear approximations were also of interest in the field of aerodynamics where they provide a foundation for the construction of more elaborate schemes.

In 1988, Einfeldt [43] proposed a new Riemann solver, HLLE, which kept the computing time extremely low, while remaining the essential properties of Godunov's method and provided an attractive alternative on which to construct higher-order extensions. A numerical approximation for the largest and smallest signal velocity in the Riemann problem was derived in contrast to previous Riemann solvers, where a numerical approximation for the pressure and the velocity at the contact discontinuity was computed. Having obtained the numerical signal velocities, the theory proposed by HLL had been used to obtain the full approximation. A stability condition for the numerical signal velocities had been derived. Einfeldt supported his scheme with numerical results for the one- and two-dimensional compressible gas dynamics equations.

Let's consider the Euler equations for an inviscid compressible flow. The conservation

form of these equations in one Cartesian space variable is

$$\frac{\partial Q}{\partial t} + \frac{\partial F(Q)}{\partial x} = 0 \tag{4.42}$$

where the conserved quantities Q and fluxes F are:

$$Q = \begin{pmatrix} \rho \\ \rho u \\ E \end{pmatrix}, \qquad F(Q) = \begin{pmatrix} m \\ m^2/\rho + p \\ \frac{m}{\rho}(E+p) \end{pmatrix}$$

Here, ρ is the density, $\rho u = m$ is the momentum per unit length and $E = \rho\varepsilon + \frac{1}{2}\rho u^2$ is the total energy per unit length. The physical variables u and ε are the velocity and the internal energy per unit mass. The pressure p is related to the conserved quantities through the equation of state

$$p = p(\tau,\ \varepsilon),$$

where $\tau = 1/\rho$ is the specific volume. In the case of an ideal equation of state we have

$$p = (\gamma - 1)\frac{\varepsilon}{\tau}$$

In [43], Einfeldt concentrated on an ideal equation of state and indicated possible extension to general equations of state.

The HLL-Riemann solver, theoretically discussed by Harten, Lax and van Leer [10], extracts the information about the signal velocities from the full Riemann problem. In Figure 4.8 , $b^l_{i+1/2}$ and $b^r_{i+1/2}$ are Lipschitz-continuous approximations to the smallest and largest physical signal velocities. In contrast to original version, Einfeldt didn't assume that the numerical signal velocities $b^l_{i+1/2}$, $b^r_{i+1/2}$ are lower and upper bounds for the physical signal velocities $a^l_{i+1/2}$, $a^r_{i+1/2}$. Stability bounds for the numerical signal velocities were derived separately. Einfeldt claims that HLL Riemann solver (Equation (4.43)) spreads the discontinuity and is a rather rough approximation to the exact solution. HLL solver consists of three constant states, i.e.,

$$\omega_{i+1/2}(x'/t) = \begin{cases} Q_i, & \text{for } x' < b^l_{i+1/2}t, \\ Q_{i+1/2}, & \text{for } b^l_{i+1/2}t < x' < b^r_{i+1/2}t, \\ Q_{i+1}, & \text{for } b^r_{i+1/2}t < x' \end{cases} \tag{4.43}$$

where $\omega_{i+1/2}(x^{'}/t)$ is the solution to the Riemann problem at the cell interface $x_{i+1/2} = (i + 1/2)\Delta$.

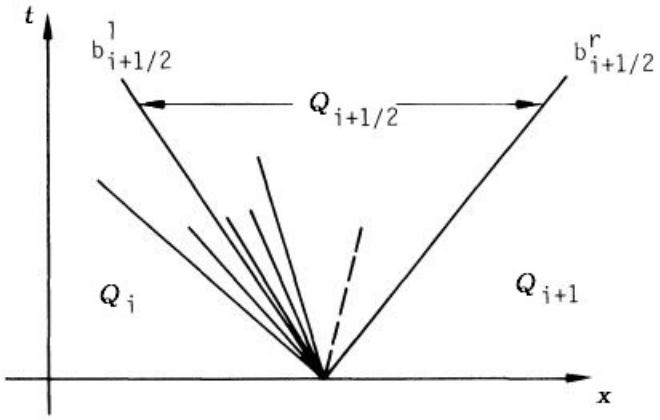

Figure 4.8: Approximate Solution of the Riemann Problem [43]

Einfeldt pointed out that the information of the contact discontinuity is buried in the average state $Q_{i+1/2}$. A contact wave is proposed as a weak solution of equation (4.42) of the form,

$$Q(x,t) = \omega(x,t)(1, u, \frac{1}{2}u^2)^T, \tag{4.44}$$

where u is the constant velocity of propagation of the wave. We therefore recover the information about the contact discontinuity, by modifying the average state $Q_{i+1/2}$ in (4.43),

$$\omega_{i+1/2} = \begin{cases} Q_i, & \text{for } x^{'}/t < b^l_{i+1/2}t, \\ Q_{i+1/2} + \delta_{i+1/2}(x - \bar{u}_{i+1/2}t)\eta^2_{i+1/2}R^2_{i+1/2}, & \text{for } b^l_{i+1/2}t < x^{'}/t < b^r_{i+1/2}t, \\ Q_{i+1}, & \text{for } b^r_{i+1/2}t < x^{'}/t \end{cases} \tag{4.45}$$

Where

$$R^2_{i+1/2} = (1,\ \bar{u}_{i+1/2},\ \frac{1}{2}\bar{u}^2_{i+1/2})^T,$$

and

$$\eta^2_{i+1/2} = l^2_{i+1/2}(Q_{i+1} - Q_i)$$

with

$$l^2_{i+1/2} = \Big(1 - \frac{\gamma-1}{2}\frac{\bar{u}^2_{i+1/2}}{\bar{c}^2_{i+1/2}}, (\gamma-1)\frac{\bar{u}_{i+1/2}}{\bar{c}^2_{i+1/2}}, \frac{(1-\gamma)}{\bar{c}^2_{i+1/2}}\Big).$$

$\delta_{i+1/2}$ is an important anti-diffusion parameter for stability condition. Observe that $R^2_{i+1/2}$ is the second eigenvector of the Jacobian matrix A (Equation (4.35b)) and that $\eta^2_{i+1/2}$ is an approximate value for the projection from $Q_{i+l} - Q_i$ onto this eigenvector. $\bar{u}_{i+1/2}$ and $\bar{c}_{i+1/2}$ are numerical approximations of the velocity and the sound speed at the contact discontinuity,

$$\bar{u}_{i+1/2} = \frac{b^r_{i+1/2} + b^l_{i+1/2}}{2}, \quad \bar{c}_{i+1/2} = \frac{b^r_{i+1/2} - b^l_{i+1/2}}{2}$$

The approximate solution (4.45) is thus completely defined by the numerical signal velocities. The modification of the average state $Q_{i+1/2}$ does not change the integral form of Riemann solver. Therefore, the Riemann solver (4.45) remains in conservation form. The numerical flux of the corresponding Godunov-type method is defined by,

$$\begin{aligned} h_{i+1/2} &= F(Q_i) - \frac{1}{\tau}\int_{-\Delta/2}^{0} \omega_{i+1/2}(x'/\tau)dx' + \frac{\Delta}{2}Q_i \\ &= g_{i+1/2} - b^+_{i+1/2}b^-_{i+1/2}\frac{\tau}{2}\delta_{i+1/2}\eta^2_{i+1/2}R^2_{i+1/2}, \end{aligned} \tag{4.46}$$

where numerical flux,

$$g_{i+1/2}(Q_i, Q_{i+1}) = \begin{cases} F(Q_i) & \text{for } 0 < b^l_{i+1/2} \\ \dfrac{b^r_{i+1/2}F(Q_i) - b^l_{i+1/2}F(Q_{i+1})}{b^r_{i+1/2} - b^l_{i+1/2}} + \dfrac{b^l_{i+1/2}b^r_{i+1/2}}{b^r_{i+1/2} - b^l_{i+1/2}}(Q_{i+1} - Q_i) & \text{for } b^l_{i+1/2} < 0 < b^r_{i+1/2} \\ F(Q_{i+1}) & \text{for } b^r_{i+1/2} < 0 \end{cases}$$

The resolution of a shock wave or contact discontinuity is largely determined by the numerical dissipation of the difference scheme. In dissipation and stability analysis, Einfeldt noted that for a contact discontinuity the dissipation of the methods of Roe and Godunov is the same, whereas the dissipation of the Godunov-type method is larger. The Godunov-type method therefore spreads a contact discontinuity over more grid points.

Harten, Lax and van leer [42] leave open the question of how to compute approximations for the signal velocities $b^r_{i+1/2}$. Einfeldt [43] describes two algorithms for this essential part of the Godunov-type method. The most accurate resolution of shock discontinuities

are obtained if we choose the smallest and largest eigenvalues of a Roe matrix $A_{i+1/2}$ for the signal velocities. For a γ-law (ideal) equation of state a special matrix $A_{i+1/2}$ was constructed by Roe [24]. The minimal and maximal eigenvalues of this matrix are,

$$b^l_{i+1/2} = \bar{u}_{i+1/2} - \bar{c}_{i+1/2}, \tag{4.47a}$$

$$b^r_{i+1/2} = \bar{u}_{i+1/2} + \bar{c}_{i+1/2}, \tag{4.47b}$$

with $\rho_i H_i = E_i + p_i$. For a more general equation of state (at that time) a Roe average matrix $A_{i+1/2}$ was not available in the literature and may also lead to a more complex algorithm. Here, $\bar{c}_{i+1/2}$ is averaged speed of sound at cell interface $x_{i+1/2} = (i + 1/2)\Delta$.

Next, a possible extension of Roe signal velocities to more general equations of state was derived. The signal velocities are as follows,

$$b^l_{i+1/2} = \bar{u}_{i+1/2} - \bar{d}_{i+1/2}, \quad b^r_{i+1/2} = \bar{u}_{i+1/2} + \bar{d}_{i+1/2}, \tag{4.48}$$

Since

$$\bar{d}_{i+1/2} > \bar{c}_{i+1/2},$$

where

$$\begin{aligned} \bar{c}_{i+1/2} &= (\gamma - 1)(\bar{H}_{i+1/2} - \tfrac{1}{2}\bar{u}^2_{i+1/2}) \\ &= (\gamma - 1)\left(\frac{\sqrt{\rho_i}H_i + \sqrt{\rho_{i+1}}H_{i+1}}{\sqrt{\rho_i} + \sqrt{\rho_{i+1}}} - \frac{1}{2}\left(\frac{\sqrt{\rho_i}u_i + \sqrt{\rho_{i+1}}u_{i+1}}{\sqrt{\rho_i} + \sqrt{\rho_{i+1}}} \right)^2 \right) \end{aligned} \tag{4.49}$$

where $\bar{u}_{i+1/2}$ and $\bar{H}_{i+1/2}$ are the averaged velocity and averaged total enthalpy.

These signal speeds satisfy the following stability requirement for any gas law.

$$b^-_{i+1/2} \leqq \alpha^k_{i+1/2} \leqq b^+_{i+1/2} \quad \text{for } k = 1, ..., 3.$$

where $\alpha^k_{i+1/2}$ is the eigenvalue of Roe matrix $A_{i+1/2}$.

Moreover, Einfeldt compared results from HLLR (Roe) and HLLE (Einfeldt) schemes for Sod's 1D problem, Lax's 1D problem, Riemann 1D problem where the states v_l and v_r

are connected by a rarefaction and 2D test problem which is the focusing of a plane shock wave in air ($\gamma = 1.4$) by a parabolic reflector wave [48] using a Cyber 175 computer.

It was concluded [43] that the great advantage of the Riemann solver (4.43) is its simplicity. The approximation substantially reduces the program complexity while retaining the essential features of Godunovs method, especially the accurate approximation of shock waves. A drawback of the Godunov-type method (4.45) is that the resolution of a nearly stationary contact discontinuity requires more grid points as Godunov's method. This problem was overcome by introducing an anti-diffusion term in the linear degenerate field. If we choose the smallest and largest eigenvalues of the Roe linearization [24] for the numerical signal velocities, then the Godunov-type method with the modified numerical flux function (4.45) becomes identical with Roe's flux function. Thus we obtained a new interpretation of Roe's scheme [24]. The successful application to the shock focusing problem shows the usefulness of the Riemann solver in a higher-order Godunov-type scheme.

4.2.3.3 HLLEM Flux Scheme

In 1991, Einfeldt et al [41] suggested a modified HLLE flux scheme which was denoted the HLLEM flux scheme. When the energy of a flow is largely kinetic, many conservative differencing schemes may fail by predicting non-physical states with negative density or internal energy. Positively conservative was described as the subclass of schemes that by contrast always generate physical solutions from physical data and show that the Godunov method is positively conservative. It is also shown [41] that no scheme whose interface flux derives from a linearized Riemann solution can be positively conservative. However, the Harten-Lax-van Leer (HLLE) scheme is positively conservative under certain conditions on the numerical wave speeds. This observation allowed the linearized schemes to be rescued by modifying the wave speeds employed.

Highly energetic flows often contain regions in which the dominant energy mode is kinetic. If this kinetic energy is computed from a conservative numerical approximation for the conservation laws of mass and momentum and then subtracted from a conservative approximation of the conservation law for the total energy, then the resulting internal energy may be negative. This of course leads to a failing of the numerical scheme. Attempting to

replace negative internal energy values by positive ones leads to a non-conservative scheme and may result in a wrong shock position or an exponential error growth. Considerable importance attaches therefore to any numerical scheme for which the internal energy and density remain positive throughout the computational process. Einfeldt et al [41] denoted such schemes as positively conservative. In their paper they established that for the Euler equations of gas dynamics, involving problems in any number of space dimensions:

(i) Godunov's scheme [45] is positively conservative

(ii) no Godunov-type scheme based on a linearized Riemann solution is positively conservative

(iii) that the HLLE-scheme [42], [43] is positively conservative, provided the absolute value of the maximal and minimal wave speeds satisfy certain stability bounds

The results obtained in [43] also indicate how to fix up the methods studied under (ii).

The theory of Godunov-type schemes are well developed for scalar conservation law on Cartesian grids. Difficulties arise when these methods are applied to non-linear hyperbolic systems of conservation laws.

The HLLE scheme [43] given by (4.45) in 1988 was modified by Einfeldt et al [41] in 1991 as below,

$$\omega_{HLLEM}(x^{'}/t; i+1/2) = \begin{cases} Q_i, & \text{for } x^{'}/t < b^l_{i+1/2}t, \\ Q_{i+1/2} + (x - \bar{u}_{i+1/2}t)(\hat{\delta}^2_{i+1/2}\hat{\alpha}^2_{i+1/2}\hat{\mathbf{R}}^2_{i+1/2} + \hat{\delta}^3_{i+1/2}\hat{\alpha}^3_{i+1/2}\hat{\mathbf{R}}^3_{i+1/2}), & \\ \qquad \text{for } b^l_{i+1/2}t < x^{'}/t < b^r_{i+1/2}t, & \\ Q_{i+1}, \quad \text{for } b^r_{i+1/2}t < x^{'}/t & \end{cases} \tag{4.50}$$

where $\mathbf{R}^2_{1+1/2} = \mathbf{R}^2(\hat{\mathbf{w}}_{i+1/2})$ and $\mathbf{R}^3_{1+1/2} = \mathbf{R}^3(\hat{\mathbf{w}}_{i+1/2})$ are the second and third right eigen-vectors of the Jacobian matrix $d\mathbf{F}(\hat{\mathbf{w}}_{i+1/2}) = A(\hat{\mathbf{w}}_{i+1/2})$ evaluated at an average state $\hat{\mathbf{w}}_{i+1/2} = (\hat{\rho}, \hat{u}, \hat{v}, \hat{c})^T$. Also, $\hat{\alpha}^2_{i+1/2} = \alpha^2(\hat{\mathbf{w}}_{i+1/2})$ and $\hat{\alpha}^3_{i+1/2} = \alpha^3(\hat{\mathbf{w}}_{i+1/2})$ are the coefficients of the projection of $(Q_{i+1} - Q_i)$ onto these eigenvectors; i.e.,

$$Q_{i+1} - Q_i = \sum_{l=1}^{4} \hat{\alpha}^l_{i+1/2} \mathbf{R}^l_{1+1/2}$$

$\hat{\delta}^2_{i+1/2}$ and $\hat{\delta}^3_{i+1/2}$ are positive parameters which control the amount of anti-diffusion in the linear degenerate fields. For $\hat{\delta}^2_{i+1/2} = 0$ and $\hat{\delta}^3_{i+1/2} = 0$, we retain the Riemann solver (4.45). Out of several choices for the average state $\hat{\mathbf{w}}_{i+1/2}$ are possible, Einfeldt et al [41] chose,

$$\begin{aligned}
\hat{\rho}_{i+1/2} &= \sqrt{\rho_i \rho_{i+1/2}} \\
\hat{u}_{i+1/2} &= \frac{\sqrt{\rho_i} u_i + \sqrt{\rho_{i+1}} u_{i+1}}{\sqrt{\rho_i} + \sqrt{\rho_{i+1}}} \\
\hat{v}_{i+1/2} &= \frac{\sqrt{\rho_i} v_i + \sqrt{\rho_{i+1}} v_{i+1}}{\sqrt{\rho_i} + \sqrt{\rho_{i+1}}} \\
\hat{H}_{i+1/2} &= \frac{\sqrt{\rho_i} H_i + \sqrt{\rho_{i+1}} H_{i+1}}{\sqrt{\rho_i} + \sqrt{\rho_{i+1}}} \\
\hat{c}_{i+1/2} &= (\gamma - 1) \left\{ \hat{H}_{i+1/2} - \frac{1}{2} (\hat{u}^2_{i+1/2} + \hat{v}^2_{i+1/2}) \right\}
\end{aligned}$$

Along with new HLLEM scheme (4.50), Einfeldt et al [41] proved that Godunov's and the HLLE-scheme have this property, which are based on a local linearized Riemann solver (e.g.,Roe's scheme) may lead to an unphysical negative density or internal energy during the computational process. The interpretation of Roe's scheme as an HLLE-scheme with the appropriate anti-diffusion term in the linear degenerate field leads to an improved scheme, which does not require an artificial entropy fix and does not suffer from the instabilities described in the literature [41] where it was claimed that certain Riemann problems are not linearizable.

4.2.3.4 HLLE+ Flux Scheme

In 2001, an improved HLLE+ flux scheme, based on HLLEM [41], was proposed by Park and Kwon [23] which has been used in the present computations. Although Einfeldt improved [41] the original HLLE scheme by defining a more stable definition of average state and keeping HLLEM scheme positively conservative, it suffered some serious issues such as shock instability in multi dimensions and the nonexistence of strong receding flows as reported by

Liou [49]. It was also found that the HLLEM is less accurate than Roe's method, though it recovers the information of a contact discontinuity [50].

Through a linear perturbation analysis on the odd-even decoupling problem, Park and Kwon devised the necessary conditions for designing a shock stable scheme and presented curing methods for the HLLEM method. As a result, a new improved HLLE (HLLE+) scheme was proposed and analyzed on its dissipation mechanism. It was shown that this new flux scheme can accurately predict the surface heating rates without grid dependency. An improved HLLE scheme, denoted by HLLE-h, is proposed through the discrete analysis. It eliminates the erroneous dissipation of HLLEM scheme and adopts a switching function based on the second order derivative of pressure in order to reduce the dependency of grid and flow conditions.

The numerical flux $F(\mathbf{w}_l, \mathbf{w}_r)$ of a class of Godunov type (GT) schemes [43] is defined as follows:

$$\mathbf{F}^{GT}(\mathbf{w}_l, \mathbf{w}_r) = \frac{b^+\mathbf{F}(\mathbf{w_l}) - b^-\mathbf{F}(\mathbf{w_r})}{b^+ - b^-} + \frac{b^+b^-}{b^+ - b^-}\{(\mathbf{w}_r - \mathbf{w}_l) - \sum_p \delta^p \alpha^p \mathbf{R}^p\} \tag{4.51}$$

with b^+ and b^- defined to be:

$b^+ = max\ \{b^r, 0.0\},\ b^- = max\ \{b^l, 0.0\}$

$$b^r = max\ \{\lambda_2, \mathrm{C}_r^+\}$$

$$b^l = max\ \{\lambda_3, \mathrm{C}_l^-\}$$

where the parameters, C^+ and C^- are the newly introduced signal velocities in order to unify the representation of Godunov-type schemes.

The coefficients, α^p, are associated with the linear degenerated and nonlinear fields for characteristic waves which expand $\mathbf{w}_r - \mathbf{w}_l$ in terms of the right eigenvectors $\mathbf{R}^p$.

$$\alpha^p = \mathbf{L}^p(\mathbf{w}_r - \mathbf{w}_l)$$

where $\mathbf{L}^p$ is the left eigenvectors of the flux Jacobian.

The anti-diffusion coefficients δ^p in Eq.(4.51) are defined such that they take out excess dissipation in the linear degenerated fields, subjected to the stability of the scheme to be preserved:

$$\delta^1 = \frac{\hat{a}}{|\bar{u}| + \hat{a}}, \quad \delta^{2,3} = 0.0$$

where the value $\bar{u}$ is an approximation for the speed of the contact discontinuity [41].

According to the definition of C^+, C^-, and $\bar{u}$, different dissipation mechanisms can be generated. HLLE scheme [43]:

$$\begin{aligned} &C^+ = u_r + a_r, \quad C^- = u_l - a_l, \\ &|\bar{u}| = \infty \ so\ that\ \delta^1 = 0.0 \end{aligned} \tag{4.52}$$

HLLEM scheme [41]:

$$\begin{aligned} &C^+ = u_r + a_r, \quad C^- = u_l - a_l, \\ &|\bar{u}| = \left| \frac{b^r + b^l}{2} \right| \end{aligned} \tag{4.53}$$

HLLE+ scheme [23]:

$$\begin{aligned} &C^+ = u_r + a_r, \quad C^- = u_l - a_l, \\ &|\bar{u}| = \beta|\hat{u}| + (1.0 - \beta)\hat{a} \\ &\beta = \begin{cases} 1.0, & if\ k_p \leq 0.1 \\ 0.0, & otherwise \end{cases} \end{aligned} \tag{4.54}$$

A switching parameter β is activated in vicinity of the shock instabilities, where k_p adjusts the magnitude of the dissipation as a shock indicator which is defined by [51]:

$$k_p = \frac{1}{2}\left(\left| \frac{P_{i+1,j} - 2P_{i,j} + P_{i-1,j}}{P_{i+1,j} + 2P_{i,j} + P_{i-1,j}} \right| + \left| \frac{P_{i,j+1} - 2P_{i,j} + P_{i,j-1}}{P_{i,j+1} + 2P_{i,j} + P_{i,j-1}} \right| \right)$$

Quirk [25] proposed a switching method based on the pressure gradient. Quirk used the HLLE scheme as an alternate method when the base is the Roe scheme. The main difference of the HLLE+ scheme, compared with Quirk's method, is the switching based on Lin's [51] second derivative of pressure. The second derivative-based parameter is claimed to be more robust than that based on the first order one according to numerical experiments by Kwon and Park [23].

Consider now the semi-discrete form of Euler equations (4.28). The convective flux $F_{i+1/2}$ is given by,

$$F_{i+1/2} = \frac{b^+_{i+1/2}\mathbf{F}(\mathbf{w^l_{i+1/2}}) - b^-_{i+1/2}\mathbf{F}(\mathbf{w^r_{i+1/2}})}{b^+_{i+1/2} - b^-_{i+1/2}} + \frac{b^+_{i+1/2}b^-_{i+1/2}}{b^+_{i+1/2} - b^-_{i+1/2}}\{(\mathbf{w}^r_{i+1/2} - \mathbf{w}^l_{i+1/2}) - \sum_p \delta^p \alpha^p \mathbf{R}^p\} \tag{4.55}$$

By computing two dimensional hypersonic viscous flow past a blunt cylinder, it was shown that new switching mechanism does not affect the convergence speed of this modified Godunov-type (HLL) flux scheme.

4.3 Spatial Discretization and Reconstruction

To evaluate the surface integral in Equation (4.3), we need to know the primitive variables at the cell faces so that we can evaluate the fluxes. Reconstruction provides this link between the cell averages (what's stored) and the cell-face data (what's needed). The reconstruction process simply converts known cell-average data (see Equation (4.5)) into a point-wise field of data. The reconstruction is evaluated at a cell face and the flux determined. GASPex allows the user to employ characteristic-based (upwind) flux functions for computing the flux and these functions require two fluid dynamic states at each cell face - the so-called left and right states. The accuracy of reconstructing the primitive-variable field at the cell faces determines the spatial accuracy of the solution [46]. A one-parameter family of interpolated values for the left state at the $i + 1/2$ face and right state at the $i - 1/2$ face can be represented as

$$\begin{aligned} \mathbf{q}^l_{i+1/2} &= \mathbf{q}_i + \frac{\phi}{4}[(1-\kappa)\nabla\mathbf{q}_i + (1+\kappa)\Delta\mathbf{q}_i] \\ \mathbf{q}^r_{i-1/2} &= \mathbf{q}_i - \frac{\phi}{4}[(1+\kappa)\nabla\mathbf{q}_i + (1-\kappa)\Delta\mathbf{q}_i] \end{aligned} \tag{4.56}$$

where the value for κ determines the spatial accuracy of the reconstruction and ϕ is either $\phi = 0$ for first-order accuracy, or $\phi = 1$ for high-order accuracy. This variable extrapolation method is called the Monotonic Upstream-centered Scheme for Conservation Laws (MUSCL). The forward and backward difference operators are

$$\Delta\mathbf{q}_i = \mathbf{q}_{i+1} - \mathbf{q}_i$$

$$\nabla\mathbf{q}_i = \mathbf{q}_i - \mathbf{q}_{i-1}$$

for all interior cells and ghost-cell boundaries.

This all works great for interior cells and ghost-cell boundaries, but how do solid-wall boundaries affect the local reconstruction? Obtaining the inviscid flux along a solid surface does not require a reconstruction because the primitive variables at the boundary face are known from the tangency boundary condition (for inviscid flows). The flux is evaluated with the data provided at the wall. For the first interior face, the MUSCL formulation (i.e., Eqn. (4.56)) is altered to account for the position in space of the boundary data. For example, if a solid surface exists at an *i0* boundary, the backward gradient is doubled (i.e.,

$\nabla \mathbf{q} \rightarrow 2\nabla \mathbf{q} = 2(\mathbf{q}_2 - \mathbf{q}_1)$) to account for the closer spacing between data points. A similar correction is applied for the forward gradient for an *idim* solid wall.

In the GASPex GUI, a first-order reconstruction (i.e., $\phi = 0$) is assumed if κ is outside the range of $\kappa \in [-1, +1]$. If the user inputs a high-order value of κ in the marching direction, then GASPex assumes $\kappa = -1$. To assist the user, the value of κ is set according to the spatial accuracy selected in the inviscid tab of the GUI. For global flow fields, the common choices for κ are [20]:

$\kappa = -1$	Second-order, fully upwind scheme. The linear reconstructions slope equals the fully upwind gradient, $q_i - q_{i-1}$.
$\kappa = 0$	Second-order, Fromms scheme. The linear reconstructions slope equals the symmetric gradient, $q_{i+1} - q_{i-1}$.
$\kappa = 1/3$	Third-order, quadratic reconstruction which conserves the cell average of all three cells in the stencil: $q_{i-1},\ q_i,\ q_{i+1}$.
$\kappa = +1$	Central differencing. The linear reconstructions slope equals the downwind gradient, $q_{i+1} - q_i$.

For the present computations, third-order upwind biased, quadratic reconstruction ($\kappa = 1/3$) which is no less stable than second order upwind biased reconstruction ($\kappa = -1$) has been utilized.

4.4 Limiters

The unlimited reconstructions in Eqn. (4.56) work well for smooth regions of the flow; however, in regions with large gradients such as shocks, the higher-order correction term must be reduced to maintain stability and eliminate numerical oscillations in the solution. This process is called limiting because the reconstruction at the cell face should be within the limits of the adjacent cell averages. For example, if $q_{i+1} > q_i$, then the interface value, $q_{i+1} = 2$, should be within the two adjacent limits (i.e., $q_i < q_{i+1} = 2 < q_{i+1}$). Limiters are designed by altering the high-order term to yield interface reconstructions which are within the bounds of the adjacent cell averages. Using a linear reconstruction on a uniform mesh, we can write the interface primitive variables as

$$\mathbf{q}^{l}_{i+1/2} = \mathbf{q}_i + \frac{1}{2}\Big(\frac{\partial \mathbf{q}}{\partial x}\Big)\Delta x \equiv \mathbf{q}_i + \frac{1}{2}\delta\mathbf{q}$$
$$\mathbf{q}^{r}_{i-1/2} = \mathbf{q}_i - \frac{1}{2}\Big(\frac{\partial \mathbf{q}}{\partial x}\Big)\Delta x \equiv \mathbf{q}_i - \frac{1}{2}\delta\mathbf{q}$$

Comparing this Taylor series with the expressions given in Eqn. (4.56), we can identify $\delta\mathbf{q}$ as

$$\delta\mathbf{q} = \frac{1}{2}[(1-\kappa)\nabla\mathbf{q}_i + (1+\kappa)\Delta\mathbf{q}_i]$$

In GASPex limiting is applied in two different ways: limiting of the primitive variables and limiting performed in the marching direction. The limiting parameter in the GUI controls the limiting performed in each of the coordinate directions. Primitive-variable limiting means that the particular limiter model (e.g., min-mod) is applied to the forward and backward gradients of the primitive variables. These limited gradients are then applied in Eqn. (4.56) to obtain the reconstructed values of the left and right states. The exact form of the limited equation depends on the model selected.

There are many limiters available in GASPex such as Van Albada's limiter, Min-Mod limiter, Spekreijse limiter, Roes SuperBee limiter etc. For current computations, the *Min-Mod limiter* which has been found to be robust and accurate for many applications in the past has been implemented.

4.4.1 The Minimum Modulus (Min-Mod) Limiter

The lowest boundary of the total variation diminishing (TVD) region is realized when the limiter incorporates the Minimum-Modulus (Min-Mod) function [52]. The Min-Mod function chooses the smaller of the two gradients (forward and backward) by magnitude if they have the same sign and zero otherwise. The function can be written as

$$\text{minmod}(x,y) = \begin{cases} x, & |x| < |y| \text{ and } xy > 0 \\ y, & |y| < |x| \text{ and } xy > 0 \\ 0, & xy < 0 \end{cases}$$

This limiter resolves contact discontinuities poorly and can cause limit cycles in the convergence process. Nonetheless, the Min-Mod limiter is a popular limiter by the user

community. The min-mod filtering function with Fromms high-order scheme is

$$R(\theta) = \begin{cases} \dfrac{2\theta}{\theta+1}, & 0 \le \theta \le 1 \\ \dfrac{2}{\theta+1}, & \theta \ge 1 \end{cases}$$

Notice that the filtering function chooses the difference with the smaller modulus. Choosing either $\delta\mathbf{q} = \Delta\mathbf{q}_i$ or $\delta\mathbf{q} = \nabla\mathbf{q}_i$ for all θ would eventually yield an interpolation that was outside the bounds of the TVD region. The min-mod filtering function given here generates either second-order upwind or central-difference interpolation beginning from Fromm's scheme.

4.5 Viscous Model Formulations

Since the dimension of hollow cylinder in the direction of the flow is very large, the boundary layer is fully turbulent before it approaches the flare. Hence, turbulent viscous (diffusive) flux has been chosen. For viscous problems (either laminar or turbulent flow), one must select an appropriate viscosity model, conductivity model, and diffusivity model. For our computations, Sutherland's viscosity model, Sutherland's conductivity model and constant Schmidt number diffusivity model have been chosen.

Sutherland's Viscosity Model is the extension of Sutherland's relation for a perfect gas to a generic component. Using the idealized intermolecular-force potential of Sutherland [53] where molecules are assumed to be weakly attracted when not in contact, the species viscosity and conductivity can be written as

$$\mu_i = \mu_0 \Big(\frac{T}{T_0}\Big)^{3/2} \frac{T_0 + S}{T + S}, \qquad k_i = k_0 \Big(\frac{T}{T_0}\Big)^{3/2} \frac{T_0 + S}{T + S}$$

The coefficients μ_0, k_0 T_0 and S depend upon the specie.

The simplest modeling of the diffusivity is obtained by assuming a constant Schmidt number and knowing the species viscosity. When modeling the diffusivity in this way, all of the species diffusivities equal one global constant denoted D_{12}. Using the definition of the Schmidt number, the binary diffusion coefficient is determined as follows

$$D_i = D_{12} = \frac{\mu}{\rho\ Sc}, \qquad \text{For turbulent flow, } D_i = D_{12} = \frac{\mu}{\rho\ Sc} + \frac{\mu_t}{\rho\ Sc_t}$$

where Sc is the Schmidt number.

The viscosity is determine using Sutherland's law as described above. Schetz recommends a turbulent Schmidt number of $0.5 < Sc_t < 0.7$ for radial and planar injection of air into air [54].

For consistency, the accuracy of the wall-gradient has been set to second order accurate. The viscous derivatives are then calculated with a one-sided, second-order accurate difference formula at a physical boundary. As discussed previously, $k - \omega$ Wilcox (2006) turbulence model with no limiting, turbulent Prandtl number equal to 0.9 and turbulent Schmidt number equal to 0.5 has been used.

4.6 Grid Generation

In computational fluid dynamics, the Plot3D file format is a standard file format used for storing grid and results data. Plot3D was created at the NASA Ames Research Center in 1982 by Pieter Buning and remains an often used file format. It can only store a structured grid. The structured grid allows random access, that is by knowing the block number, i location, j location, and k location, any grid point value or result value may be extracted. Additionally, given the location of any value, the block number, i location, j location, and k location may be determined. This makes it simple to iterate through a series of volumetric elements and calculate all required properties for the purpose of a CFD analysis.

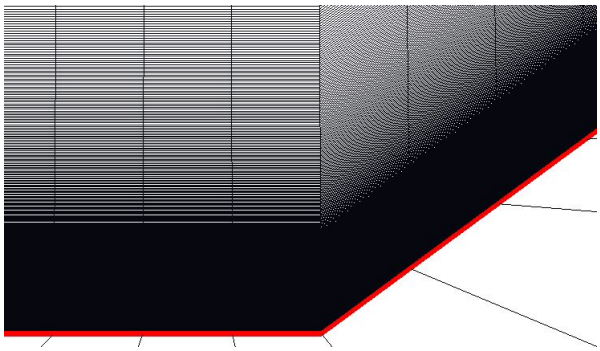

Figure 4.9: Grid Clustering Near Wall (Zoomed Down at Hollow Cylinder-Flare Junction)

Over the period of this computational study, C++ codes have been written by the

author to create a series of 10 grids with increasing resolution in each grid iteration in order to reach an optimum grid resolution. Final computations have been carried out on a grid with resolution of 2764 x 3113. In Plot3D grid format, x, y, and z (if 3 dimensional grid) coordinates have to be written in a particular order. In the present case we are dealing with a 2D grid which is converted into a 2D axisymmetric grid by GASPex commercial software.

The basic idea is to provide x and y coordinates for every node in the grid. In the first few lines of the grid file, we list the number of zones in the grid followed by the resolution of each zone. Then, x coordinates for every y coordinate of first zone is written. After that, y coordinates for every x coordinate of the first zone are written. It should be noted that in writing both x and y coordinates, we start at the first y node and write x or y coordinates for every x node and then we move to the next y node. This concludes the definition of grid in the irst zone. For multiple zones, this procedure is repeated for each zone. To better illustrate the procedure, a sample grid has been shown in the Figure 4.11 and a Plot3D grid file has been written alongside.

An oblique shock is generated due to boundary layer displacement at the leading edge. We can calculate Mach angle from the inlet conditions as following

$$\mu = \sin^{-1}\left(\frac{1}{M_\infty}\right), \quad H = L \cdot \tan(\mu) \tag{4.57}$$

H is the height of the flow domain until where the oblique shock wave will spread at the end of the test model. L is the length of the test model.

In order to resolve the boundary layer and its interaction with shock wave, the first cell height should be very fine and should slowly increase across the boundary layer. The first cell aspect ratio ($\Delta x/\Delta y$) is 1145234 which slowly decreases to 1.42 with growth rate of 1.008 in y direction. Here, $\Delta x = 1.15 \times 10^{-3} m$ (constant) and $\Delta y_{wall} = 10^{-9} m$. The aspect ratio is constant after the cell height equals the boundary layer thickness at the end of the hollow cylinder. The boundary layer thickness has been estimated by an empirical formula for turbulent boundary layer thickness, $\delta_t = (0.37x)/(Re_x^{1/5})$.

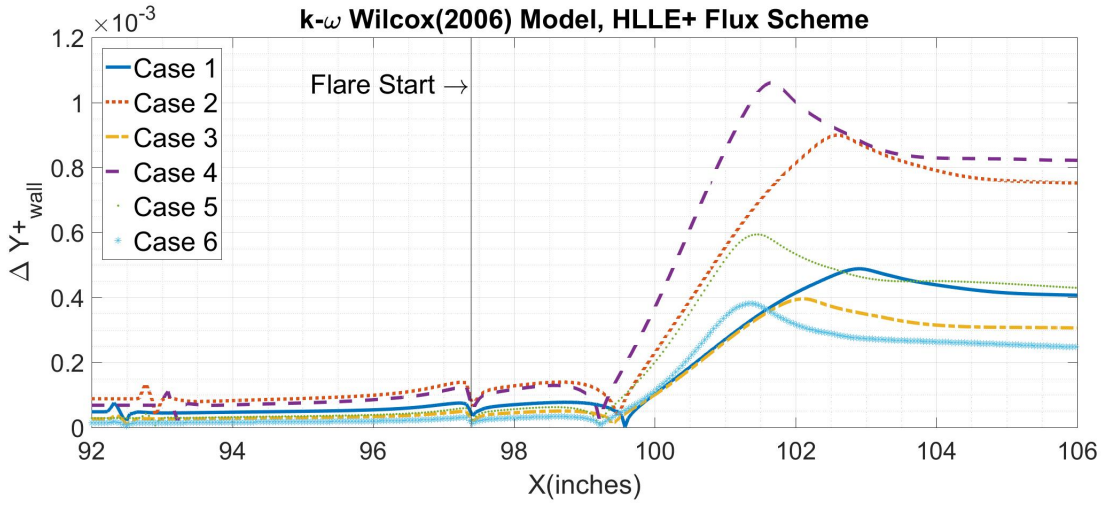

Figure 4.10: $\Delta Y+_{wall}$ for All Cases

Sample Plot3D Grid File

1 ←*(Number of zones)*

3 3 ←*(Zone resolution)*

0 1 2 ←*(x coords at 1^{st} y node(0))*

0 1 2 ←*(x coords at 2^{nd} y node(0.25))*

0 1 2 ←*(x coords at 3^{rd} y node(0.5))*

0 0 0 ←*(y coords at 1^{st} y node(0))*

0.25 0.25 0.25 ←*(y coords at 2^{nd} y node(0.25))*

0.5 0.5 0.5 ←*(y coords at 3^{rd} y node(0.5))*

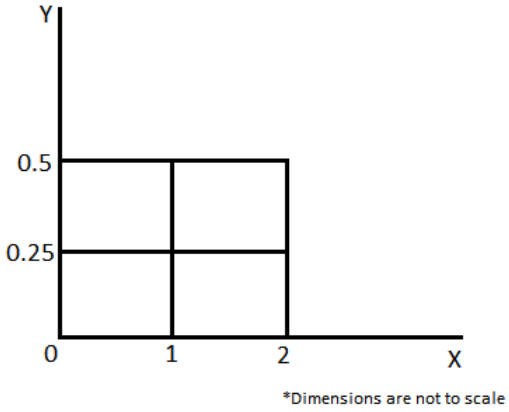

Figure 4.11: Sample Grid

4.7 Solver Setup

Aerosoft's General Aerodynamic Simulation Program (GASPex) has been utilized to simulate the experimental flow conditions around a large hollow cylinder flare configuration. There are many input parameters in the solver setup which are left for inputs from the user. We will go through each set of parameters.

4.7.1 Grid Import

The first step is to import a grid which was generated in Plot3D (.p3d) ASCII format using C++. Grid generation techniques have been described in detail in the previous section. As shown in the Figure 4.12, there are options to select the file format, grid format, grid system and grid units. GASPex allows to select between English and Metric units. The current grid is a multi-zone grid in metric units written in ASCII file format and double precision has been selected for accuracy. For a 2-D axisymmetric grid system, GASPex can take the 2-D grid from input grid file and rotate it about the x-axis $by \pi/80$ and $-\pi/80$ ($+2.25$ degrees and -2.25 degrees). The grid has been generated by keeping in mind the fact that GASPex assumes the 2-D grid is in the xy plane and that the x axis is the axis of symmetry. This way we don't have to simulate the flow for whole 3-D geometry and can still predict the flow features for 3-D flow while using 2-D axi-symmetric option due to its axisymmetry. This is a well known practice in CFD applications.

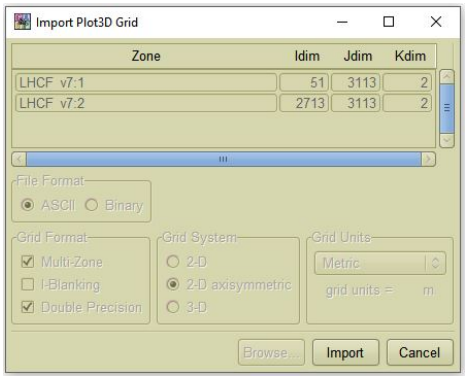

Figure 4.12: Grid Import Tab

4.7.2 Zonal Boundaries

Since we are using multi-zone grid system, we need to connect zonal boundaries between two zones in order to pass the flow information across the zonal boundaries. We can compute

the point-to-point zonal boundaries in GASPex with an internal algorithm that will search the grid for zonal boundaries. The algorithm searches for common nodes to within some tolerance. This relative tolerance is specified by the user and may need to be adjusted in order to get the algorithm to work correctly for a given set of grids. For our problem, the value of this relative tolerance is 0.0001. In order to determine if two surface faces form a point-to-point mapping, the four grid points of each are compared to see if they lie on top of each other. The relative tolerance is the physical distance between two points being checked normalized by the cell size (longest edge length). Occasionally this can be problematic with a highly stretched grid where the (aspect ratio)*(relative tolerance) > 1 [20]. Although, this product number ranges from 114.5 to 0.00014 in our case, this algorithm has worked out fine for connecting zonal boundaries.

4.7.3 Grid Sequencing

Grid sequencing is a powerful tool that can help reduce the required CPU time needed to obtain the final solution to a problem. The finest grid has a resolution of 2764 x 3113. For the original grid (i.e., the finest grid), the values for the ILev, JLev, and KLev are all set to 1, meaning that every grid line is kept. For the next sequence level, *medium-2*, the values for the ILev and JLev are changed to 2, meaning every other grid line is retained. This way, resolution of this new sequence is half of that of fine sequence in both X and Y directions. Thus, as shown in Figure 4.13, the total number of cells in medium-2 sequence will be $1/4^{th}$ of that of the fine (original) sequence, which is 8.6 million cells for the fine sequence. In total, four sequence levels have been generated including the original grid. Other two sequence levels have next logical Lev value for both I and J direction which is 4 for *medium-1* sequence and 8 for *coarse* sequence.

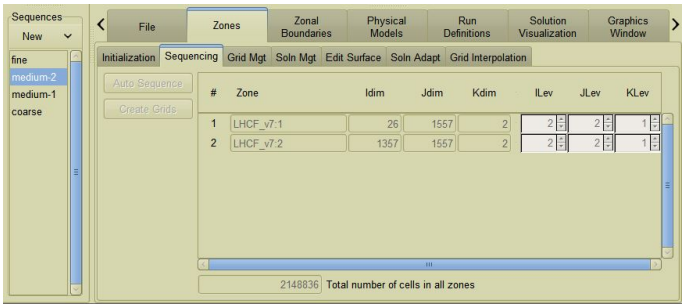

Figure 4.13: Grid Sequencing Tab

4.7.4 Run Definitions

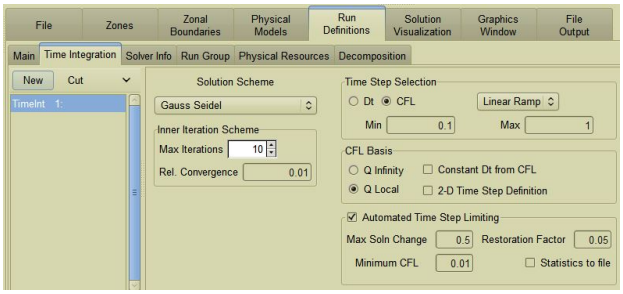

Figure 4.14: Time Integration Tab

As shown in Figure 4.14, the algorithm implemented for solving an iterative technique for solving a linear system is a symmetric *Gauss-Seidel* solver which does a forward and backward sweep each iteration. The Gauss-Seidel solver alone is not a very effective time-integration strategy. However, this method takes far less CPU time per iteration than other implicit schemes, and when combined with an inner-iteration strategy, the convergence rate drastically improves. There are two parameters for doing inner iterations. The first controls the maximum number of inner iterations. This is the number of inner cycles to be performed unless a tolerance is satisfied. The tolerance is relative to the first inner cycle and is specified in the Rel. Convergence type-in box.

An efficient method of advancing the solution in time is to use a uniform Courant number for each cell (i.e., a non-dimensional time step). In this case, each cell has a unique time step based upon the CFL number, a reference velocity, and the cell size. This option corresponds to selecting the CFL radio button. With the linear ramp option, the CFL number will increase over the course of a run in which the value varies linearly with the cycle number between the Min and Max values.

CFL basis changes how a reference velocity is calculated for cell. With a CFL, the time step for a gas dynamic system is calculated using [20]

$$\Delta t = \frac{\lambda \Delta_L}{c}$$

where λ is the CFL or Courant number, Δ_L is a characteristic length of the cell, and c is the fastest characteristic speed. Using the *Q Infinity* option corresponds to calculating the characteristic speed with free-stream quantities, while *Q Local* calculates the characteristic speed using the local cell quantities. High-speed viscous flows converge well by first using

local time stepping and then switching to freestream time stepping. Often the local time stepping will converge a viscous region and the primary shock features, but the pre and post-shock time steps are orders of magnitude different causing the residual to plateau. Switching to the freestream characteristic speed in the CFL definition equalizes the time steps around the shock and aids convergence.

The *Automated Time Step Limiting* option is intended to help improve robustness. When using a CFL, this option will adjust the time step for an individual cell. The time step will be lowered if the solution changes by more than a prescribed amount (specified by Max Solution Change). For example, a Max Solution Change value of 0.5 means that the time step will be lowered if the solution changes by more than 50%. The time step limiting is applied on a cell by cell basis. If the time step has been lowered for a cell, yet the solution is no longer changing by more than the prescribed limit, the time step will be raised according to the value of Restoration Factor. In Figure 4.14, the value 0.05 corresponds to a 5% increase in time step each cycle.

In *solver info* tab, the turbulence system of equations has been defined as *uncoupled*. Uncoupling the turbulence equations offers the potential to lower computational time and memory necessary for the solution of the block-matrix system. When uncoupled turbulence is selected, the fluid dynamic system update is followed by a non-linear residual update for the turbulence system. In addition, individual residual information of continuity, momentum, energy and turbulence has been monitored at the end of each run definition

Lastly, the number of processors and memory per processor is also defined for each run definition. Along with that, decomposition in performed separately, which is the process of dividing a zone up into multiple partitions. Prior to decomposition, a zone consists of a single partition. Zone decomposition is done for three reasons [20]. The first reason is to run the problem in parallel efficiently. There must be, at a minimum, the same number of zone partitions as processors. Each processor is assigned at least one zone partition to compute. To maximize the work load on all the processors, the load size assigned to each processor should be roughly equal. This can be accomplished using zone decomposition. The second reason to break zones up into smaller sizes is to decrease the memory use. Running more zones with explicit passing of partition boundary information will reduce

the required CPU memory. The final reason is also to reduce memory, but in this case the reduction of local memory is desired for the purpose of improving CPU performance on cache-based computers. *Load Balancing Automated Decomposition* has been utilized to setup the decomposition to give proper load balancing for parallel runs.

4.8 Boundary Conditions

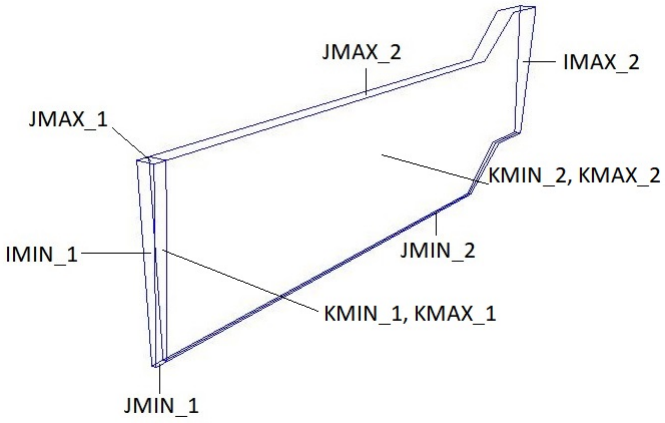

Figure 4.15: Boundary Conditions

As shown in the Figure 4.15, there is an initialization zone (Zone 1) with 50 x 3113 cells before the beginning of the hollow cylinder flare in the grid in order to develop the flow before entering the actual flow field. Boundary conditions on respective surfaces are given as shown in the Table 4.1.

If the fixed-temperature, no-slip wall is specified, the wall temperature, T_1, is set to the user specified temperature. The pressure, non-equilibrium vibrational energy and mixture gas constant are all extrapolated from the interior. The density is calculated using the equation of state, $p_1 = \rho_1 \widetilde{R}_1 T_1$. The mass fractions at the wall are assumed equal to those of the first interior cell. The velocity components are set to zero for no slip. The turbulence kinetic energy is set to zero and the dissipation rate at the wall depends upon the turbulence model in use. In summary the fixed-temperature, no-slip boundary condition specifies that

Zone	Surface ID	Boundary Condition
Zone 1	IMIN_1	Inlet (free-stream conditions)
Zone 1	JMIN_1, JMAX_1	Symmetry Plane
Zone 1	KMIN_1	Positive Axisymmetric Wall
Zone 1	KMAX_1	Negative Axisymmetric Wall
Zone 2	JMIN_2	Fixed temperature, No-slip Wall ($T = T_{wall}$)
Zone 2	IMAX_2, JMAX_2	Outlet (first order extrapolation)
Zone 2	KMIN_2	Positive Axisymmetric Wall
Zone 2	KMAX_2	Negative Axisymmetric Wall

Table 4.1: Boundary Conditons

the primitive variables are determined as follows:

$$
\begin{aligned}
&\text{Temperature at boundary,} && T_1 = T_w,\\
&\text{Velocity components,} && u_1 = v_1 = w_1 = 0,\\
&\text{Non-equilibrium vibrational energy,} && (e_{ni})_1 = (e_{ni})_2,\\
&\text{Wall pressure,} && p_1 = p_2,\\
&\text{Mixture gas constant,} && \widetilde{R}_1 = \widetilde{R}_2,\\
&\text{Mixture density,} && \rho_1 = \frac{p_1}{\widetilde{R}_1 T_1},\\
&\text{Mass fraction density,} && (\rho_i)_1 = \left(\frac{\rho_i}{\rho}\right)_2 \rho_1.
\end{aligned}
$$

Across symmetry planes, the primitive variables reflect except that the sign of one velocity component reverses. Which component changes depends on whether the symmetry plane lies at a constant x, y or z location (i.e., a yz, xz or xy symmetry plane). For example, if the symmetry plane lies at a constant x location (i.e., a yz symmetry plane), then the symmetry boundary condition fills the ghost cells as:

Mass fraction density,	$(\rho_i)_1 = (\rho_1)_2,$
Velocity components,	$u_1 = -u_2,\ v_1 = v_2,\ w_1 = w_2,$
Non-equilibrium vibrational energy,	$(e_{ni})_1 = (e_{ni})_2,$
Pressure at boundary,	$p_1 = p_2,$
Turbulent kinetic energy,	$K_1 = K_2,$
Turbulent dissipation,	$\epsilon_1 = \epsilon_2$

In GASPex, the axisymmetric side-wall boundary condition applies under very strict conditions. First the flow must be two-dimensional and axi-symmetric. The flow must be in the xy plane and the angular displacement of the side walls must be exactly $\pi/80$ or $+/-2.25°$. This means that the acute angle in a cross-flow pie wedge must be exactly $4.5°$. When these conditions apply, the interior velocity vector is rotated about the singular axis to the boundary cell. This boundary condition is automatically given to axisymmetric wall when you import a 2D grid file with 2D-axisymmetric flag turned on.

4.9 Run Definition

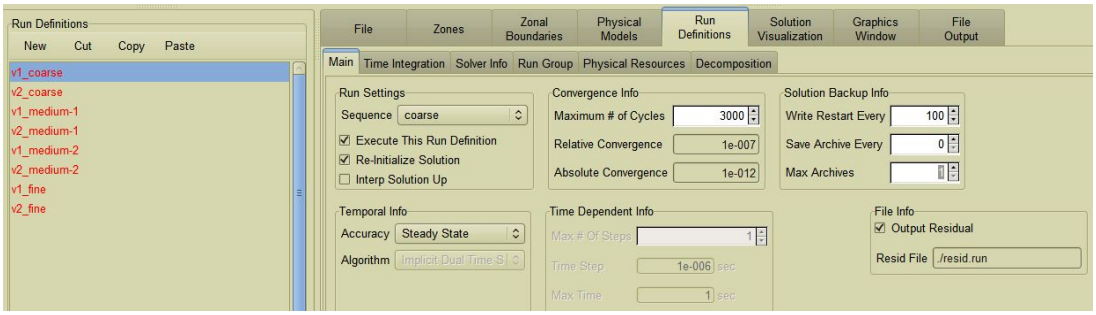

Figure 4.16: Run Definition Tab

The Run Definitions frame of GASPex solver is where the user defines how a problem is solved. Information such as which sequence and physical model to use, the time-integration scheme to use, and parallel settings are defined here. As shown in Figure 4.16, the Sequence option menu allows to select which sequence level to execute. Note that run definition for coarse has the re-initialize flag turned on. This enables us to initialize our computation

with inlet conditions as initial conditions in the flow domain. Once the computation for coarse sequence converges for *v2_coarse* run definition, solution will be interpolated to the next sequence level, *medium-1*, at the end of the run.

For each run definition, Output Residual option allows to extract information such as residuals, CPU time, parallel speed-up factor, load-balancing efficiency, percent CPU time for explicit and implicit communication, and the location of the largest residual. The residual is computed using the root-mean-square (RMS) value of the flux-balance residual over all the equations and cells. The residual value is one way to monitor solution convergence, as well as solution stability.

Run Definition	Sequence	Resolution	Max # Cycles	Rel. Conv. Criteria	CFL # Range	CFL Basis
v1_coarse	Coarse	346 x 390	5000	10^{-7}	0.1 to 1	Q Local
v2_coarse	Coarse	346 x 390	5000	10^{-7}	0.1 to 1	Q Infinity
v1_medium	Medium	705 x 779	10000	10^{-6}	0.1 to 10	Q Local
v2_medium	Medium	705 x 779	5000	10^{-6}	0.1 to 10	Q Infinity
v1_fine	Fine	1383 x 1557	10000	10^{-6}	0.1 to 25	Q Local
v2_fine	Fine	1383 x 1557	5000	10^{-6}	0.1 to 25	Q Infinity
v1_superfine	Superfine	2764 x 3113	10000	10^{-6}	0.1 to 50	Q Local
v2_superfine	Superfine	2764 x 3113	5000	10^{-6}	0.1 to 50	Q Infinity

Table 4.2: Run Definitions

A total of eight run definitions have been created, two run definitions for each sequence. In the Table 4.2, specific information about each run definition have been given. For a steady-state run, GASPex will execute the run definition until all the cycles have been completed or a residual tolerance has been met. Hence, we must provide maximum number of iterations and relative convergence criteria. For each run definition, the number of specified CPUs is 80 and amount of memory allocated per CPU is 2000 MB. Run definitions are executed in order as they appear in Figure 4.16.

Chapter 5

Results

For better visualisation, only last three grid sequences i.e., Coarse (705 x 779), Medium (1383 x 1557), Fine (2764 x 3113), out of total four grid sequences have been used in the following sections.

5.1 Grid Convergence Study

In this section, the grid convergence behavior of computation with HLLE+ flux scheme and k-ω Wilcox (2006) turbulence model is presented and discussed for each case. Similar behavior has been noticed for computations with other two flux schemes i.e., Roe and AUSM+.

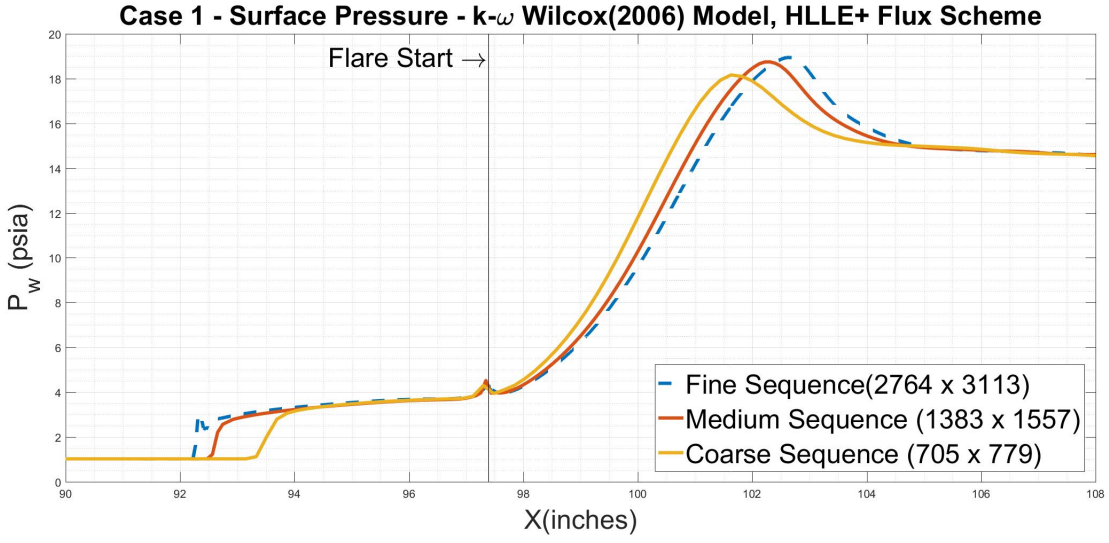

Figure 5.1: Case 1: Surface Pressure - Grid Convergence Study

As shown in Figures 5.1 and 5.2 for case 1, the boundary layer separation location, and re-attachment (peak surface pressure) location changes -0.29 inches and 0.34 inches

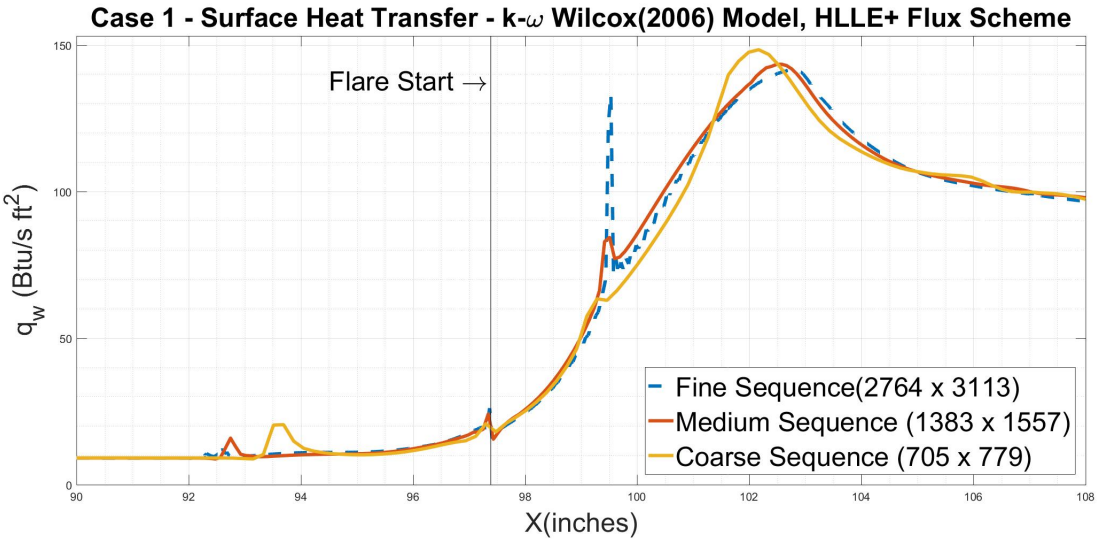

Figure 5.2: Case 1: Surface Heat Transfer - Grid Convergence Study

respectively between the medium and the fine grid sequences. A negative change in flow separation location means flow separates further upstream in the fine grid compared to the medium grid which results in re-attachment of flow at greater downstream distance, i.e., positive change in re-attachment location. Also, the change in the peak surface pressure value is 0.20 $psia$ (1.05%) and the change in the peak heat transfer value is -1.95 $Btu/s\ ft^2$ (-1.36%) between the two grid sequences. In Table 5.1, similar parameters, i.e., change in separation location, re-attachment location, peak surface pressure and peak surface heat transfer, are presented for all cases.

It should be noted that the medium grid sequence is interpolated to the fine grid sequence at the end of the medium run definition. After that, the solution has been computed on the fine grid sequence for another 15,000 iterations with the fine run definition which converges to 10^{-4} in normalised residuals.

Change Between Medium and Fine Grid Sequence				
Case	Separation Location $inch$ (%)	Re-attachment Location $inch$ (%)	Peak Surface Pressure $psia$ (%)	Peak Surface Heat Transfer $Btu/(s \cdot ft^2)$ (%)
1	-0.29 (-0.32%)	0.34 (0.33%)	0.20 (1.05%)	-1.95 (-1.36%)
2	-0.29 (-0.32%)	0.38 (0.38%)	0.46 (1.26%)	-4.00 (-1.60%)
3	-0.38 (-0.41%)	0.25 (0.24%)	0.30 (2.39%)	-0.64 (-0.40%)
4	-0.34 (-0.36%)	0.34 (0.33%)	0.90 (2.43%)	0.06 (0.02%)
5	-0.38 (-0.41%)	0.25 (0.25%)	0.41 (2.41%)	1.9 (0.57%)
6	-0.29 (-0.32%)	0.20 (0.20%)	0.26 (2.72%)	1.85 (0.77%)

Table 5.1: Grid Convergence Study

The change in peak heat transfer between medium and fine grid sequences is less than experimental uncertainty of 3%. Similarly, the change in peak surface pressure between medium and fine grid sequences is less than experimental uncertainty of 5%. Also, the percentage change in flow separation and re-attachment location between medium and fine grid sequences is less than 0.5% for all cases. Thus, it can concluded that good grid independence has been achieved for all the cases.

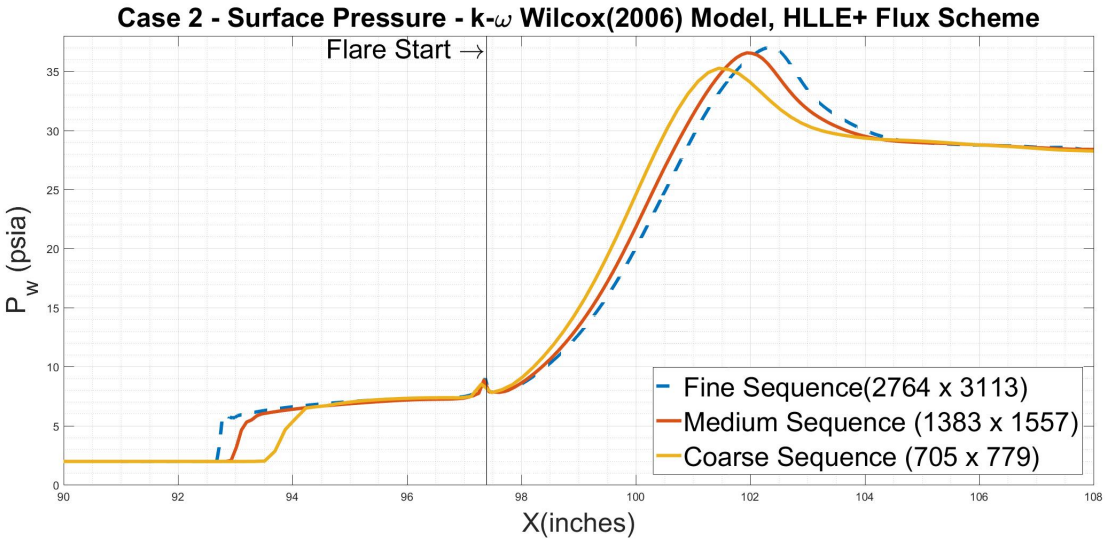

Figure 5.3: Case 2: Surface Pressure - Grid Convergence Study

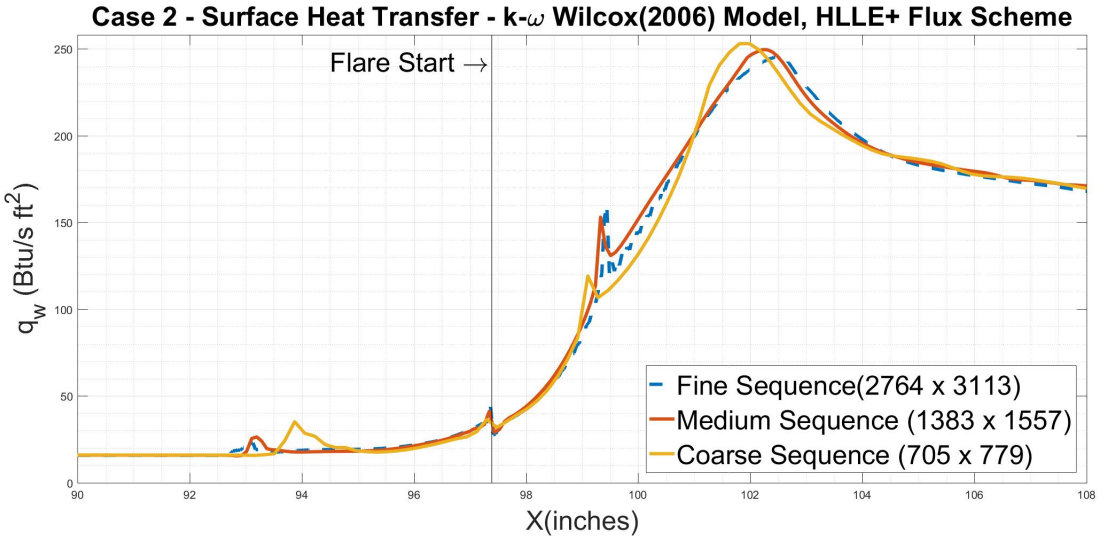

Figure 5.4: Case 2: Surface Heat Transfer - Grid Convergence Study

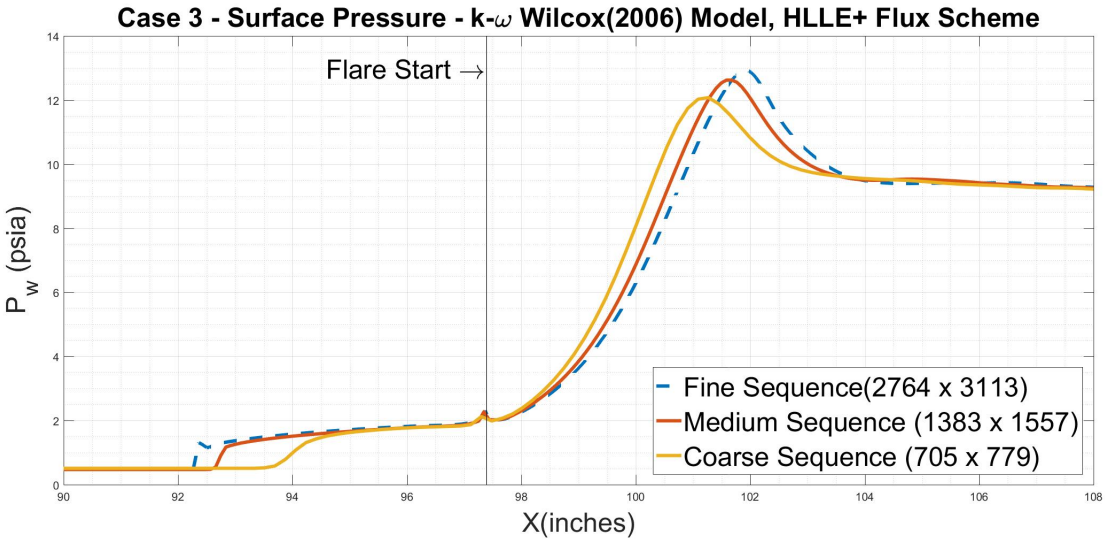

Figure 5.5: Case 3: Surface Pressure - Grid Convergence Study

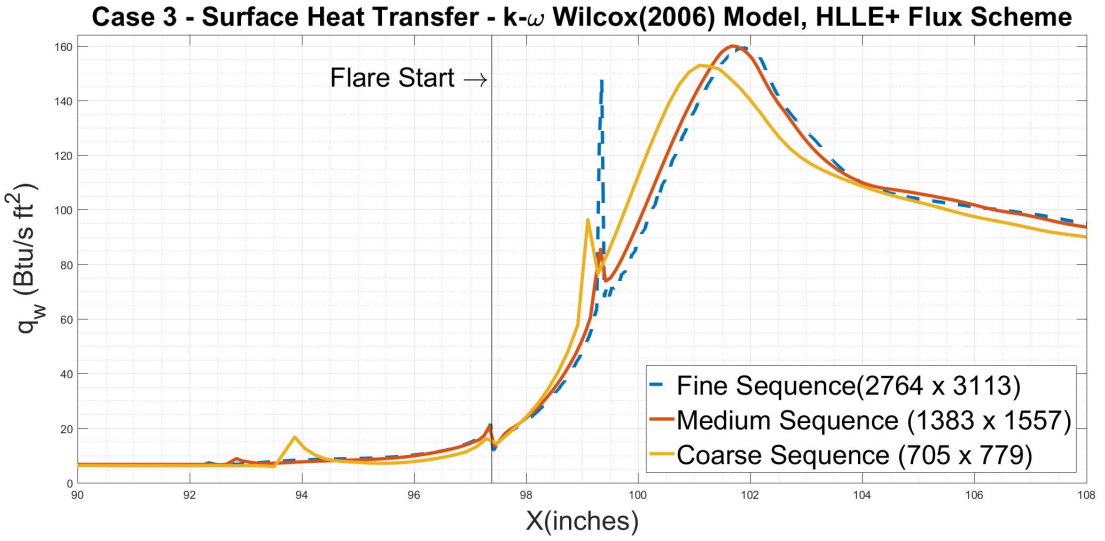

Figure 5.6: Case 3: Surface Heat Transfer - Grid Convergence Study

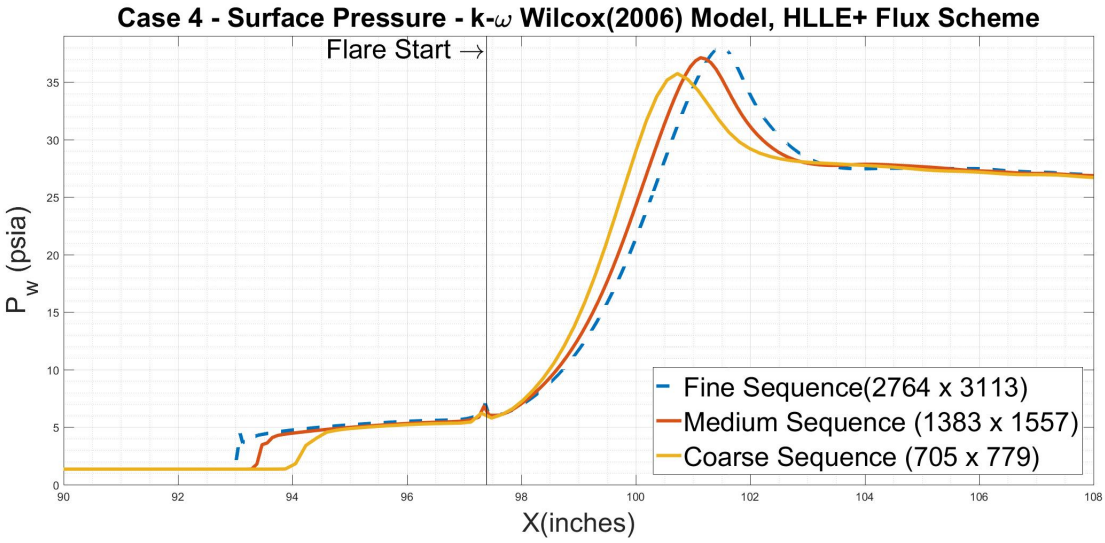

Figure 5.7: Case 4: Surface Pressure - Grid Convergence Study

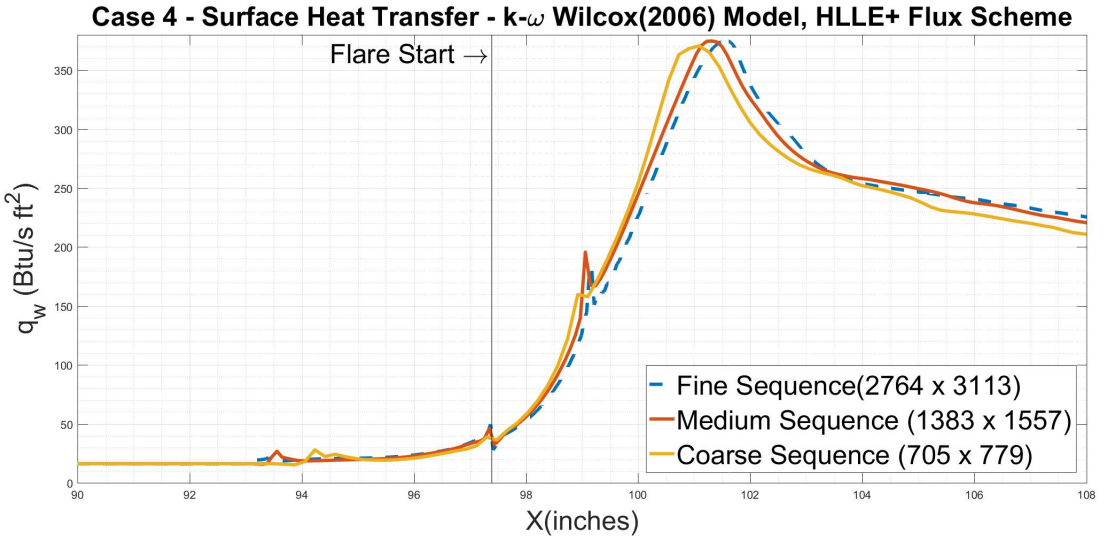

Figure 5.8: Case 4: Surface Heat Transfer - Grid Convergence Study

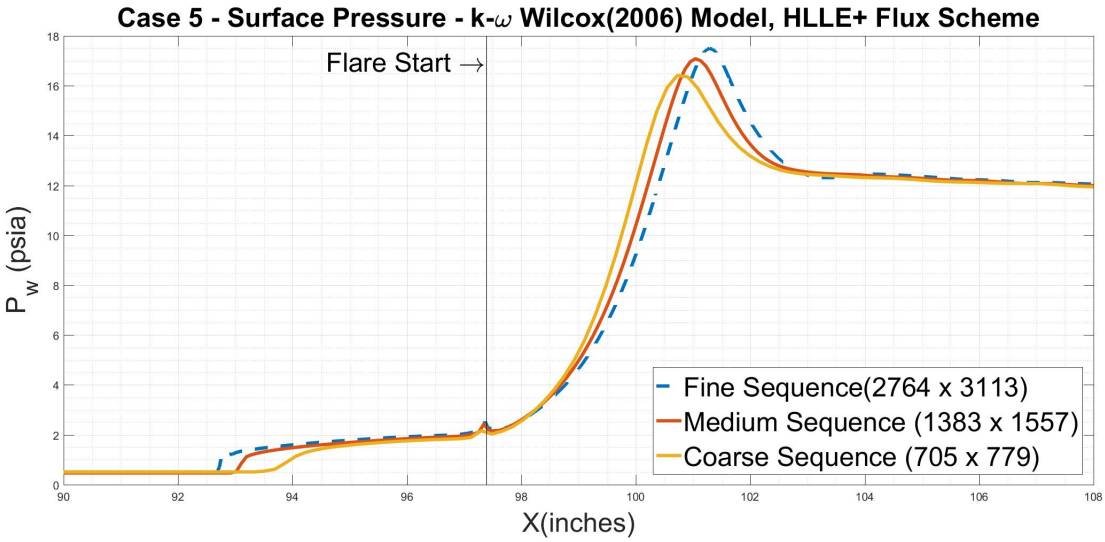

Figure 5.9: Case 5: Surface Pressure - Grid Convergence Study

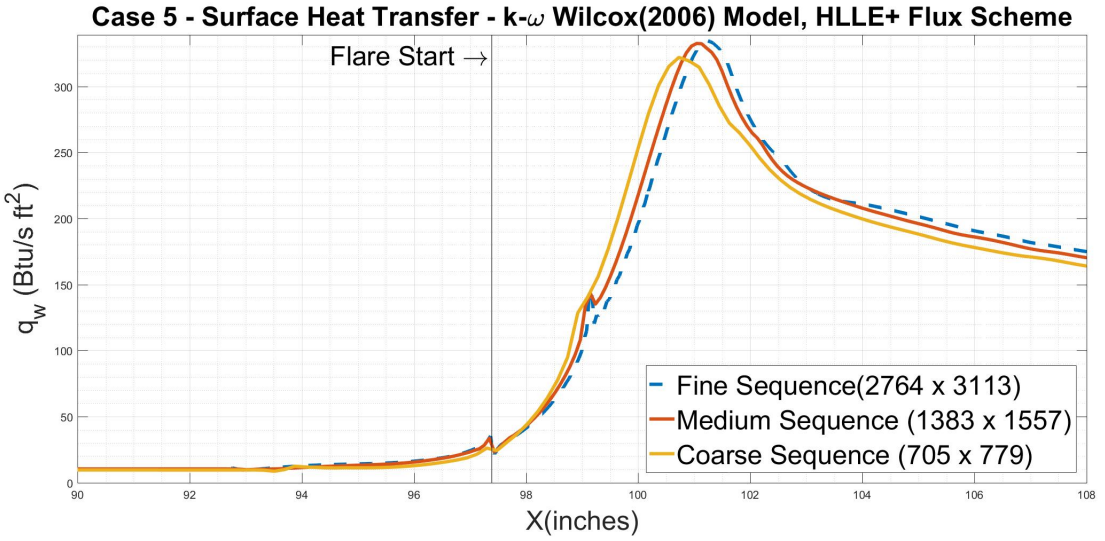

Figure 5.10: Case 5: Surface Heat Transfer - Grid Convergence Study

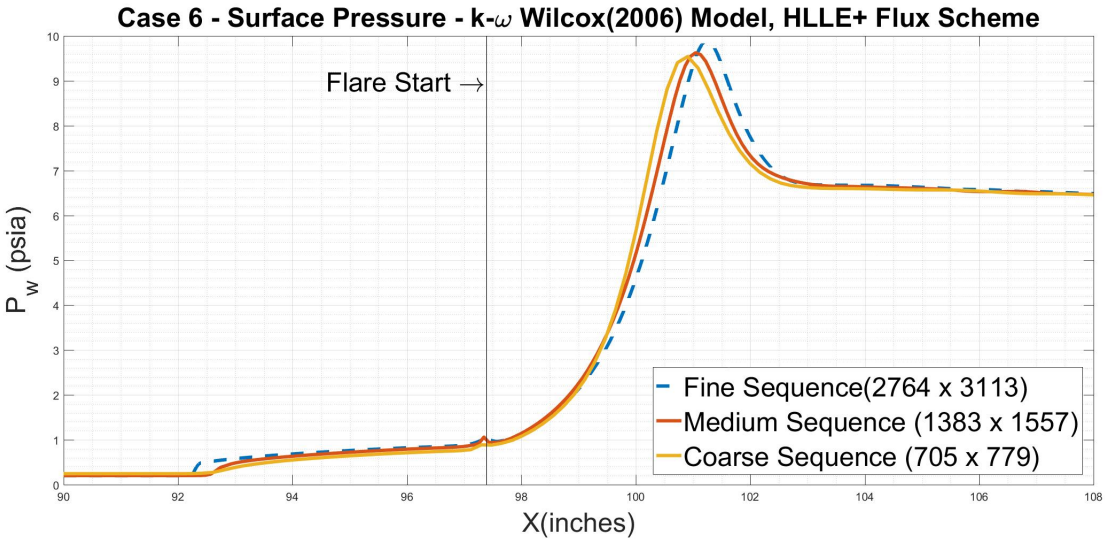

Figure 5.11: Case 6: Surface Pressure - Grid Convergence Study

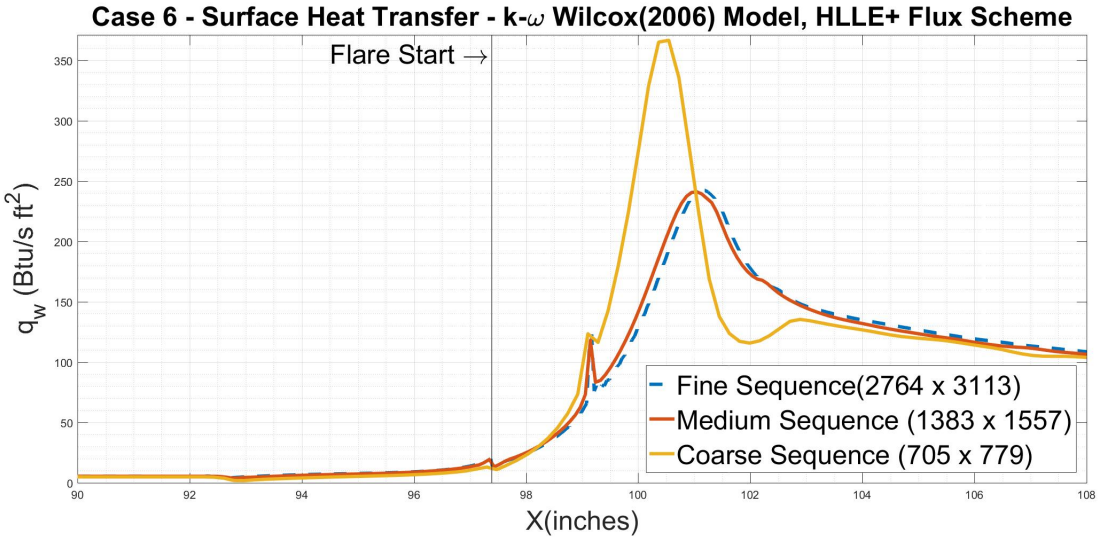

Figure 5.12: Case 6: Surface Heat Transfer - Grid Convergence Study

5.2 Evaluation of Flux Schemes

In this section, the final results for three Euler flux schemes, Roe, HLLE+, and AUSM+, is presented for all six cases. Since the HLLE+ flux scheme is basically a modified Roe scheme for achieving faster grid independence, the percentage difference between results from HLLE+ and AUSM+ flux schemes have been plotted on the right y axis of the following plots. The purpose of this section is to understand the influence of inviscid flux formulation on the uncertainty in the computation.

Change Between Two Most Different Results for Each Case				
Case	Separation Location $inch$ (%)	Re-attachment Location $inch$ (%)	Peak Surface Pressure $psia$ (%)	Peak Surface Heat Transfer $Btu/(s \cdot ft^2)$ (%)
1	0.18 (0.20%)	0.18 (0.18%)	0.28 (1.48%)	3.14 (2.27%)
2	0.14 (0.15%)	0.18 (0.18%)	0.29 (0.79%)	10.18 (4.33%)
3	0.05 (0.05%)	0.05 (0.04%)	0.23 (1.79%)	6.31 (4.10%)
4	0.09 (0.10%)	0.14 (0.13%)	1.68 (4.61%)	24.14 (6.86%)
5	0.23 (0.24%)	0.05 (0.04%)	0.49 (2.88%)	7.40 (2.27%)
6	0 (0%)	0.09 (0.09%)	0.12 (1.20%)	7.96 (3.39%)
Average	0.12 (0.12%)	0.12 (0.11%)	0.52 (2.13%)	9.86 (3.87%)

Table 5.2: Evaluation of Flux Algorithms

For all three flux schemes, the prediction of separation and re-attachment locations is in close agreement for each case. The change in peak surface pressure is within 2.88% except for case 4 (4.61%) and the change in peak heat transfer is within 4.33% except for case 4 (6.86%). Hence, it is clear that all the flux schemes are predicting flow characteristics within 5% accuracy for nearly all cases. In general, the AUSM+ flux scheme is showing slightly different result than results from HLLE+ and Roe flux schemes. Similar behavior is seen for case 4 with slightly larger change in results compared to other cases.

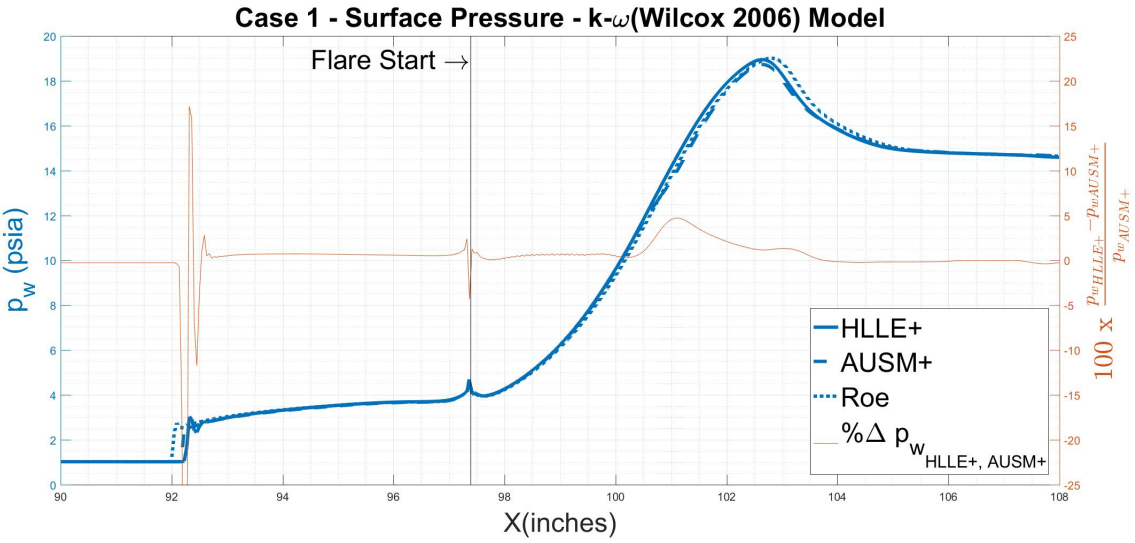

Figure 5.13: Case 1: Surface Pressure - Flux Scheme Evaluation

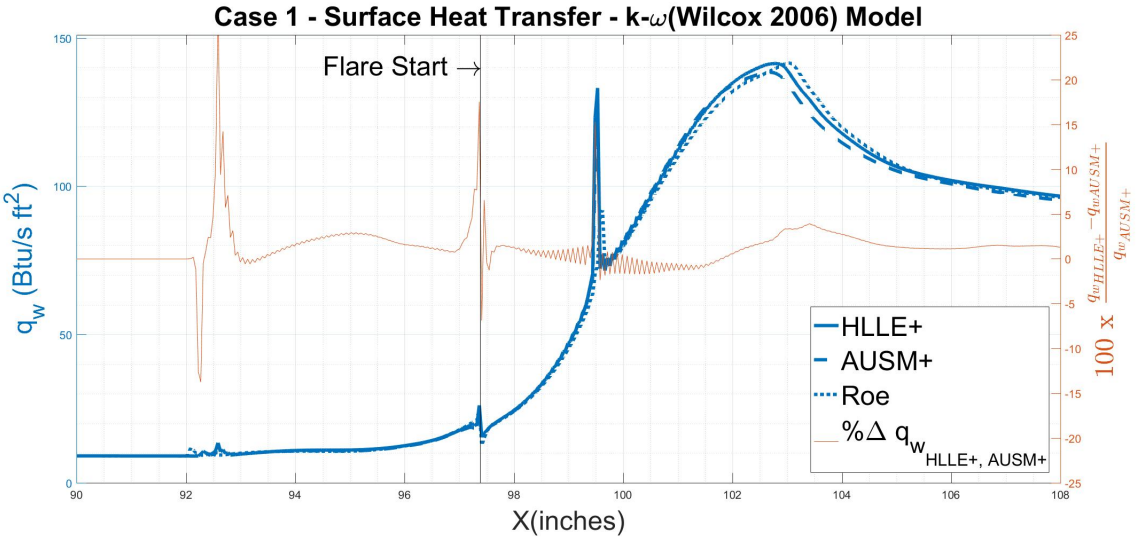

Figure 5.14: Case 1: Surface Heat Transfer - Flux Scheme Evaluation

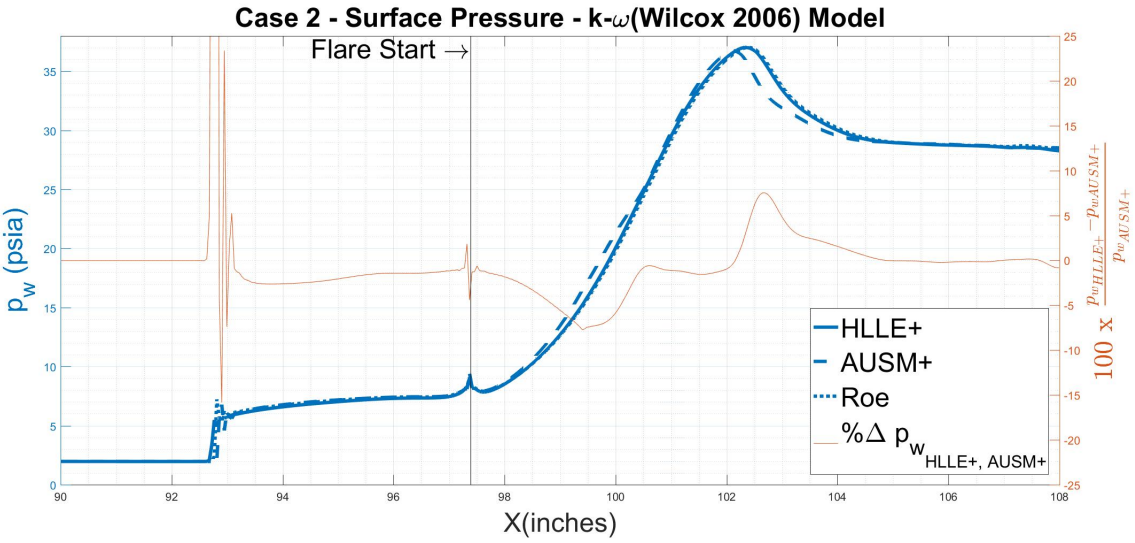

Figure 5.15: Case 2: Surface Pressure - Flux Scheme Evaluation

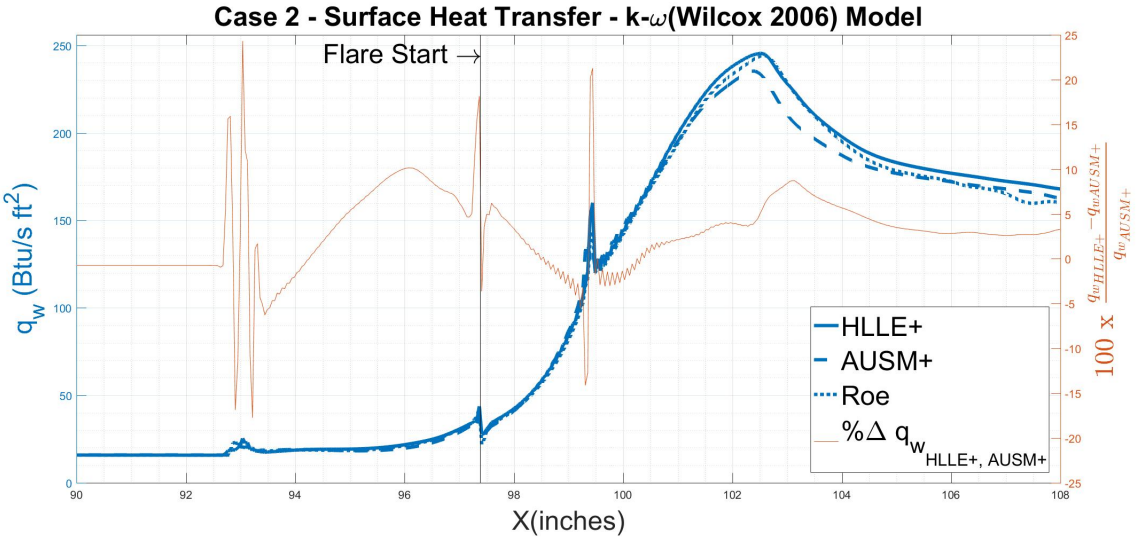

Figure 5.16: Case 2: Surface Heat Transfer - Flux Scheme Evaluation

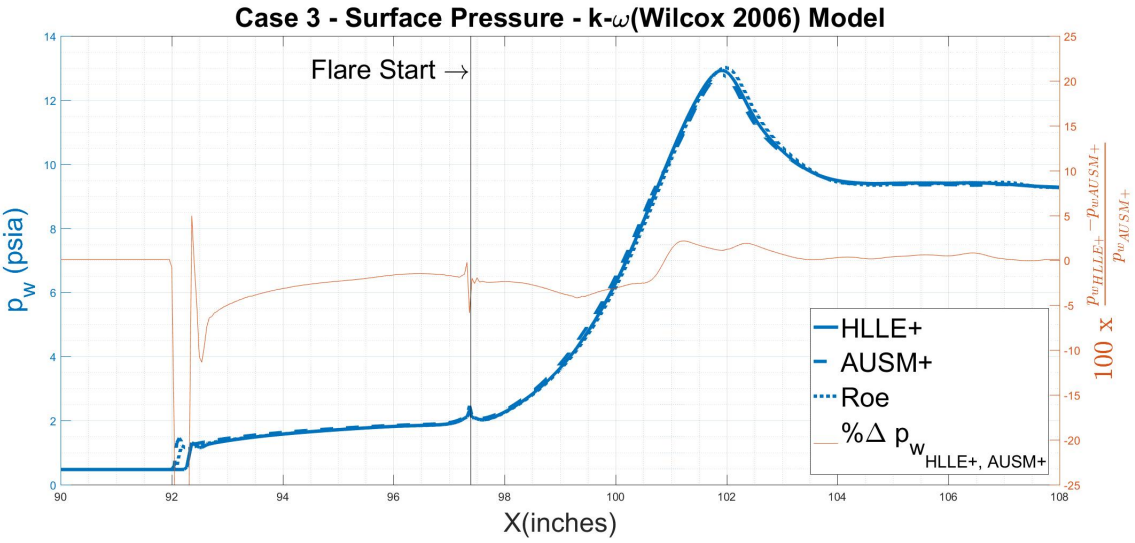

Figure 5.17: Case 3: Surface Pressure - Flux Scheme Evaluation

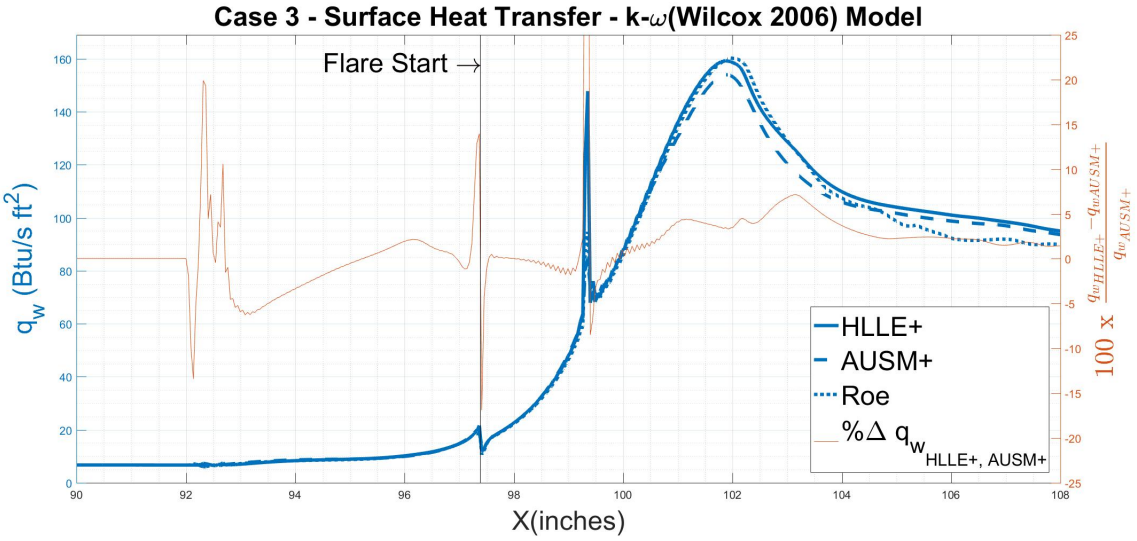

Figure 5.18: Case 3: Surface Heat Transfer - Flux Scheme Evaluation

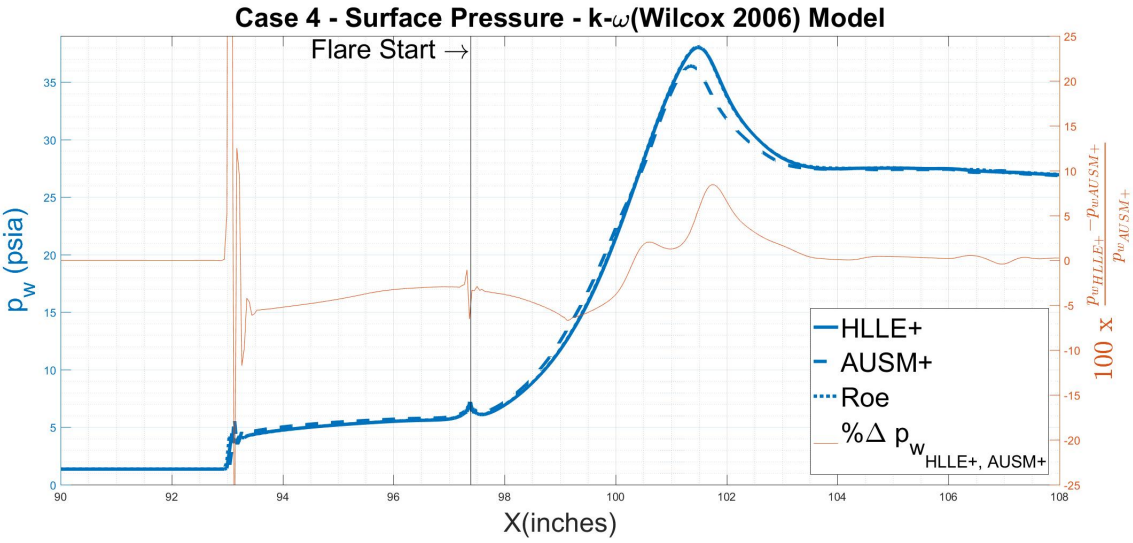

Figure 5.19: Case 4: Surface Pressure - Flux Scheme Evaluation

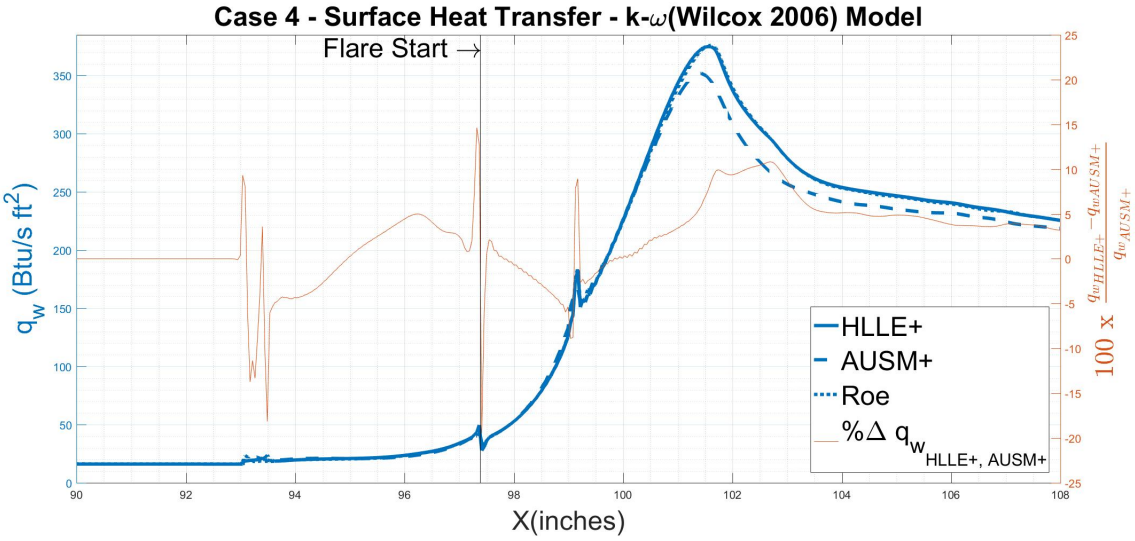

Figure 5.20: Case 4: Surface Heat Transfer - Flux Scheme Evaluation

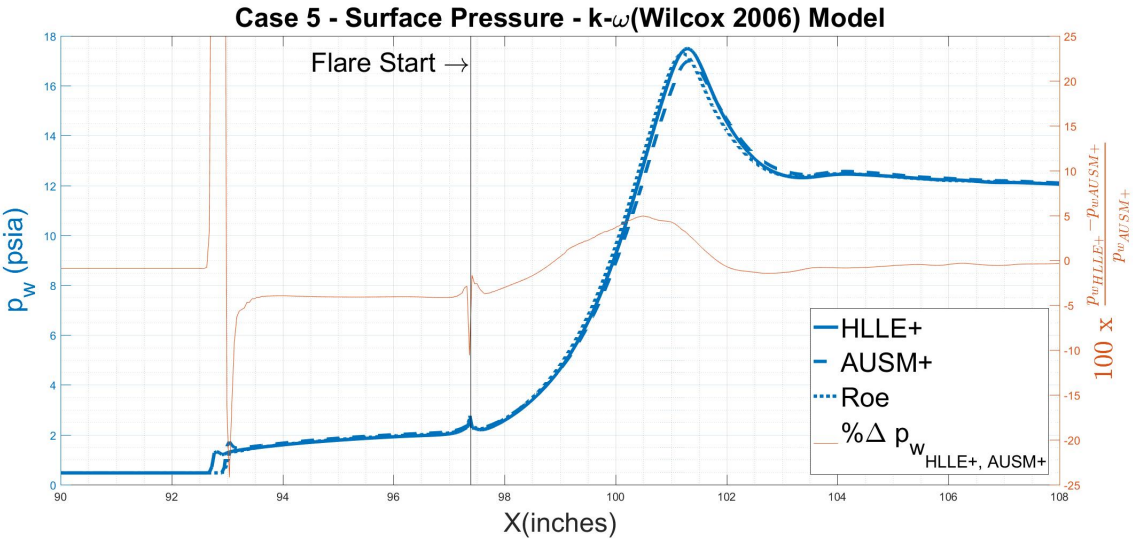

Figure 5.21: Case 5: Surface Pressure - Flux Scheme Evaluation

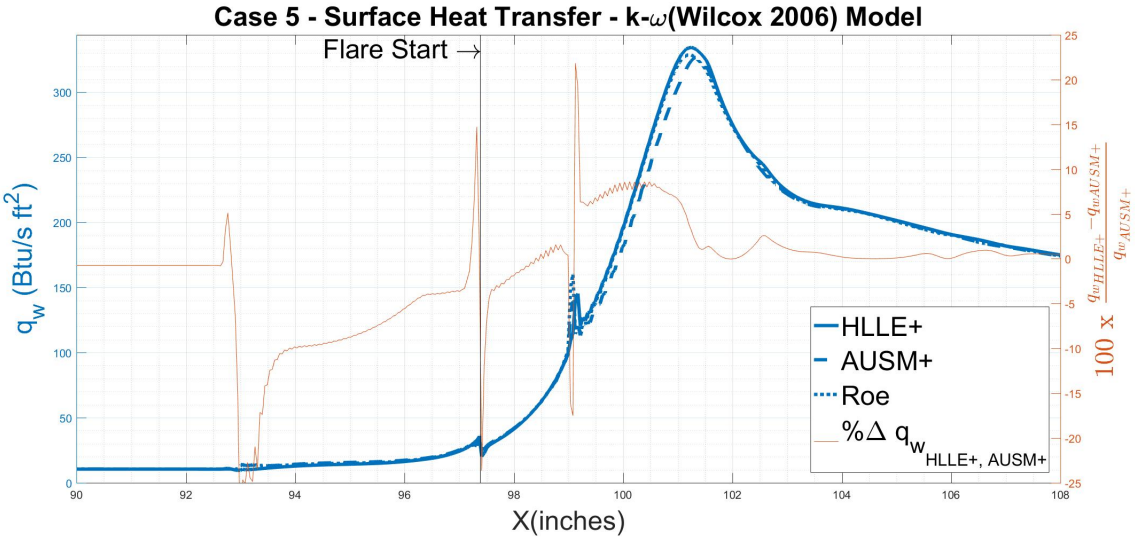

Figure 5.22: Case 5: Surface Heat Transfer - Flux Scheme Evaluation

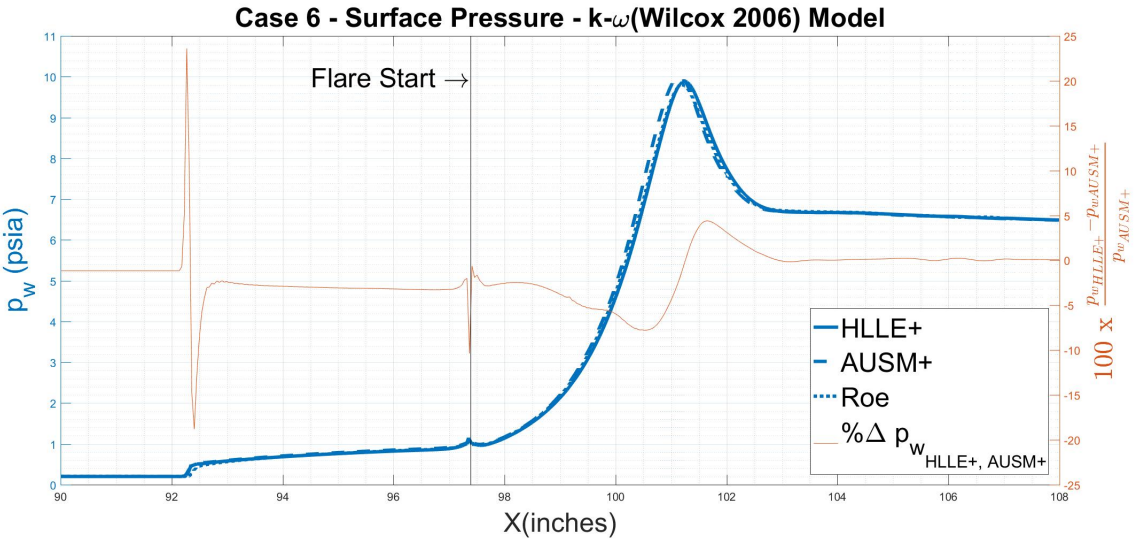

Figure 5.23: Case 6: Surface Pressure - Flux Scheme Evaluation

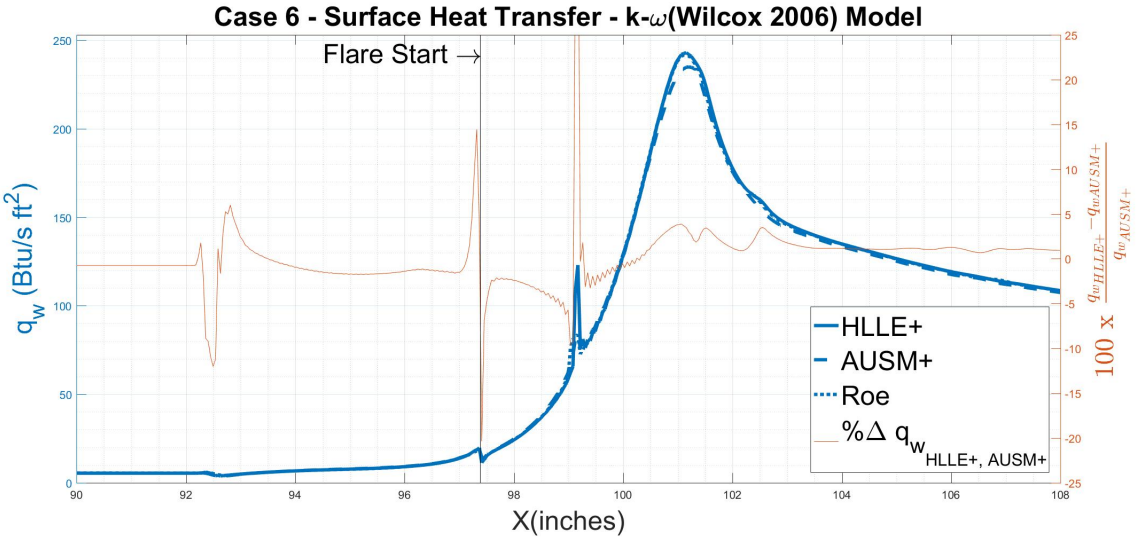

Figure 5.24: Case 6: Surface Heat Transfer - Flux Scheme Evaluation

5.3 Effects of Flux Limiters and Compressibility Correction

In this section, two solver parameters, flux limiters and compressibility correction, are presented for only case 1.

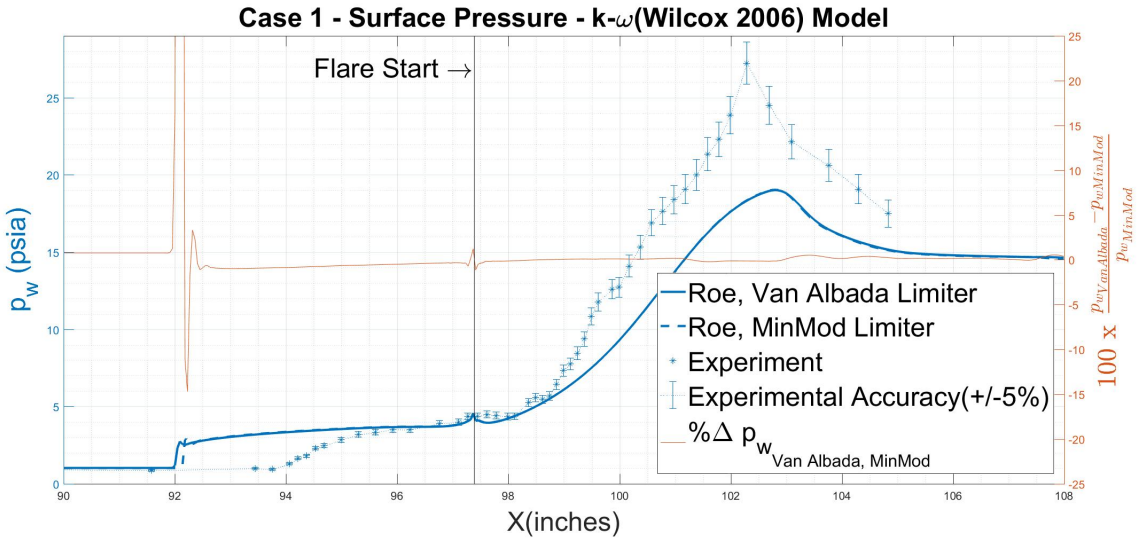

Figure 5.25: Case 1: Surface Pressure - Flux Limiters

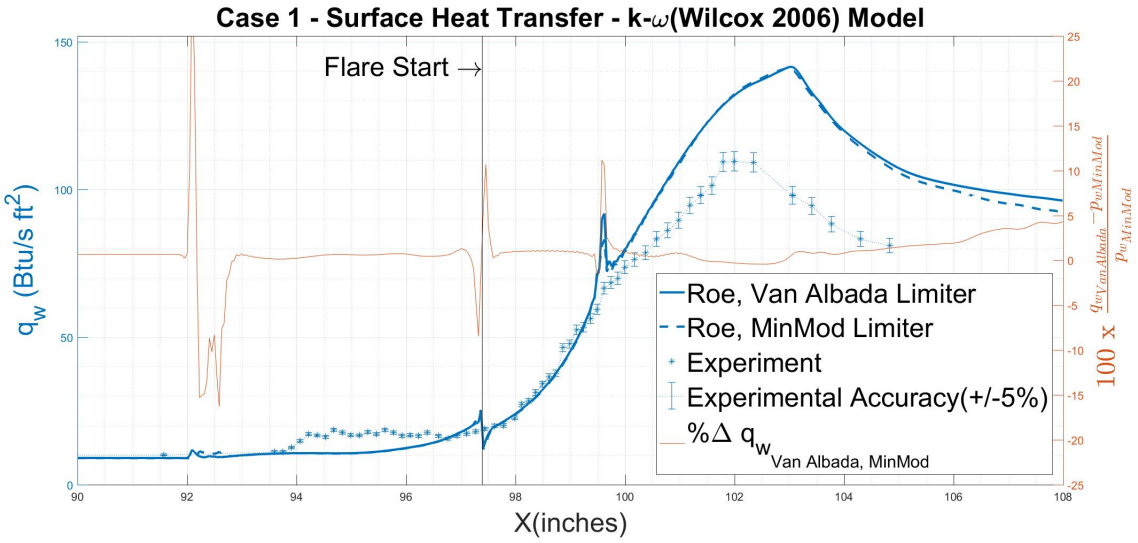

Figure 5.26: Case 1: Surface Heat Transfer - Flux Limiters

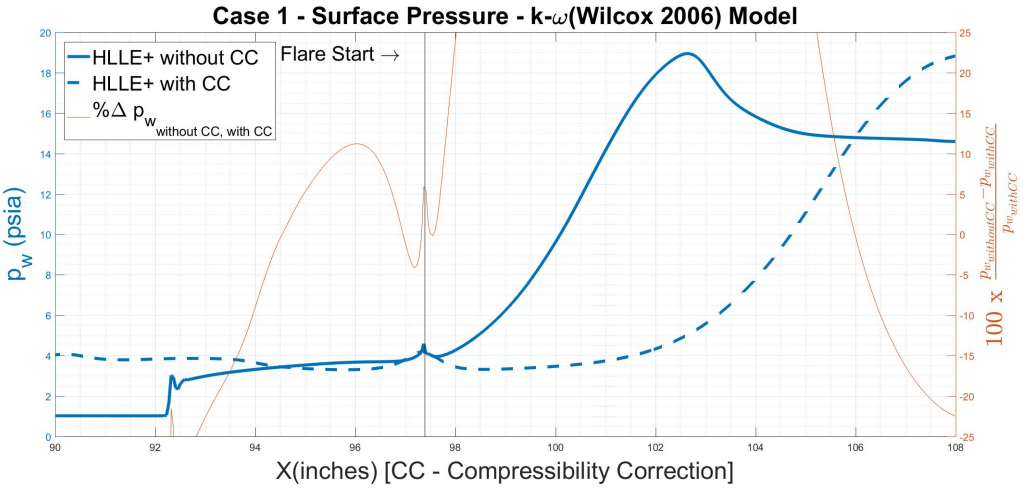

Figure 5.27: Case 1: Surface Pressure - Compressibility Correction

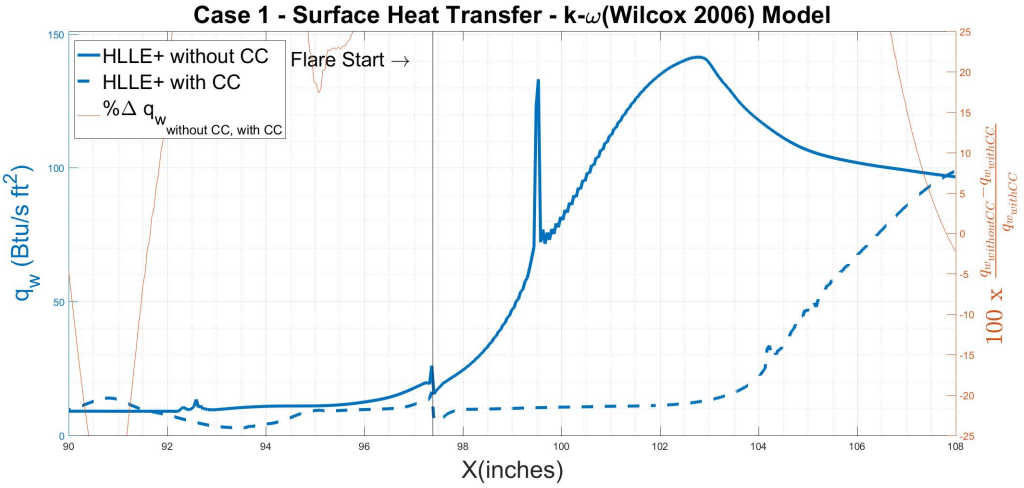

Figure 5.28: Case 1: Surface Heat Transfer - Compressibility Correction

Although MinMod limiter is claimed to be dissipative, results are matching well with VanAlbada flux limiter. Hence, both the flux limiters are expected to give identical results. On the other hand, the Wilcox (2006) $k-\omega$ with the compressibility correction doesn't yield any improvement in the results. The correction increases the dissipation of turbulence kinetic energy, thus reducing the spreading or mixing rate [20]. For wall bounded flows, the compressibility correction should (in theory) not have any impact on the solution. This however is not always the case [28].

5.4 Comparison with Experimental Data

In this section, we compare the CFD results with experiment to assess the aerothermodynamic load prediction capabilities of the $k-\omega$ Wilcox (2006) turbulence model (without the compressibility correction) with the HLLE+ flux scheme. The HLLE+ flux scheme has been chosen for the sake of consistency with previous sections. Also, as shown in the last section, all the flux schemes predict flow separation and re-attachment location within less than 1% difference. Similarly, the peak surface pressure and the peak surface heat transfer have been estimated within 5% and 7% difference respectively. Hence, we can compare results from only one flux scheme for the sake of simplicity.

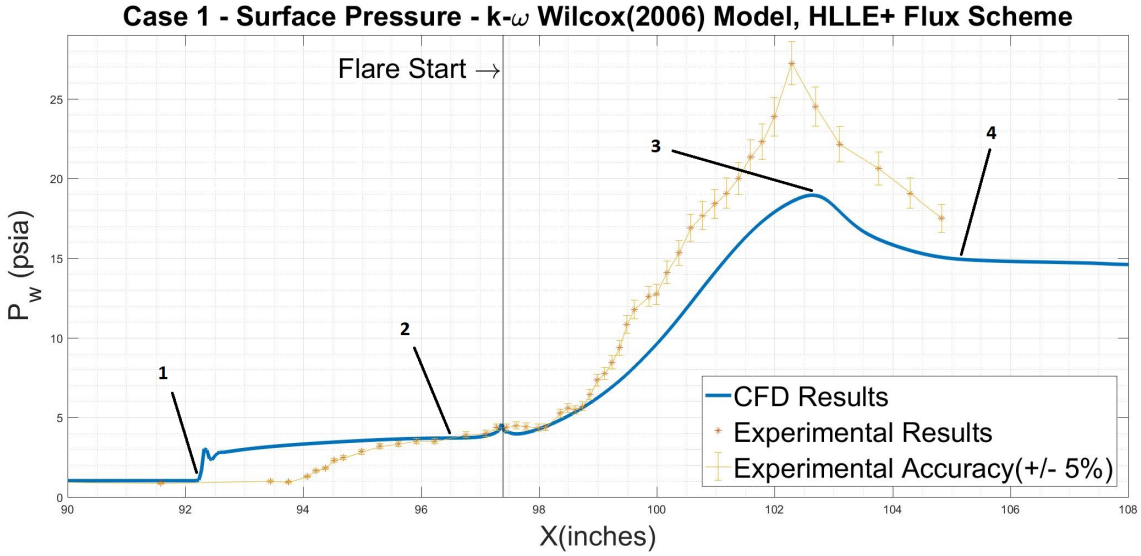

Figure 5.29: Case 1: Surface Pressure - Comparison with Experimental Data
1. Flow Separation Location, 2. Plateau Region, 3. Flow Re-attachment Location, 4. Recovery Region

(i) Flow Separation Location

A boundary layer displacement shock forms from the beginning of the sharp edge due to the existence of the boundary layer. The flare shock imposes an adverse pressure gradient on the flow and separates the boundary layer and creates a separated region. As shown in Table 5.3, $k-\omega$ Wilcox (2006) turbulence model consistently predicts flow separation location on average 2% upstream of experimental results. It is interesting

to note that all simulations slightly over predicted the size of the separation zone, and predicted excessive heating at the re-attached location after separation. Also, the flare upstream conditions are matching well with the experimental results for all the cases.

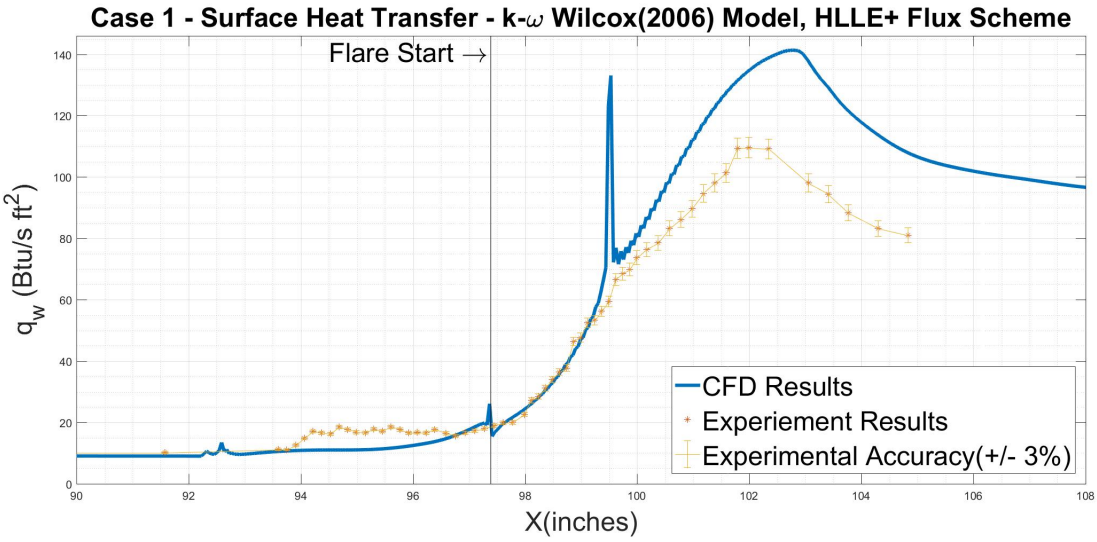

Figure 5.30: Case 1: Surface Heat Transfer - Comparison with Experimental Data

Difference Between CFD and Experimental Results					
Case	Separation Location *inch* (%)	Re-attachment Location *inch* (%)	Peak p_w *psia* (%)	Peak q_w $Btu/(s \cdot ft^2)$ (%)	Average p_w Plateau Region *psia* (%)
1	-1.79 (-1.90%)	0.35 (0.35%)	-8.29 (-30.44%)	31.88 (29.10%)	-0.17 (-4.19%)
2	-1.34 (-1.42%)	0.54 (0.53%)	-6.65 (-15.22%)	76.19 (45%)	0.2 (2.66%)
3	-1.79 (-1.90%)	-0.07 (-0.07%)	-0.62 (-4.56%)	58.64 (58.26%)	0.09 (4.75%)
4	-1.18 (-1.25%)	-0.12 (-0.11%)	3.22 (9.25%)	160.07 (74.53%)	1.09 (23.28%)
5	-1.49 (-1.59%)	-0.50 (-0.49%)	-0.60 (-3.33%)	112.97 (51.02%)	-0.14 (-6.28%)
6	-3.65 (-3.80%)	1.38 (1.38%)	1.13 (12.86%)	92.99 (62.04%)	0.03 (2.98%)

Table 5.3: Comparison with Experimental Results

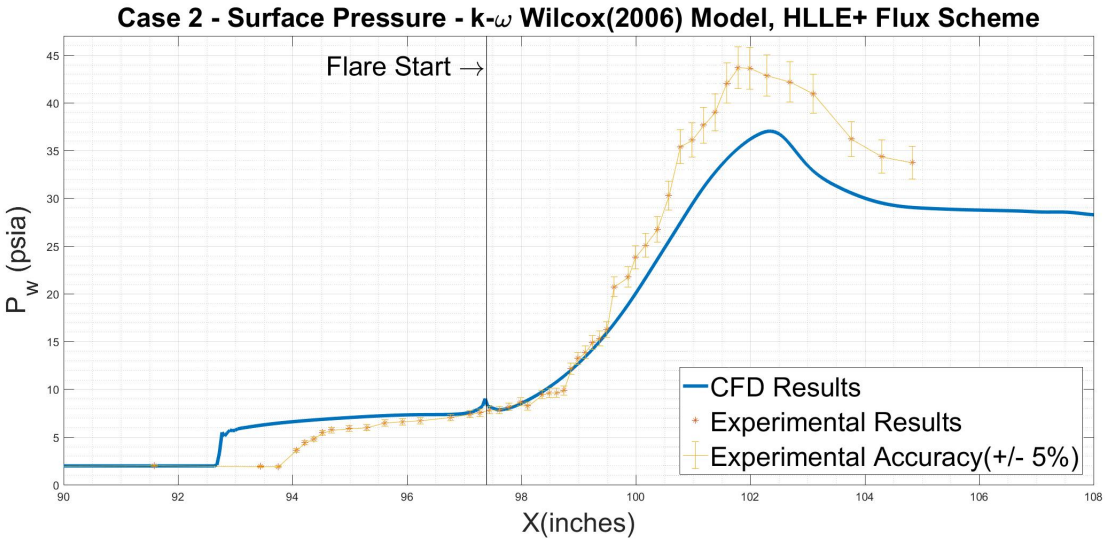

Figure 5.31: Case 2: Surface Pressure - Comparison with Experimental Data

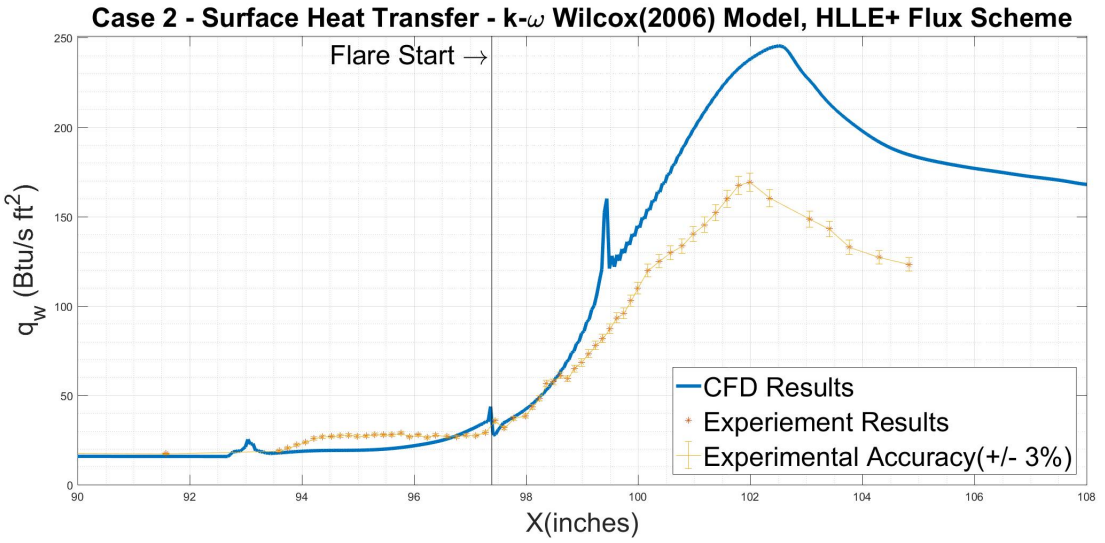

Figure 5.32: Case 2: Surface Heat Transfer - Comparison with Experimental Data

(ii) Plateau Region

Separated flow travels some distance past the beginning of the flare to re-attach at the flare wall. In between, the flow passes through a plateau region where pressure becomes constant. It is found that the separation and reattachment regions tend to become distinct, with an intervening plateau region of nearly constant pressure, as the shock strength increases. Although size of plateau region is largely over predicted, the surface plateau pressure has been accurately predicted within 6% (except case 4

- 23%) for plateau region for all the cases using the $k-\omega$ Wilcox (2006) turbulence model.

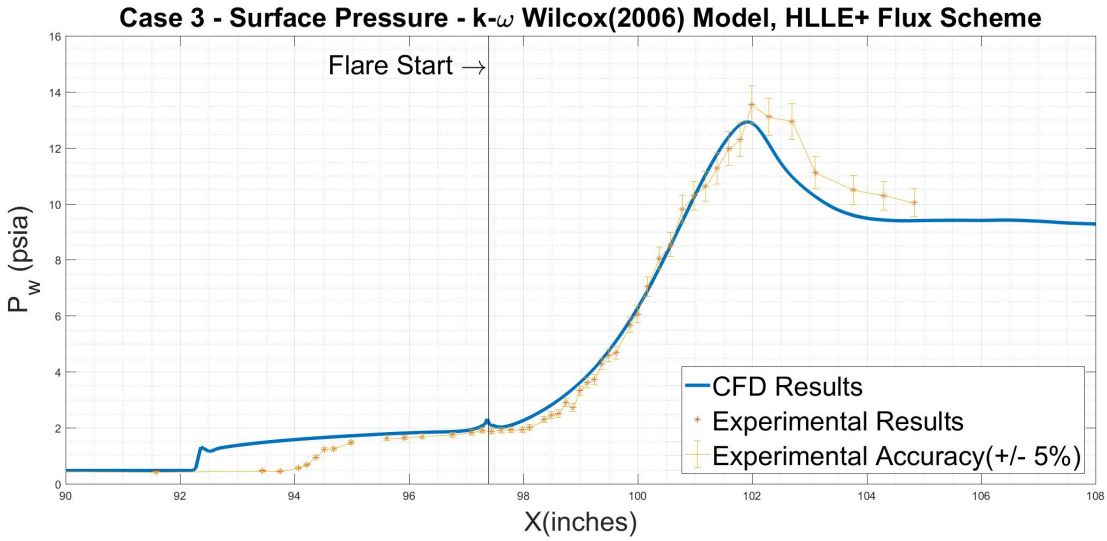

Figure 5.33: Case 3: Surface Pressure - Comparison with Experimental Data

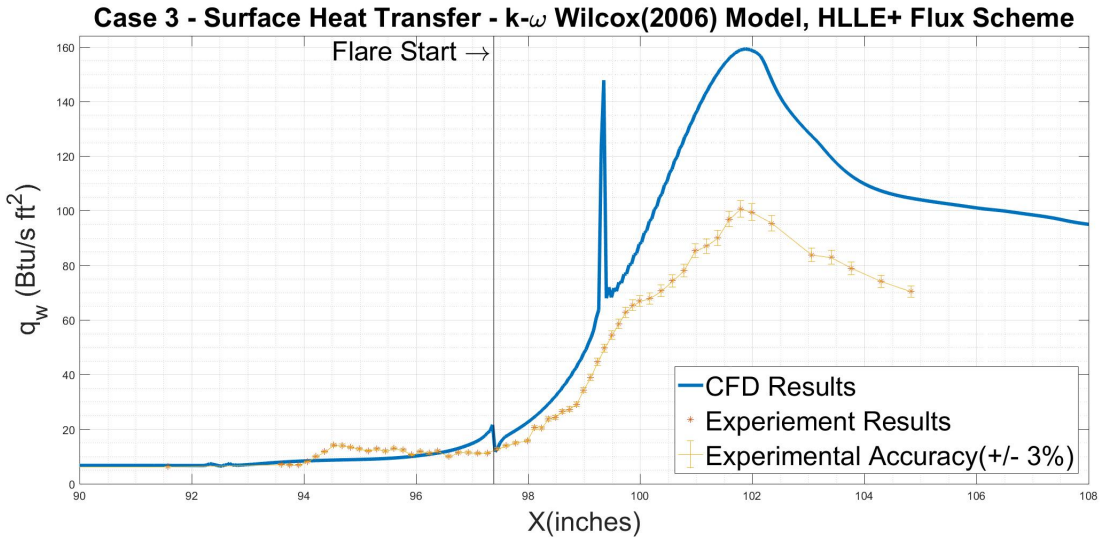

Figure 5.34: Case 3: Surface Heat Transfer - Comparison with Experimental Data

(iii) Re-attachment Location

A separated shock forms over the separated zone and meets the boundary layer displacement shock at the reattachment point where the surface pressure and surface heat transfer are increased. As shown in Table 5.3, $k-\omega$ Wilcox (2006) turbulence

model consistently predicts flow re-attachment location within 1% downstream of experimental results.

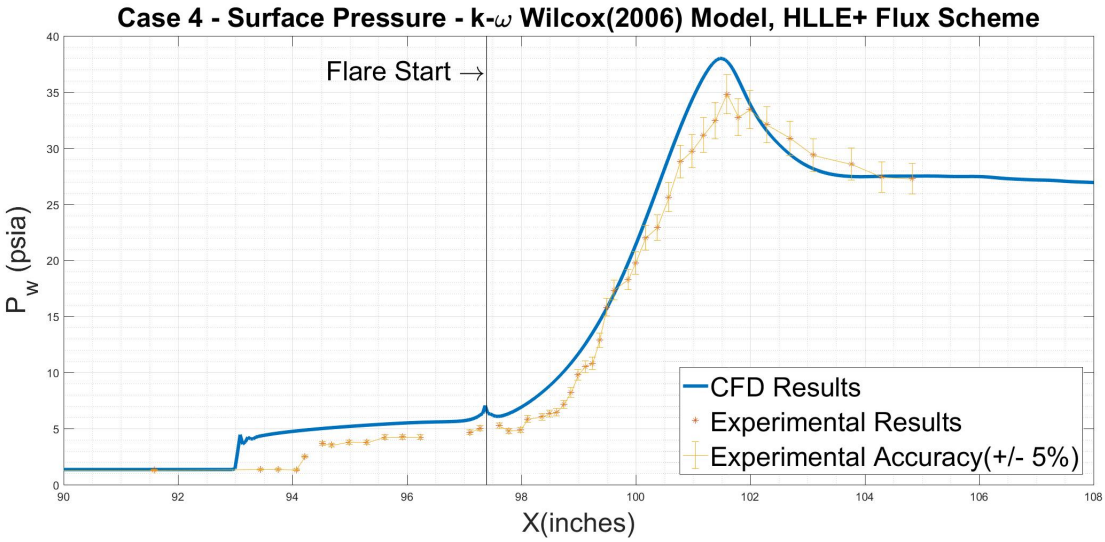

Figure 5.35: Case 4: Surface Pressure - Comparison with Experimental Data

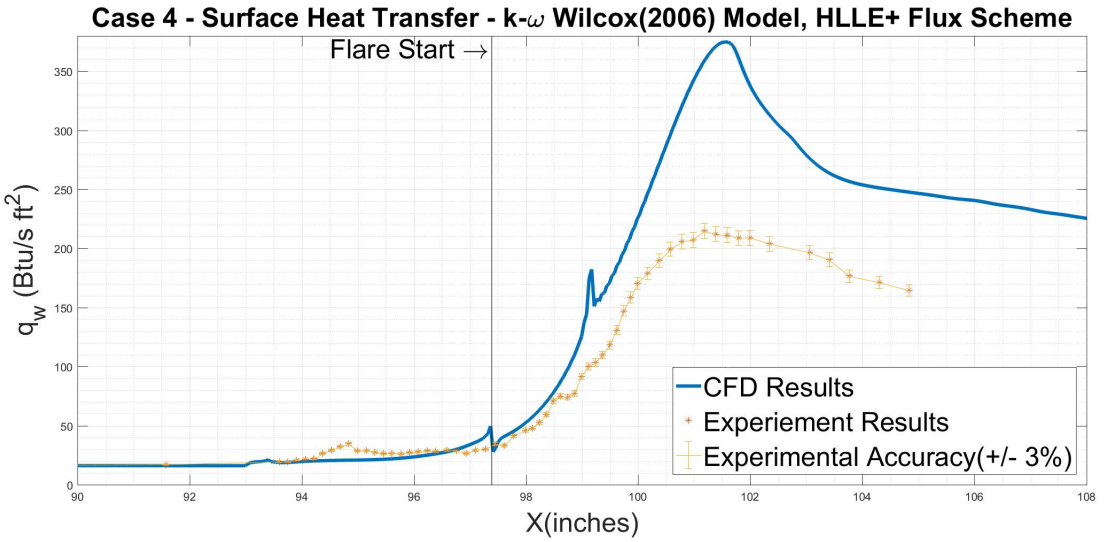

Figure 5.36: Case 4: Surface Heat Transfer - Comparison with Experimental Data

(iv) Peak Surface Pressure, p_w

The peak surface pressure is achieved at the flow re-attachment location. It is observed that $k-\omega$ Wilcox (2006) turbulence model typically underpredicts the peak surface pressure. The $k-\omega$ turbulence model underpredicts the peak surface pressure for

four out six cases. The peak surface pressure, p_w, is off by -3% to -30%. The error in prediction has been greatly varying which suggests that the turbulence model is not reliable to predict the peak surface pressure within a certain percentage error.

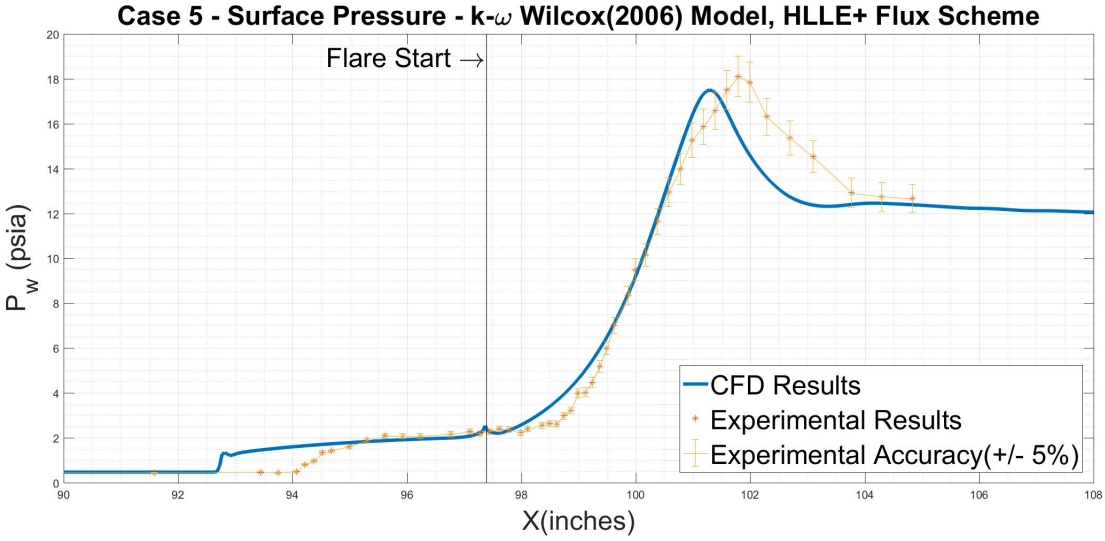

Figure 5.37: Case 5: Surface Pressure - Comparison with Experimental Data

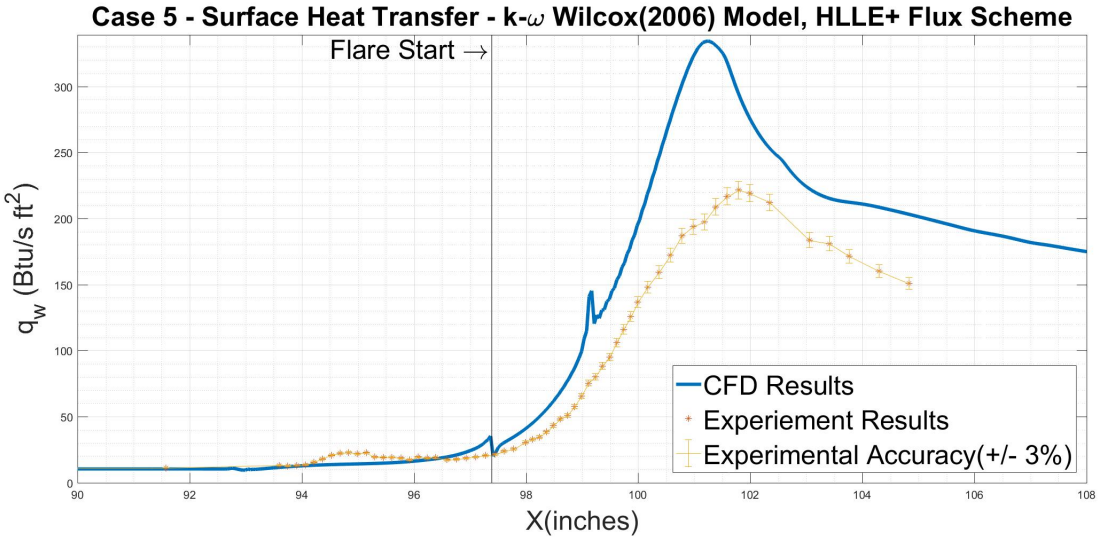

Figure 5.38: Case 5: Surface Heat Transfer - Comparison with Experimental Data

(v) Peak Surface Heat Transfer, q_w

The peak surface heat transfer is achieved at the flow re-attachment location. It is observed that the $k-\omega$ Wilcox (2006) turbulence model consistently overpredicts

the peak surface heat transfer. It is clear from Table 5.3 that $k-\omega$ Wilcox (2006) turbulence model over predicts the peak surface heat transfer from 29% to 75%.

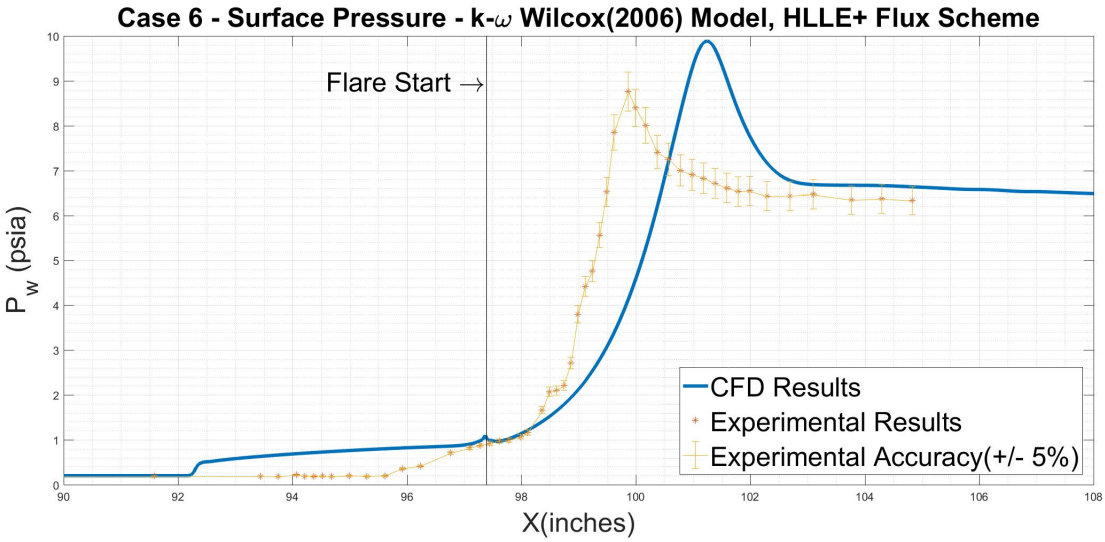

Figure 5.39: Case 6: Surface Pressure - Comparison with Experimental Data

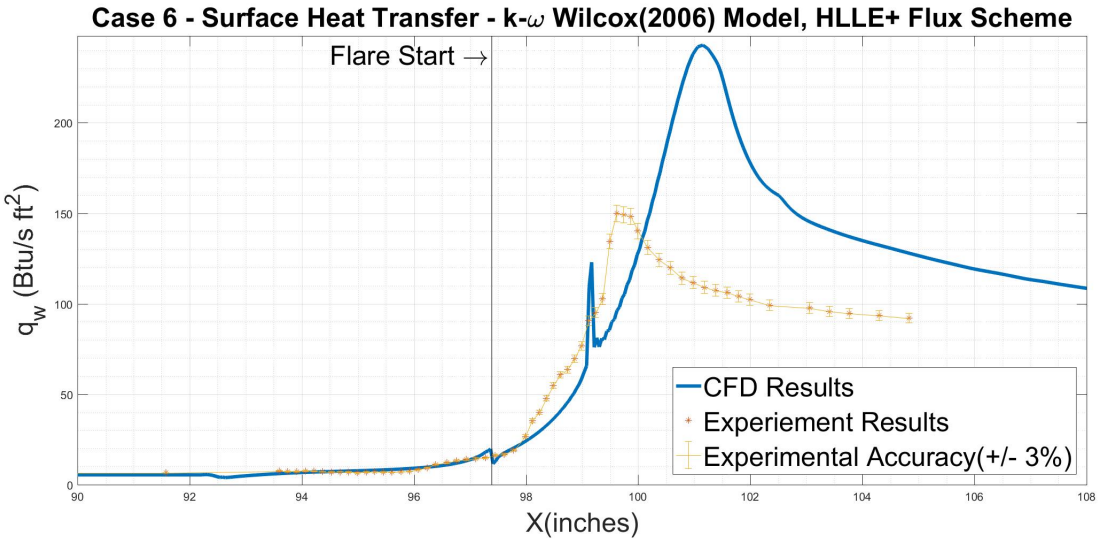

Figure 5.40: Case 6: Surface Heat Transfer - Comparison with Experimental Data

(vi) Recovery Downstream of Peak Aerothermodynamic Load

The flare shock bends when it interacts with the expansion waves created from the edge of the cylinder downstream of the flare. Before re-attachment shock wave interacts with expansion waves, there will be a recovery region where aerothermodynamic

properties i.e., surface pressure, surface heat transfer recovers to a constant value after flow re-attachment. It is observed that surface pressure in recovery region is accurately predicted in cases 3,4,5 and 6. Although p_w is off by few percentage points in cases 1 and 2, it shows accurate trend in pressure gradient. Surface heat transfer, q_w, is consistently overpredicted in recovery region.

5.5 Flow Structure

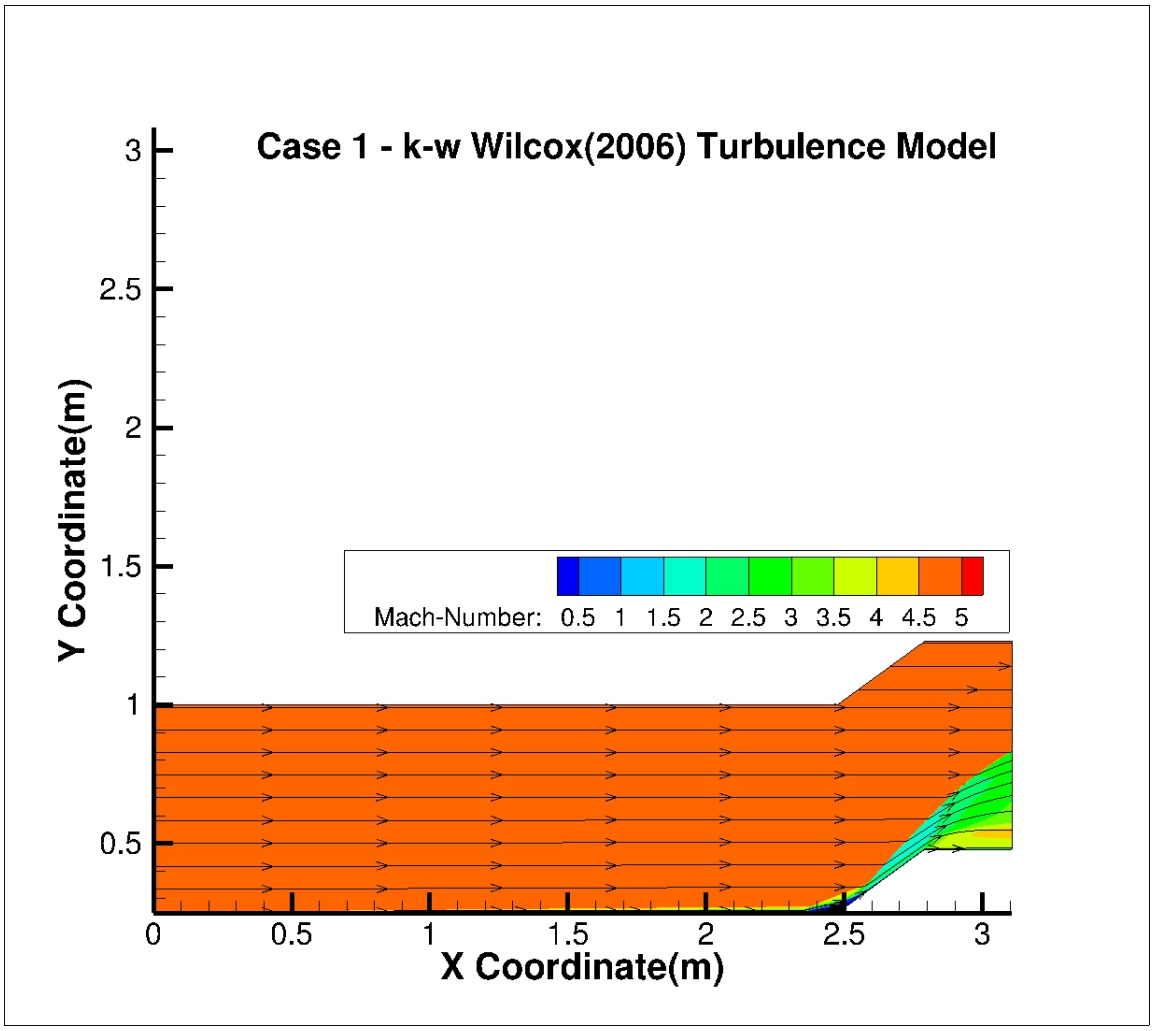

Figure 5.41: Contours of Local Mach Number with Superposed In-plane Streamlines

In this section, we will take a look at different shock waves and flow behavior for one of the cases which will represent the flow structure for all the cases. Mach number contours and

streamlines are shown in Figure 5.41.

Figure 5.42 shows the flow structure of the hypersonic flow over large hollow cylinder flare. The recirculation of the flow in the separated region can be seen with help of streamlines. Any rise in pressure provokes greater retardation in regions where the stagnation pressure is lowest that is, in the boundary-layer inner part. By imposing an adverse pressure gradient, a situation can be reached in which the flow adjacent to the wall is stagnated or reversed so that a *separated region* forms. Downstream of separation point is a *recirculating bubble* flow, which separates the recirculating flow from the flow streaming from upstream to downstream. This separation bubble will have near constant pressure which creates plateau region as seen in the previous section.

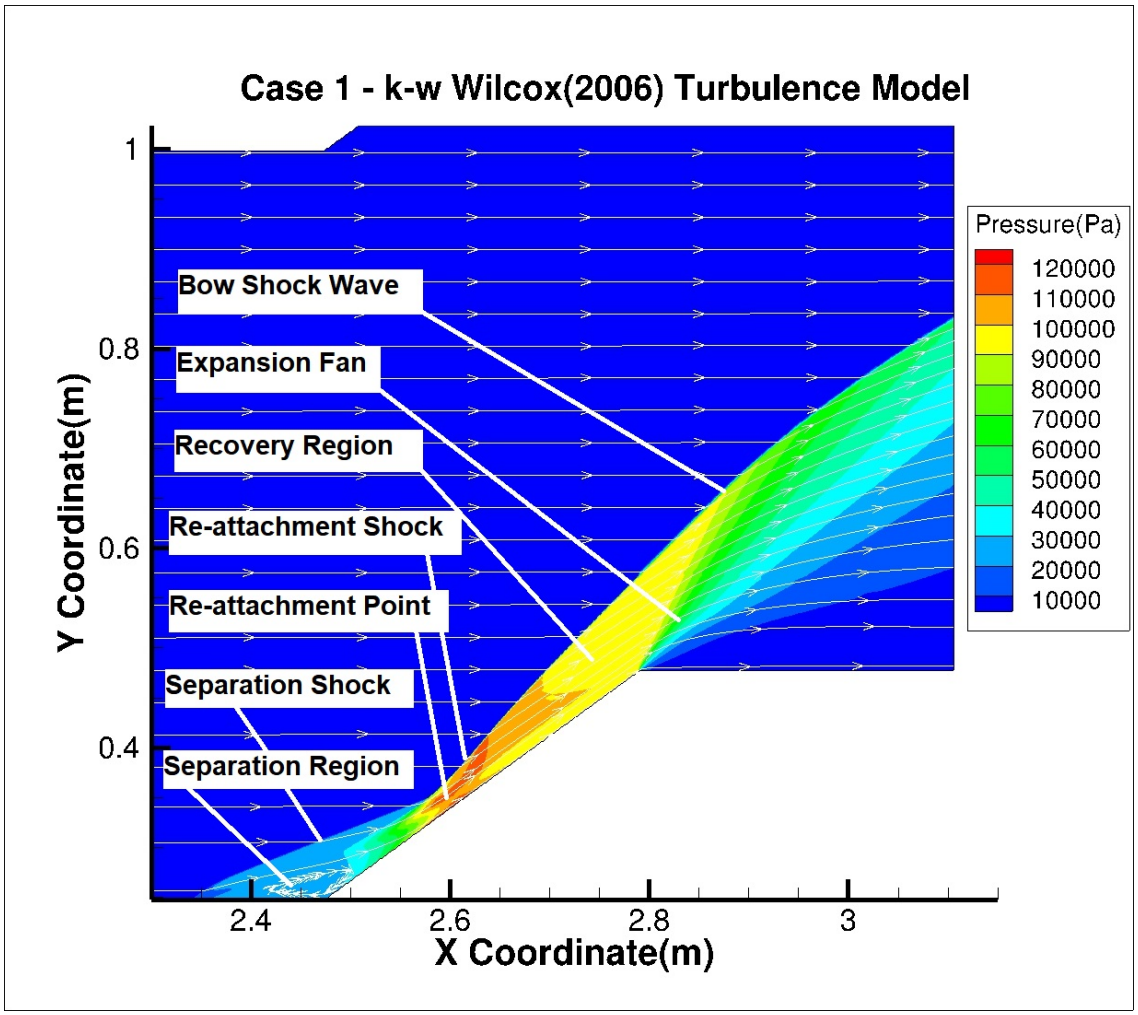

Figure 5.42: Pressure Contours

Due to the action of the strong mixing taking place in the detached shear layer emanating from separation point, a mechanical-energy transfer occurs from the outer high-speed flow towards the separated region. As a consequence, the velocity on the dividing streamline steadily increases until the deceleration associated with the reattachment process starts. Hence, we get peak aerothermodynamic loading at the re-attachment location. The transmitted shock, separation shock, penetrates the separated viscous flow, where it is reflected as an expansion wave because there is a near-constant pressure level in the bubble. This causes a deflection of the shear layer towards the wall, where it eventually reattaches at the *re-attachment point*. This process is accompanied by a sequence of compression waves that coalesce into a reattachment shock in the outer stream.

The wall-pressure distribution initially exhibits a steep rise, associated with separation, followed by a plateau typical of separated flows. A second, more progressive pressure rise occurs during reattachment. Downstream of the re-attachment point, flow recovers to a constant pressure and heat transfer which drops drastically with expansion fan at the end of the flare. As it can be seen in the Figure 5.42, the re-attachment shock converts into a bow shock due to the expansion fan.

5.6 Anomalous Behavior of Turbulence Model

In this section, an unphysical prediction of turbulence kinetic energy by the $k-\omega$ Wilcox (2006) turbulence model is presented. As shown in Figure 5.43, there is an unphysical spike in turbulence kinetic energy at about 3 inches upstream of re-attachment point for case 3. The energy dissipation rate, ω, is at peak at the re-attachment point. Similar behavior is present for all 6 cases. The reason behind this behavior was not investigated. Also, the grid refinement studies concentrated near the unphysical spike had been carried out which yielded no significant improvements in the results. When we take a look at surface temperature profiles near wall, we observe similar spikes in the temperature values as shown in the Figure 5.44.

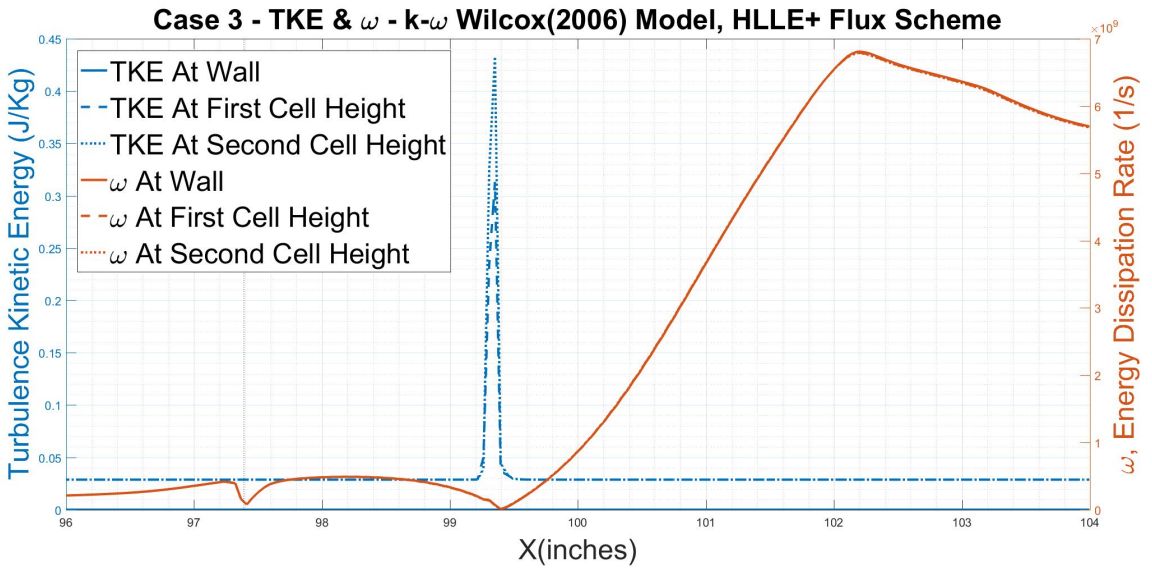

Figure 5.43: Case 3: Turbulent Kinetic Energy and Energy Dissipation Rate

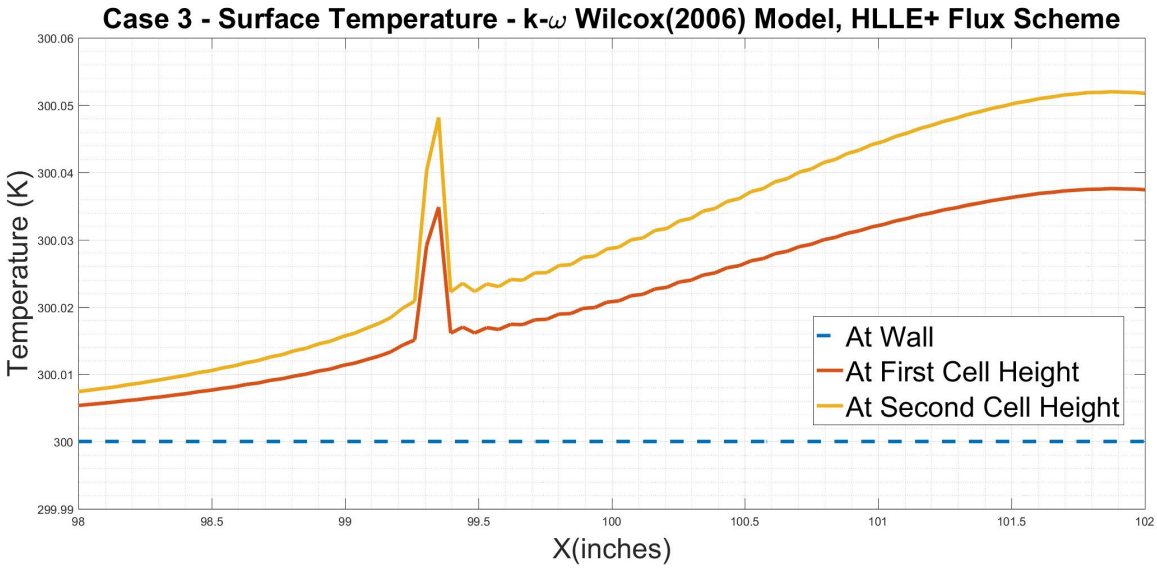

Figure 5.44: Case 3: Surface Temperature

Chapter 6

Conclusion

A series of numerical simulations have been conducted for Mach numbers ranging from 5 to 8 for assessing aerothermodynamic load prediction capability of the $k-\omega$ Wilcox (2006) turbulence model. In addition to that, the effects of the compressibility correction and flux limiters, an assessment of appropriate mesh density with series of 10 different Plot3d grids generated in C++, and evaluation of three Euler flux algorithms have been carried out. The driving factors for creating series of grids have been the percentage changes in the solution between last two grid sequences, flow resolution near critical regions (i.e., separation and re-attachment regions) and comparison with experimental results. In judging the results, we should keep in mind that the purpose of this computational study is the assessment of computational techniques and not the investigation of the physics of the hollow cylinder/flare flow.

- It has been found that the three Euler flux schemes predict the flow features within 1% accuracy of each other.
- The $k-\omega$ Wilcox (2006) turbulence model consistently underpredicts peak surface pressure at the wall except in two cases and overpredicts peak heat transfer at wall. The peak surface pressure, p_w, is off by -3% to -30% and the peak surface heat transfer, q_w, is off by 29% to 74% from experimental results. This suggests that a large correction factor should be implemented while converting computational results into critical design decisions for hypersonic vehicles.

- Also, the $k-\omega$ turbulence model overpredicts the size of the separation region along the length of cylinder/flare by about 2% due to prediction of separation point upstream of experimental results and prediction of re-attachment point downstream of experimental results. This can significantly affect design of control surfaces (i.e., wings, grid fins, rudder, ailerons, flaps) and result in loss of maneuverability in real flight.

- An anomalous behavior of current $k-\omega$ model is found in prediction of surface heat transfer which corresponds to turbulent kinetic energy (TKE). The unphysical spike in q_w is found to be present in all six cases at about 2-3 inches upstream of re-attachment point.

Chapter 7

Future Work

- The anomalous behavior of the the $k-\omega$ Wilcox (2006) turbulence model should be studied and required improvements can be suggested. Also, it would be beneficial to compare the current turbulence model with other turbulence models. Any anomalous behavior of other models should be examined also.

- The current computations are based on RANS model which gives time averaged solution over a time period which is considerably higher than time constant of velocity fluctuations. For better visualization of turbulent eddies and get more insight into the flow, LES or Hybrid RANS/LES methods can be utilized.

- Although most recent studies on fundamental physics have focused on nominally two-dimensional and axisymmetric configurations, three-dimensional interactions have fundamentally different kinematic structure in the mean sense. They are likely to be a renewed focus going forward.

References

[1] E Musk. Hyperloop Alpha. *(PDF). SpaceX. Retrieved August*, 12, 2013.

[2] Uber. Fast-Forwarding to a Future of On-Demand Uber Air Transportation. *(PDF). Retrieved October*, 27, 2016.

[3] Boom Technology. Boom Supersonic Expands Mach 2.2 Airliner Program, Bolsters Leadership With Key Hires. *(PDF). Press Release. Retrieved November*, 13, 2017.

[4] C Horstman. Hypersonic Shock-Wave Turbulent-Boundary-Layer Interaction Flows-Experiment and Computation. In *22nd Fluid Dynamics, Plasma Dynamics and Lasers Conference*, page 1760, 1991.

[5] D Gaitonde. Progress in Shock Wave/Boundary Layer Interactions. *Progress in Aerospace Sciences*, 72:80–99, January 2015.

[6] M Thompson. At the Edge of Space: The X-15 Flight Program/Smithsonian Institution Press. *Astronomy*, 20:102, 1992.

[7] D Knight, O Chazot, J Austin, M Badr, G Candler, B Celik, D de Rosa, R Donelli, J Komives, A Lani, et al. Assessment of Predictive Capabilities for Aerodynamic Heating in Hypersonic Flow. *Progress in Aerospace Sciences*, 90:39–53, April 2017.

[8] J Green. Interactions Between Shock Waves and Turbulent Boundary Layers. *Progress in Aerospace Sciences*, 11:235–340, January 1970.

[9] D Dolling. Fifty Years of Shock-Wave/Boundary-Layer Interaction Research: What Next? *AIAA journal*, 39(8):1517–1531, August 2001.

[10] J Delery. Shock Wave/Turbulent Boundary Layer Interaction and Its Control. *Progress in Aerospace Sciences*, 22(4):209–280, January 1985.

[11] A Panaras. Review of the Physics of Swept-Shock/Boundary Layer Interactions. *Progress in Aerospace Sciences*, 32(2-3):173–244, January 1996.

[12] M Escudier. The Distribution of the Mixing Length in Turbulent Flows Near Walls. Rept. Technical report, TWF/TN/1, Imperial College, London, 1965.

[13] B Baldwin and H Lomax. *Thin Layer Approximation and Algebraic Model for Separated Turbulent Flows*. American Institute of Aeronautics and Astronautics, January 1978.

[14] C Hung and R MacCormack. Numerical Solution of Three-Dimensional Shock Wave and Turbulent Boundary Layer Interaction. *AIAA J*, 16(12):1090–1096, October 1978.

[15] M Holden. Shock Wave-Turbulent Boundary Layer Interaction in High Speed Flow. Technical report, Technical Report ARL TR 75-0204, CALSPAN Corporation, Buffalo, NY, June 1975.

[16] M Holden and T Wadhams. A Database of Aerothermal Measurements in Hypersonic Flow in "Building Block" Experiments for CFD Validation. In *41 st AIAA Aerospace Sciences Meeting & Exhibit, Reno, NV*, January 2003.

[17] D Knight and G Degrez. Shock Wave Boundary Layer Interactions in High Mach Number Flows a Critical Survey of Current Numerical Prediction Capabilities. *AGARD ADVISORY REPORT AGARD AR*, 2, December 1998.

[18] M Holden, T Wadhams, and M MacLean. Measurements in Regions of Shock Wave Turbulent Boundary Layer Interaction from Mach 4 to 10 for Open and Blind Code Evaluation/Validation. In *21st AIAA Computational Fluid Dynamics Conference*, page 2836, 2013.

[19] M Holden, T Wadhams, M MacLean, and B Walker. Experimental studies in the lens supersonic and hypersonic tunnels for hypervelocity vehicle performance and code validation. In *15th AIAA International Space Planes and Hypersonic Systems and Technologies Conference*, page 2505, 2008.

[20] AeroSoft Inc. GASPex Version 5.2.2 Reference Guide. v5.2.2, December 2015.

[21] D Wilcox. *Turbulence Modeling for CFD*. DCW industries, 3rd edition, 2006.

[22] M Liou. A Sequel to AUSM: AUSM+. *Journal of computational Physics*, 129(2):364–382, December 1996.

[23] S Park and J Kwon. An Improved HLLE Method for Hypersonic Viscous Flows. In *15th AIAA Computational Fluid Dynamics Conference*, page 2633, June 2001.

[24] P Roe. Approximate Riemann Solvers, Parameter Vectors, and Difference Schemes. *Journal of Computational Physics*, 43(2):357–372, October 1981.

[25] J Quirk. A Contribution to the Great Riemann Solver Debate. *International Journal for Numerical Methods in Fluids*, 18(6):555–574, March 1994.

[26] B Van Leer. On the Relation Between the Upwind-Differencing Schemes of Godunov, Engquist–Osher and Roe. *SIAM Journal on Scientific and Statistical Computing*, 5(1):1–20, March 1984.

[27] A Favre. Equations des Gaz Turbulents Compressibles. *Journal de mecanique*, 4(3):361–390, 1965.

[28] AeroSoft Inc. GASPex Version 5.2.2 Technical Reference. v5.2.2, December 2015.

[29] D Wilcox. *Turbulence Modeling for CFD*. DCW industries Inc., La Canada, CA, 1993.

[30] D Wilcox. Comparison of Two-Equation Turbulence Models for Boundary Layers with Pressure Gradient. *AIAA journal*, 31(8):1414–1421, August 1993.

[31] D Wilcox. Reassessment of The Scale-Determining Equation for Advanced Turbulence Models. *AIAA journal*, 26(11):1299–1310, November 1988.

[32] D Wilcox. *Turbulence Modeling for CFD*. DCW industries, 2nd edition, 1998.

[33] D Knight. *Elements of Numerical Methods for Compressible Flows*, volume 19. Cambridge University Press, August 2006.

[34] C Hirsch. *Numerical Computation of Internal and External Flows*, volume I and II. John Wiley and Sons, New York, 1988.

[35] M Holt. *Numerical Methods in Fluid Dynamics*, volume I and II. Springer-Verlag, New York, 1984.

[36] P Roe. Characteristic-Based Schemes for the Euler Equations. *Annual review of fluid mechanics*, 18(1):337–365, 1986.

[37] M Liou and C Steffen. A New Flux Splitting Scheme. *Journal of Computational physics*, 107(1):23–39, July 1993.

[38] B van Leer. Lecture Notes in Physics. In *E. Krause, éditeur: Proceeding of Eighth International Conference on Numerical Method in Fluid Dynamics*, volume 170, 1982.

[39] M Liou, B Van Leer, and J Shuen. Splitting of Inviscid Fluxes for Real Gases. *Journal of Computational Physics*, 87(1):1–24, 1990.

[40] GAMM Workshop on the Numerical Simulation of Compressible Euler Flows. June 1986.

[41] B Einfeldt, C Munz, P Roe, and B Sjögreen. On Godunov-Type Methods Near Low Densities. *Journal of computational physics*, 92(2):273–295, February 1991.

[42] A Harten, P Lax, and B van Leer. On Upstream Differencing and Godunov-Type Schemes for Hyperbolic Conservation Laws. *SIAM review*, 25(1):35–61, January 1983.

[43] B Einfeldt. On Godunov-Type Methods for Gas Dynamics. *SIAM Journal on Numerical Analysis*, 25(2):294–318, April 1988.

[44] P Lax. *Hyperbolic Systems of Conservation Laws and the Mathematical Theory of Shock Waves*, volume 11. SIAM, Philadelphia, 1972.

[45] S Godunov. A Difference Method for Numerical Calculation of Discontinuous Solutions of The Equations of Hydrodynamics. *Matematicheskii Sbornik*, 89(3):271–306, 1959.

[46] B Van Leer. Flux-Vector Splitting for the Euler Equations. In *Eighth International Conference on Numerical Methods in Fluid Dynamics*, pages 507–512. Springer, 1982.

[47] S Osher. Numerical Solution of Singular Perturbation Problems and Hyperbolic Systems of Conservation Laws. *North-Holland Mathematics Studies*, 47:179–204, January 1981.

[48] H Olivier and H Grönig. The Random Choice Method Applied to Two-Dimensional Shock Focusing and Diffraction. *Journal of Computational Physics*, 63(1):85–106, March 1986.

[49] M Liou. Mass Flux Schemes and Connection to Shock Instability. *Journal of Computational Physics*, 160(2):623–648, May 2000.

[50] S Jang Hyuk Kwon. Study of Godunov-Type Schemes Using Control Parameters. In *Proceedings of the Fourth Asian Computational Fluid Dynamics Conference*, 2000.

[51] H Lin. Dissipation Additions to Flux-Difference Splitting. *Journal of Computational Physics*, 117(1):20–27, March 1995.

[52] C Hirsch. *Numerical Computation of Internal and External Flows, Volumes 1 and 2*. John Wiley and Sons, 1992.

[53] F White and I Corfield. *Viscous Fluid Flow*, volume 3. McGraw-Hill Higher Education Boston, 2006.

[54] J Schetz. *Foundations of Boundary Layer Theory for Momentum, Heat, and Mass Transfer*. Wiley Online Library, January 1984.